

¹ Study of the multi-strange resonance $\Xi(1530)^0$ production
² with ALICE at the LHC energies

³ Jihye Song

4 Contents

5	List of Figures	4
6	List of Tables	8
7	1 The physics of relativistic heavy-ion collisions	9
8	1.1 Standard model	9
9	1.2 QCD and Quark-Gluon plasma	10
10	1.3 Heavy Ion Collisions	16
11	2 Theoretical models	19
12	2.1 Statistical-Thermal model	19
13	2.1.1 Calculations	21
14	2.1.2 Results and comparison with data	23
15	2.2 EPOS, UrQMD	25
16	3 Production of hyperon resonance	27
17	3.1 Strange quark and hyperons	29
18	3.2 Resonance production	31
19	4 A Large Ion Collider Experiment at the LHC	33
20	4.1 The Large Hadron Collider	33
21	4.2 The ALICE project	36
22	4.2.1 ALICE detector	36
23	4.2.2 Data Acquisition (DAQ) and trigger system	47
24	4.2.3 ALICE offline software frame work	49
25	5 Measurement of $\Xi(1530)^0$ production in p-Pb and Pb-Pb	51
26	5.1 $\Xi(1530)^0$ -reconstruction	51
27	5.1.1 Data sample and event selection	51
28	5.1.2 Track and topological selection	55
29	5.1.3 Particle identification	58
30	5.1.4 Signal extraction	61
31	5.2 Efficiency correction	70
32	5.3 Corrected p_T -spectra	73
33	5.4 Systematic uncertainties	75
34	5.5 $\Xi(1530)^0$ transverse momentum spectra	80
35	6 Further results and discussion	83
36	6.1 Mean transverse momentum	83
37	6.2 Particle yield ratios	87

38	6.2.1 Integrated yield ratios of excited to ground-state hadrons	87
39	6.3 Integrated yield ratios to pion	90
40	References	94

41 **List of Figures**

42 1	QCD coupling constant as a function of momentum transfer. Experimental	13
43 data and also theoretical prediction are presented. [1]		
44 2	QCD phase diagram in T as function of μ_B . The chemical freeze out points	
45 are determined from thermal models fit to heavy ion data at SIS, AGS, and		
46 SPS energies. (http://na49info.web.cern.ch/na49info/Public/Press/findings.html)	15	
47 3	The time evolution of a high energy heavy ion collision. [2]	16
48 4	Hydrodynamic evolution of a heavy ion collision with and without the for-	
49 mation of a QGP.	18	
50 5	Grand canonical thermal fit of 0-10% central Pb-Pb collisions, with 3 models	
51 (THERMUS, GSI, SHARE).	19	
52 6	Ratio of baryonic and mesonic resonances over their stable partner as a	
53 function of temperature.	24	
54 7	Ratio of resonances over their stable partner as a function of $\sqrt(s)$	25
55 8	The $J^P = 1/2^+$ ground state baryon octet	28
56 9	The $J^P = 3/2^+$ baryon decuplet	28
57 10	Integrated yield relative to small system (pp or p-Be) as a function of the	
58 mean number of participants $\langle N_{part} \rangle$ in the rapidity range $ y < 0.5$. The		
59 results from ALICE are presented as full symbols, RHIC and SPS data		
60 are shown as open symbols. Boxes on the dashed line at unity represent		
61 statistical and systematic uncertainties on the pp or p-Be reference.	30	
62 11	Hadronic phase	31
63 12	The CERN accelerator complex [3]	34
64 13	The ALICE detector	38
65 14	Schematic view of the ITS [4]	39
66 15	Track impact parameter resolution ($r\phi$) in the transverse plane as function	
67 of p_T for charged particle	40	
68 16	Schematic view of the TPC	41
69 17	Specific energy loss (dE/dx) in the TPC as a function of momentum in Pb-	
70 Pb collisions at $\sqrt{s_{NN}} = 2.76$ TeV. The lines show the parameterizations of		
71 the expected mean energy loss.	42	
72 18	Sketch of events collisions at (8.3 ns, 14.3 ns) is shown in left, background	
73 from Beam 1 at (-14.3 ns, -8.3 ns) in in middel and background from Beam		
74 2 at (14.3 ns, 8.3 ns) is in right.	43	
75 19	Correlation between the sum (y-axis) and difference (x-axis) of signal times	
76 in V0A and V0C. The signals in center come from beam-beam interactions,		
77 the signal in left is background from Beam1 and background from Beam2 is		
78 shown in right hand.	44	
79 20	Sum of V0A and V0C amplitude distribution in top and V0A amplitude	
80 distribution in bottom.	46	

81	21	The overall architecture of the ALICE DAQ and the interface to the HLT system.	47
82	22	Schematic view of the AliRoot framework	50
83	23	Distribution of vertex-z position from the accepted events in p–Pb collision(Left) and in Pb–Pb collisions(Right). The red dashed line indicates vertex cut	53
84	24	Multiplicity distribution of accepted events in p–Pb collision in percentile. The each color presents the four intervals for the analysis.	53
85	25	Centrality distribution of three different trigger classes.	54
86	26	Sketch of the decay modes for Ξ^{*0} and depiction of the track and topological selection criteria.	56
87	27	TPC dE/dx as function of transverse momentum in p–Pb collisions for total (Left) and selected first emitted π in 3σ (Right)	58
88	28	TPC dE/dx as function of transverse momentum in p–Pb collisions for total (Left) and selected second emitted π in 3σ (bottom)	58
89	29	TPC dE/dx as function of transverse momentum in p–Pb collisions for total (Left) and selected last emitted π in 3σ (bottom)	59
90	30	TPC dE/dx as function of transverse momentum in p–Pb collisions for total (Left) and selected proton in 3σ (bottom)	59
91	31	TPC dE/dx as function of transverse momentum in Pb–Pb collisions for total (Left) and selected first emitted π in 3σ (Right)	59
92	32	TPC dE/dx as function of transverse momentum in Pb–Pb collisions for total (Left) and selected second emitted π in 3σ (Right)	60
93	33	TPC dE/dx as function of transverse momentum in Pb–Pb collisions for total (Left) and selected last emitted π in 3σ (Right)	60
94	34	TPC dE/dx as function of transverse momentum in Pb–Pb collisions for total (Left) and selected proton in 3σ (Right)	61
95	35	The $\Xi^\mp\pi^\pm$ invariant mass distribution (Same-event pairs) in $1.8 < p_T < 2.2 \text{ GeV}/c$ and for the multiplicity class 20-40%. The background shape, using pairs from different events (Mixed-event background), is normalised to the counts in $1.49 < M_{\Xi\pi} < 1.51 \text{ GeV}/c^2$ and $1.56 < M_{\Xi\pi} < 1.58 \text{ GeV}/c^2$	62
96	36	The $\Xi^\mp\pi^\pm$ invariant mass distribution (Same-event pairs) in $3.0 < p_T < 3.5 \text{ GeV}/c$ and for the centrality class 0-10%. The background shape, using pairs from different events (Mixed-event background), is normalised to the counts in $1.49 < M_{\Xi\pi} < 1.51 \text{ GeV}/c^2$ and $1.56 < M_{\Xi\pi} < 1.58 \text{ GeV}/c^2$	63
97	37	The invariant mass distribution after subtraction of the mixed-event background in p–Pb collisions. The solid curve represents the combined fit, while the dashed line describes the residual background.	64
98	38	The invariant mass distribution after subtraction of the mixed-event background in Pb–Pb collisions. The solid curve is the combined fit, while the dashed line represents the residual background.	65

122	39	σ fit parameters as a function of p_{Trin} MB in p–Pb collisions (top) and in Pb–Pb collisions (bottom).	67
123	40	$\Xi(1530)^0$ mass distribution as a function of p_{Trin} in each multiplicity classes in p–Pb collisions (top) and the different centrality classes in Pb–Pb (bottom). The mass values are obtained from fit of the Voigtian function.	68
124	41	The raw spectra of $\Xi(1530)^0$ obtained by integrating the Voigtian fit function for different multiplicities in p–Pb collisions (top) and Pb–Pb collisions (bottom). Only the statistical error is reported.	69
125	42	The geometrical acceptance and the reconstruction efficiency ($A \times \epsilon$) for $\Xi(1530)^0$ in $-0.5 < y_{\text{CMS}} < 0$. Only statistical uncertainties are shown.	70
126	43	Real corrected $\Xi(1530)^0$ spectrum (black) for the minimum bias with Levy fit (black curve). Also shown are the unweighted generated (blue) and reconstructed (red) $\Xi(1530)^0$ spectra.	71
127	44	Efficiency as a function of p_{T} in minimum bias events in p–Pb collisions.	72
128	45	Efficiency as a function of p_{Trin} in different centrality classes in Pb–Pb collisions	73
129	46	Corrected p_{T} -spectra of $\Xi(1530)^0$ in NSD and different multiplicity classes in p–Pb collisions.	74
130	47	Corrected p_{T} -spectra of $\Xi(1530)^0$ in different centrality classes in Pb–Pb collisions.	74
131	48	Summary of the contributions to the systematic uncertainty in minimum bias events in p–Pb collisions. The dashed black line is the sum in quadrature of all the contributions.	78
132	49	Systematic uncertainties for each multiplicity classes in p–Pb collisions.	78
133	50	Summary of the contributions to the systematic uncertainty in minimum bias events in Pb–Pb collisions. The dashed black line is the sum in quadrature of all the contributions.	79
134	51	Systematic uncertainties for each multiplicity classes.	79
135	52	Corrected yields as function of p_{T} in NSD events and multiplicity dependent event classes in p–Pb collision system. Statistical uncertainties are presented as bar and systematical uncertainties are plotted as boxes.	81
136	53	Corrected yields as function of p_{T} in different centrality classes in Pb–Pb collision system. Statistical uncertainties are presented as bar and systematical uncertainties are plotted as boxes.	82
137	54	Mean transverse momenta $\langle p_{\text{T}} \rangle$ of Λ , Ξ^- , $\Sigma^{*\pm}$, Ξ^{*0} and Ω^- in p–Pb collisions at $\sqrt{s_{\text{NN}}} = 5.02$ TeV as a function of mean charged-particle multiplicity density $\langle dN_{\text{ch}}/d\eta_{\text{lab}} \rangle$, measured in the pseudorapidity range $ \eta_{\text{lab}} < 0.5$. The results for Λ , Ξ^- and Ω^- are taken from [5, 6, 7]. Statistical and systematic uncertainties are represented as bars and boxes, respectively. The Ω^- and Ξ^- points in the 3rd and 4th lowest multiplicity bins are slightly displaced along the abscissa to avoid superposition with the $\Xi(1530)^0$ points.	84

162	55	Mass dependence of the mean transverse momenta of identified particles for the 0 – 20% V0A multiplicity class and with $-0.5 < y_{\text{CMS}} < 0$ in p–Pb collisions at $\sqrt{s_{\text{NN}}} = 5.02$ TeV [5, 7], and in minimum-bias pp collisions at $\sqrt{s} = 7$ TeV [8] with $ y_{\text{CMS}} < 0.5$. Additionally, D^0 and J/ψ results are plotted. The D^0 and J/ψ were measured in different rapidity ranges: $ y_{\text{CMS}} < 0.5$ [9] ($ y_{\text{CMS}} < 0.9$ [10]) for D^0 (J/ψ) in pp and $-0.96 < y_{\text{CMS}} < 0.04$ [9] ($-1.37 < y_{\text{CMS}} < 0.43$ [11]) for D^0 (J/ψ) in p–Pb. Note also that the results for D^0 and J/ψ in p–Pb collisions are for the 0–100% multiplicity class.	85
171	56	Ratio of $\Xi(1530)^0$ to Ξ^- measured in pp [8], p–Pb [5, 7] and Pb–Pb collisions as a function of $\langle dN_{\text{ch}}/d\eta_{\text{lab}} \rangle$ measured at midrapidity. Statistical uncertainties (bars) are shown as well as total systematic uncertainties (hollow boxes) and systematic uncertainties uncorrelated across multiplicity (shaded boxes). A few model predictions are also shown as lines at their appropriate abscissa.	88
177	57	Ratio of ρ/π (Up), K^*/K , ϕ/K (Left bottom) and Λ^*/Λ with system size measured at mid-rapidity. Statistical uncertainties (bars) are shown as well as total systematic uncertainties (hollow boxes) and systematic uncertainties uncorrelated across multiplicity (shaded boxes). A few model predictions are also shown as lines at their appropriate abscissa.	89
182	58	Ratio of $\Xi(1530)^0$ to π^\pm , measured in pp [12] and p–Pb [8] collisions, as a function of the average charged particle density ($\langle dN_{\text{ch}}/d\eta_{\text{lab}} \rangle$) measured at mid-rapidity. Statistical uncertainties (bars) are shown as well as total systematic uncertainties (hollow boxes) and systematic uncertainties uncorrelated across multiplicity (shaded boxes). A few model predictions are also shown as lines at their appropriate abscissa.	91
188	59	Particle yield ratios to pions of strange and multi-strange hadrons normalized to the values measured in pp collisions, both in pp and in p–Pb collisions. The common systematic uncertainties cancel in the double-ratio. The empty boxes represent the remaining uncorrelated uncertainties.	92
192	60	p_{T} -integrated yield ratios of strange and multi-strange hadrons to $(\pi^+ + \pi^-)$ as a function of $\langle dN_{\text{ch}}/d\eta_{\text{lab}} \rangle$ measured in the rapidity interval $ \eta < 0.5$. The empty and dark-shaded boxes show the total systematic uncertainty and the contribution uncorrelated across multiplicity bins, respectively. The values are compared to calculations from MC models and to results obtained in Pb–Pb and p–Pb collisions at the LHC.	93

198 **List of Tables**

199	1	Components of matter in the Standard Model	9
200	2	Fundamental forces	10
201	3	Parameters used in the thermal-model calculations.	20
202	4	Properties of particles used in the ratio calculations.	22
203	5	Difference of mass (ΔM), baryon number (ΔB), strangeness (ΔS) and charge (ΔQ) of the ratios.	23
204	6	Quantum numbers and masses associated to the three lighter quarks: u, d and s	27
207	7	Lifetime of hadronic resonances	29
208	8	Number of analyzed events per multiplicity/centrality interval	55
209	9	Track selections common to all decay daughters and primary track selections applied to the charged pions from decays of Ξ^{*0}	55
211	10	Topological and track selection criteria.	56
212	11	Summary of the systematic uncertainties on the differential yield, $d^2N/(dp_T dy)$. Minimum and maximum values in all p_T intervals and multiplicity classes in p–Pb, centrality classes in Pb–Pb are shown for each source.	80

215 **1 The physics of relativistic heavy-ion collisions**

216 The main objective of relativistic heavy ion physics is to study the nuclear matter under
 217 extreme conditions which are high temperature and energy density. In these conditions,
 218 the Standard Model anticipates that the nuclear matter undergo a new phase, where the
 219 quarks and the gluons are expected to be de-confined called quark-gluon plasma (QGP)
 220 and to freely move.

221 **1.1 Standard model**

222 If one have question "what the world is made of", our current answer to the question is
 223 Standard Model (SM) families [13] reported in Table 1. The SM explains the way how
 224 those basic blocks of matter interact and how they are ruled by four fundamental forces.
 225 In this explanation, the matter consist of 12 particles, which have a spin of 1/2 (fermions)
 226 and can be categorized in accordance with way how they interact or equivalently to what
 227 charges they carry. The basic particles are six quarks (up, down, charm, strange, top and
 228 bottom) that carry fractional charge of $+\frac{2}{3}e$ or $-\frac{1}{3}e$, and six leptons (electron, electron
 229 neutrino, muon, muon neutrino, tau, tau neutrino) with integer charge.

Family	Quarks				Leptons		
	Name	Charge[e]	Mass		Name	Charge[e]	Mass
1	u	2/3	$2.2^{+0.6}_{-0.4}$ MeV/c ²		e^-	-e	0.511 MeV/c ²
	d	-1/3	$4.7^{+0.5}_{-0.4}$ MeV/c ²		ν_e	0	< 2 eV/c ²
2	c	2/3	$1.27^{+0.03}$ GeV/c ²		μ^-	-e	105.66 MeV/c ²
	s	-1/3	96^{+8}_{-4} MeV/c ²		ν_μ	-e	< 0.19 eV/c ²
3	t	2/3	173.21 ± 1.22 GeV/c ²		τ^-	-e	1.777 GeV/c ²
	b	-1/3	$4.18^{+0.04}_{-0.03}$ GeV/c ²		ν_τ	-e	< 18.2 MeV/c ²

Table 1: Components of matter in the Standard Model

230 The interactions between elementary particles are described by the exchange of gauge
 231 bosons(gluon, photon, Z-boson, W-boson), reported in Table 2 including with their cou-
 232 pling strengths. The leptons are governed the weak force and the electromagnetic force.
 233 Quarks have color property which is the character of charge in the strong force. The color
 234 could take one out of three possible values (conventionally red, green and blue). The color
 235 can not be appeared freely. After they are confined they come out in the form of hadron
 236 which are colorless. Further explanaition on color is described in Section 1.2. Then, the
 237 hadrons are grouped into baryon and mesons. Baryons are made up f three quarks, qqq or
 238 ($\bar{q}\bar{q}\bar{q}$) while mesons consist of two quarks ($q\bar{q}$).

239 The models that describe these interactions are listed as follows:

240

Force	Strength	Gauge Boson(s)	Applies on
Strong force	1	8 Gluons(g)	Quarks, gluons
Electromagnetic force	$\simeq 10^{-2}$	Photon (γ)	All charged particles
Weak force	$\simeq 10^{-7}$	W^\pm, Z^0	Quarks, leptons
Gravitation	$\simeq 10^{-39}$	Gravitons	All particles

Table 2: Fundamental forces

241 **Quantum Electro-Dynamics (QED)** is a quantum field theory of the electromagnetic
 242 force and describes how light and matter interact. This is the first theory where
 243 full agreement between quantum mechanics and special relativity is achieved. It explains
 244 mathematically not only all interactions of light with matter but also those of charged
 245 particles with one another.

246 **Electroweak Theory (EW)** is the unified description of two of the four known fundamental
 247 interactions of nature: electromagnetism and the weak interaction. The first
 248 measurement of the existence of the weak bosons W^+ , W^- and Z^0 was performed in 1983,
 249 when they were produced and directly observed in $Spp\bar{S}$ collisions at CERN.

251 **Quantum Chromo-dynamics (QCD)** is the theory of the strong interaction (color
 252 force), describing the interactions between quarks and gluons which make up the hadrons.
 253 Starting from the classification of the large amount of particles discovered during the fifties,
 254 the original idea of the quark model by Gell-Mann (Nobel Prize in 1969) has been developed
 255 during the sixties until 1973, when David J. Gross, H. David Politzer and Frank Wilczek
 256 discovered the asymptotic freedom property of the strong nuclear interaction.

258 1.2 QCD and Quark-Gluon plasma

259 As the number of known particle species became large, the idea that these could be the
 260 elementary constituents of matter was replaced by the notion that these species could in
 261 fact be composite objects made up of fewer, more elementary particles, in a similar way to
 262 what had already happened to the elements of Mendeleev's Periodic Table. The original
 263 idea by Gell-Mann (1964) was that the hadrons could be obtained as combination of the
 264 fundamental representation of an $SU_f(3)$ group, where three different flavors of quark (q
 265 = u, d, s) combine to build mesons ($q\bar{q}$) and hadrons (qqq). However, when cataloging
 266 hadrons using the $SU_f(3)$ group, there are anomalous states, such as the Ω^- (sss) and the
 267 Δ^{++} (uuu), that are combinations of three quarks of the same flavor, in clear contrast
 268 with the Pauli exclusion principle for fermions. A solution was proposed in 1965 by Moo-
 269 Young Han with Yoichiro Nambu and Oscar W. Greenberg, who independently solved the
 270 problem by proposing that quarks possess an additional $SU(3)$ gauge quantum number,

271 later called color charge. This new quantum number may assume three states, represented
 272 by the three primary colors: red, green and blue (denoted symbolically by R, G and B,
 273 respectively). The introduction of this new quantum number also provides an explanation
 274 to other empirical evidence, such as the fact that no qq , $\bar{q}q$ or the single quark have never
 275 been observed directly. On the other hand, the existence of color charge gives rise to the
 276 possible existence of differently colored states for each particle. Thus, we could have many
 277 states for the proton, such as $u_R u_G d_B$, $u_R u_G d_G$, $u_B u_R d_R$, and so on. The fundamental
 278 rule that solves such contradictions is that all the particle states observed in nature are
 279 "colorless" or "white" (or, to be more precise, unchanged under $SU_c(3)$ rotations). The
 280 dynamics of the quarks and gluons are controlled by the gauge invariant QCD Lagrangian:

$$\mathcal{L}_{QCD} = \underbrace{i\delta_{ij}\bar{\Psi}_q^i\gamma^\mu\partial_\mu\Psi_q^j}_{\mathcal{L}_1} + \underbrace{g_s\bar{\Psi}_q^i\gamma^\mu t_{ij}^a A_\mu^a\Psi_q^j}_{\mathcal{L}_2} + \underbrace{m_q\bar{\Psi}_q^i\Psi_q^j}_{\mathcal{L}_3} + \underbrace{\frac{1}{4}F_{\mu\nu}^a F^{a\mu\nu}}_{\mathcal{L}_4} \quad (1)$$

281 where the coloured gluon field tensor, $F_{\mu\nu}^a$ (with color index a) and the squared gauge
 282 coupling parameter, g_s^2 (associated to the strong coupling constant α_s) are defined as:

$$F_{\mu\nu}^a = \partial_\mu A_\nu^a - \partial_\nu A_\mu^a + g_s f^{abc} A_\mu^b A_\nu^c \quad (2)$$

283 and

$$g_s^2 = 4\pi\alpha_s \quad (3)$$

284 where:

- 285 • Ψ_q^i : the quark field with flavor q and color index $i \in [1;3]$, such as $\Psi_q = (\Psi_{qR}, \Psi_{qG},$
 286 $\Psi_{qB})^T$ and A_μ^a is the gluon field with color index a (adjoint representation)
- 287 • γ^μ : Dirac matrices that express the vector nature of the strong interaction, with μ
 288 being the Lorentz vector associated index
- 289 • m_q : quark mass, a priori not equal to zero (resulting from the Higgs mechanism or
 290 equivalent)
- 291 • t_{ij}^a : generator matrices of the group $SU_c(3)$, proportional to the Gell-Mann matrices,
 292 that perform revolutions in color space, representing interaction of quarks and gluons
- 293 • f^{abc} : structure constant of QCD

294 Each of the four terms of the QCD Lagrangian expresses and aspect of the interaction,
 295 specifically:

- 296 • \mathcal{L}_1 : gives the kinetic energy of the quark field Ψ_q^i

- 297 • \mathcal{L}_2 : gives the interaction between quarks (fermions) and gluons (the bosons of the
298 interaction)
- 299 • \mathcal{L}_3 : gives the mass of the quarks
- 300 • \mathcal{L}_4 : gives the kinetic energy of the gluons

301 The terms of this equation, together with the fundamental parameters α_s and m_q ,
302 summarize in just one expression all the features of the strong interaction. The first three
303 terms describe the free propagation of quarks and gluons and the quark-gluon interaction.
304 The remaining two terms show the presence of three and four gluon vertices in QCD and
305 reflect the fact that gluons themselves carry color charge. This is a consequence of the non-
306 abelian⁴ character of the gauge group. This peculiarity of the QCD interaction imposes the
307 evolution of the strong coupling constant, α_s . The corresponding trend has been measured
308 experimentally, and compared in Figure 1 with predictions. A practical consequence of
309 this behavior is that the corresponding potential has a completely different shape than the
310 other fundamental interactions and can be expressed by the following equation:

$$V(r) = -4 \frac{\alpha_s}{3r} + kr \quad (4)$$

311 where r is the separation distance between the two quarks and k is a constant that is
312 approximately 1 GeV/fm.

313 Three are main properties of the QCD interaction:

314
315 **Confinement** At large distances between quarks and gluons (i.e. small values of trans-
316 ferred momentum Q in Figure 1) the coupling constant is large and the associated force
317 is strong enough to keep these elementary con- stituents (usually called partons) confined
318 in bounded states. As expressed in the Equation 4, the attractive potential increases with
319 the increasing of the relative distance between the two partons preventing the separation
320 of an individual quark or gluon. This explains the meaning of the term "confinement"
321 adopted to describe this energy regime. From the theoretical point of view, the large value
322 of α_s make impossible any perturbative approach in the solution of the Hamilton equation
323 of the system. A successful solution is to perform the study of the system on a discrete
324 space. Such techniques are known as lattice QCD and are based on numerical Monte Carlo
325 simulations. The challenge for the calculations is to reduce the lattice spacing in order to
326 approach the continuum.

327
328 **Asymptotic freedom** Reducing the distance between quarks and gluons (i.e. increas-
329 ing Q in Figure 1) the coupling constant α_s becomes smaller. As anticipated, this is a
330 unique feature among the forces and comes from the non-abelian nature of the QCD gauge
331 symmetry. Such a phenomenon is also depicted by the weakening of the anti-screening
332 effect of the surround- ing virtual gluons with decreasing distance. In this way two quarks

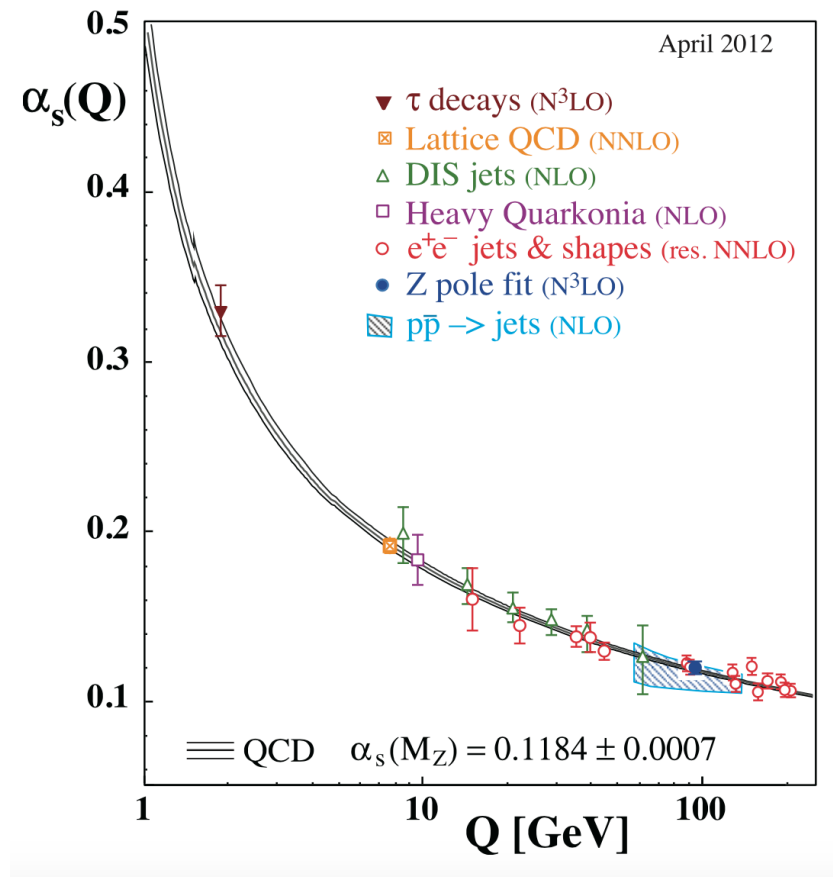


Figure 1: QCD coupling constant as a function of momentum transfer. Experimental data and also theoretical prediction are presented. [1]

333 closer and closer in space show each other a smaller and smaller color charge.

334

335 **Chiral symmetry** One further property of interest is connected to the chirality of
336 the quark. It can be verified that the QCD lagrangian for massless quarks is invariant
337 under a chiral rotation ($SU_L(N_f) \times SU_R(N_f)$), while the operator $\bar{q}q = \bar{q}_L q_R + \bar{q}_R q_L$ is
338 not invariant (in the axial part), meaning that the mesons (state $\bar{q}q$) should have the same
339 mass. Experimentally this is clearly not true, and it could be shown that the axial current
340 is conserved (PCAC and the Goldberger-Treiman relation). The solution to this puzzle
341 is that the chiral (axial-vector) symmetry is spontaneously broken; this means that the
342 symmetry of the Hamiltonian is not a symmetry of the corresponding ground state. It
343 has also been shown, by G. 't Hooft, that the confinement implies a dynamical breaking
344 of the chiral symmetry. This means that the breaking comes from the interaction between
345 the objects in the system. From this follows that the masses of the quarks are strongly
346 increased because of the interaction with the constituents of the system. This mechanism,
347 known as dynamical chiral symmetry breaking justifies the mass of the hadrons, reducing
348 the role of the Higgs mechanism in the mass explanation at least for the light hadrons.

349 The asymptotic freedom property suggests the existence of a state of matter, called
350 Quark-Gluon Plasma (QGP), in which the constituents of the hadrons are de-confined.
351 The hatched region in Figure 2 presents the expected phase boundary between partonic
352 and hadronic matter from lattice QCD calculations.

353 Two relevant thermodynamical observables of the system are plotted in the figure. One
354 is temperature T and another one is the baryonic chemical potential μ_B . The red points
355 have been measured from thermal models fit on data from different experiment [14] and
356 lie along a line that represent the limit between the two phases. As one can see in Figure
357 2, there are different ways to achieve the transition. It can be performed by changing the
358 temperature and/or the net baryonic density (μ_B).

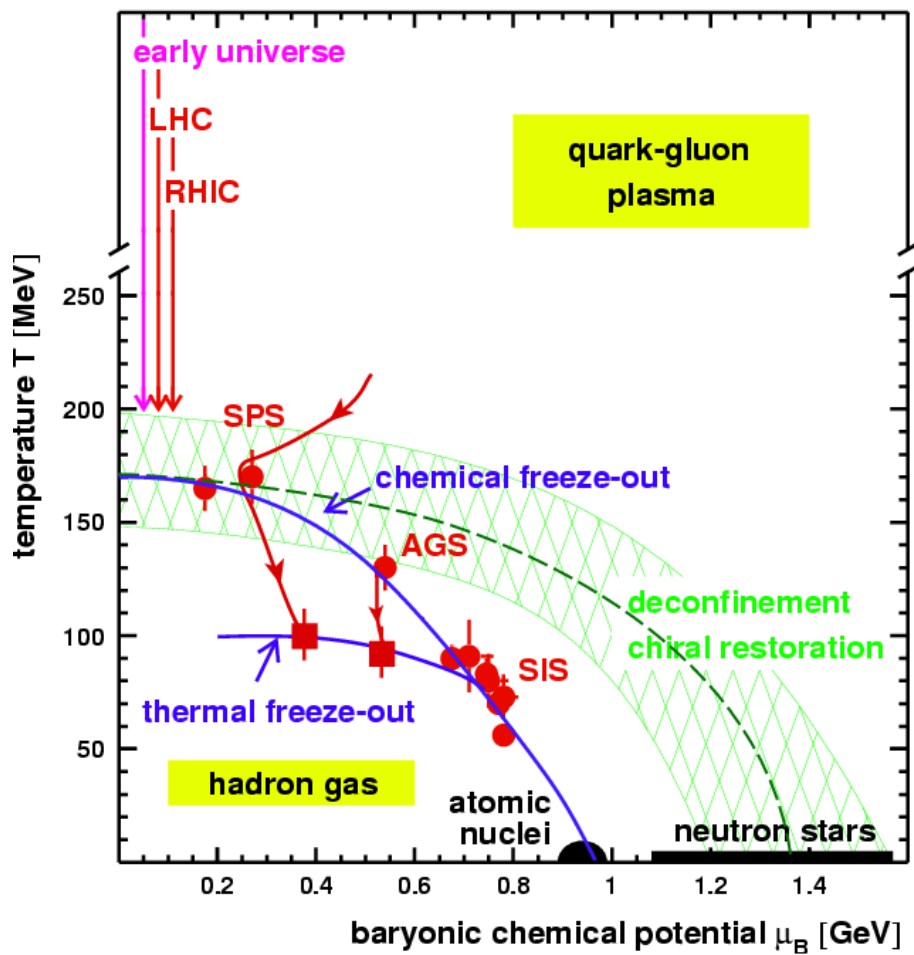


Figure 2: QCD phase diagram in T as function of μ_B . The chemical freeze out points are determined from thermal models fit to heavy ion data at SIS, AGS, and SPS energies. (<http://na49info.web.cern.ch/na49info/Public/Press/findings.html>)

359 **1.3 Heavy Ion Collisions**

360 Knowledge of the space-time evolution of the system created in high energy heavy ion
 361 collisions help to understand the dynamics of nuclear matter under extreme conditions.
 362 The Figure 3 presents the schematic of the time evolution in case of collision of two Lorentz
 363 contracted nuclei at very high energy. After the colliding, a large amount of energy can be
 364 deposited in a small area of space and in a short duration of time. The matter produced
 365 might have very high energy density and temperature so that it is sufficiently able to reach
 366 to QGP that is baryon free region.

367 Just after the colliding, the medium may not be in thermal equilibrium which can be
 368 reached after that the evolution is governed by the law of thermodynamics. As the system
 369 expands and cools, the hadronization takes place and the freeze out comes after some
 370 time. Different stages during the collisions can be studied by various observables, such as,
 371 Electromagnetic probes, Quarkonia and heavy flavour, Hard probes, Electroweak probes,
 372 global properties and Freeze-out condition as well. Most of the produced particles in the
 373 high energy heavy-ion collisions are emitted at freeze-out. In order to estimate the energy
 374 density, pressure, temperature and baryon chemical potential, the study of particle after
 375 freeze-out gives crucial information. Those quantities could be derived from measurement
 376 of multiplicity and rapidity distribution, transverse momentum (p_T) distributions.

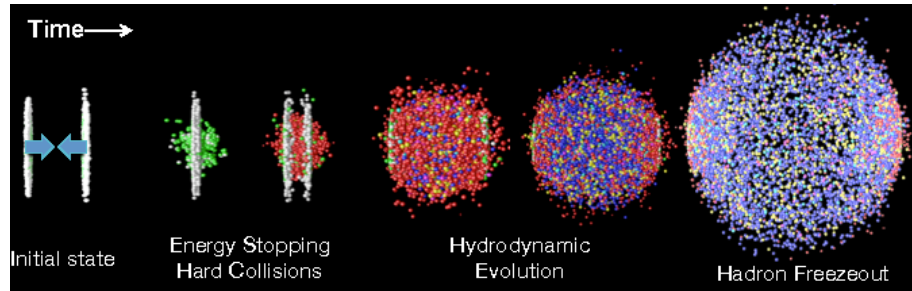


Figure 3: The time evolution of a high energy heavy ion collision. [2]

377 In the case a QGP is formed, it will eventually expand because of its internal pressure.
 378 As the system expands it also cools. The space-time evolution of the expansion can be
 379 seen in Figure 4 (right side). A and B represent the two incoming ion beams. After a pre-
 380 equilibrium phase a QGP is formed. As it expands, the system will eventually reach what
 381 is known as the critical temperature (T_c). At this point partons begin to hadronize and this
 382 will continue until the chemical freeze-out (T_{ch}) takes place, when inelastic collisions cease.
 383 At this stage the distribution of hadrons is frozen. As cooling and expansion continue the
 384 hadrons reach what is called thermal freeze out (T_{fo}). Here the elastic collisions stop and
 385 the hadrons carry fixed momenta. The QGP state can not be directly observed, because of
 386 its short lifetime. Instead, through experiment we measure the final state hadrons, which

387 have a fixed momentum after T_{fo} . The observables of interest should tell us about the
388 de-confinement and the thermodynamic properties of the matter. Moreover, experimental
389 measurements include yields and p_T spectra of various particle species, azimuthal studies
390 of high p_T particles, phase space distributions, and particle correlations.

391 A practical way to reach a critical condition in which a nuclear system should undergo
392 a phase transition to the QGP, at high temperature and/or matter density, is to collide
393 two nuclei at sufficiently high energy. Therefore, relativistic and ultra-relativistic heavy-ion
394 collisions are a unique tool to study nuclear matter under extreme conditions.

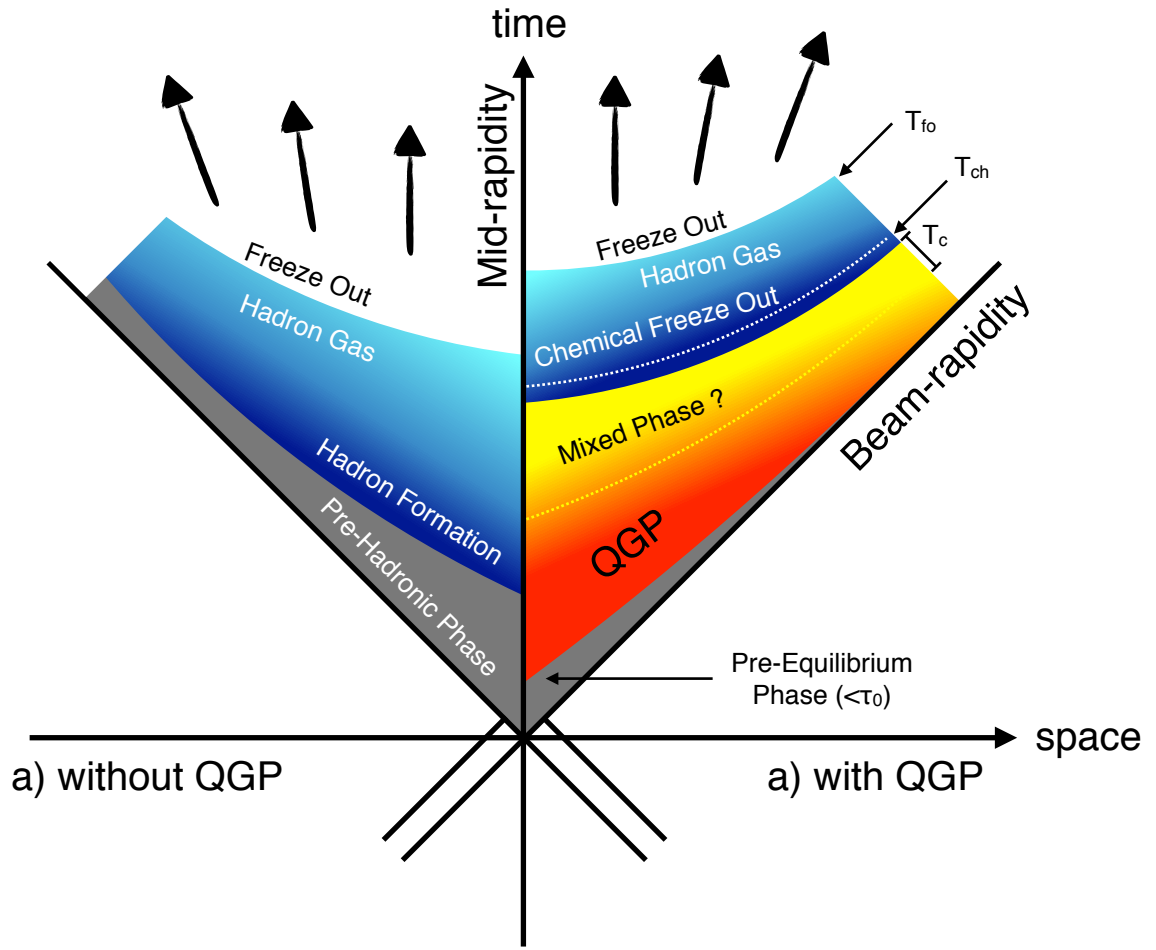


Figure 4: Hydrodynamic evolution of a heavy ion collision with and without the formation of a QGP.

395 2 Theoretical models

396 2.1 Statistical-Thermal model

397 The statistical-thermal model deal with the fireball created from high energy collisions as
 398 an ideal gas of hadrons including resonances. These hadrons are described by local thermal
 399 distributions at freeze-out with the parameters common to all particle species. The
 400 model has proved successful in applications to relativistic collisions of both heavy ions and
 401 elementary particles. The comparison between prediction and data obtained from Pb–Pb
 402 collisions are shown in Figure 5. In light of this success, THERMUS, a thermal model
 403 analysis package, has been developed for incorporation into the object-oriented ROOT
 404 framework [15].

405

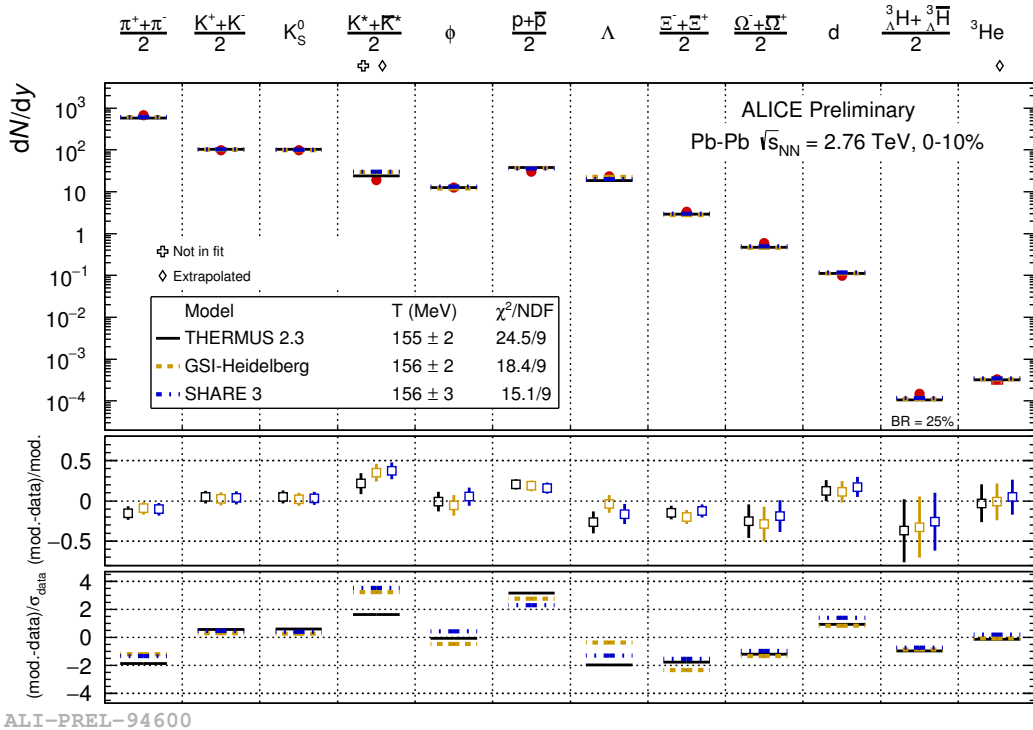


Figure 5: Grand canonical thermal fit of 0-10% central Pb-Pb collisions, with 3 models (THERMUS, GSI, SHARE).

406 There are three types of statistical-thermal models in explaining data in high energy
 407 nuclear physics and THERMUS treats the system quantum numbers B (baryon number),

408 S (strangeness) and Q (charge) within three distinct formalisms:

- 409 1. **Grand-Canonical Ensemble:** Because the hot dense matter produced in nucleus-
410 nucleus collisions is large enough, this ensemble is the most widely used in applica-
411 tions to heavy-ion collisions, in which the quantum numbers or particle numbers are
412 conserved on average through the temperature and chemical potential.
- 413 2. **Fully-Canonical Ensemble:** In which B, S and Q are exactly conserved and this
414 ensemble used in high-energy elementary collisions such as $p\bar{p}$, $p\bar{p}$ and e^-e^+ collisions.
- 415 3. **Strangeness-Canonical Ensemble:** In heavy-ion collisions, the large numbers of
416 baryons and charged particles generally allows baryon number and charge to be
417 treated grand-canonically. However, in small systems or at low temperatures, a
418 canonical treatment leads to a suppression of hadrons carrying non-zero quantum
419 numbers, since these particles have to be created in pairs and the resulting low pro-
420 duction of strange particles needs a canonical treatment of strangeness. Within this
421 ensemble the strangeness in the system is fixed exactly by its initial value of S, while
422 the baryon and charge content are treated grand-canonically.

423 In order to calculate the thermal properties of a system, the partition function requires to
424 be evaluated. The form of it clearly depends on the choice of ensemble. In the present
425 analysis the strangeness-canonical ensemble used and statistical-thermal model requires six
426 parameters as input: the chemical freeze-out temperature T , baryon and charge chemical
427 potentials μ_B and μ_Q respectively, canonical or correlation radius, R_C ; the radius inside
428 which strangeness is exactly conserved and the fireball radius R . An additional strangeness
429 saturation factor γ_S has been used as indicator of a possible departure from equilibrium
430 and $\gamma_S = 1.0$ corresponds to complete strangeness equilibration.

431 The volume dependence cancels out when studying the particle ratios as well as strangeness
432 canonical equivalent to grand canonical formalism if $\Delta S = 0$ in the ratios and γ_S also can-
433 cels out. Parameters used in the analysis reported in Table 3.

Table 3: Parameters used in the thermal-model calculations.

Parameter	Value
T (MeV)	varied
μ_B (MeV)	0.1
μ_Q (MeV)	0.0
γ_S	1.0

434

435 **2.1.1 Calculations**

436 *Concept:*

437 In order to calculate the particle ratios within strangeness canonical formalism of THER-
438 MUS, temperature varied between 60 MeV to 180 MeV and particle yields extracted for
439 each temperature value and then primary particle ratios calculated for each case.

440

441 *Feed-Down Correction:*

442 Since the particle yields measured by the detectors in collision experiments include feed-
443 down from heavier hadrons and hadronic resonances, the primitive hadrons are allowed to
444 decay to particles considered stable by the experiment before model predictions are com-
445 compared with experimental data. In the analysis only Λ particles counted as stable (do not
446 allowed to decay) so there is no feed-down contribution from these particles to the other
447 ratios.

448

449 Properties of studied particles and their particle ratios listed in Table 4 and Table 5,
450 respectively.

451

452

Table 4: Properties of particles used in the ratio calculations.

Particle	Δ^{++}	Δ^{*+}	K^{*0}	K^+	Λ^*	Λ	Σ^{*+}	Σ^+	Σ^0	Ξ^{*0}	Ξ^-
Mass (MeV/ c^2)	1232	938.27	895.92	493.67	1519.5	1115.68	1382.8	1189.37	1192.64	1531.80	1321.31
Width (MeV/ c^2)	120	—	50.7	—	15.6	—	37.6	—	—	9.1	—
$c\tau$ (fm)	1.6	—	3.9	-12.6	—	5.51	—	—	21.6	—	—
Ang. Momentum (J)	$3/2$	$1/2$	1	0	$3/2$	$1/2$	$3/2$	$1/2$	$1/2$	$3/2$	$1/2$
$^{22}_{\Lambda}$ Isospin (I)	$3/2$	$1/2$	$1/2$	$1/2$	0	0	1	1	1	$1/2$	$1/2$
Parity (P)	+1	+1	-1	0	-1	+1	+1	+1	+1	+1	+1
Strangeness (S)	0	0	1	1	-1	-1	-1	-1	-1	-2	-2
Baryon Number (B)	1	1	0	0	1	1	1	1	1	1	1
Decay Channel	$\text{p}\pi^+$	—	π^-	$\mu^+\nu_\mu$	pK^-	$p\pi^-$	$\Lambda\pi^+$	$\text{p}\pi^0$	$\Lambda\gamma$	$\Xi^-\pi^+$	$\Lambda\pi^-$
Branching Ratio (%)	~ 100	—	~ 66.7	~ 63.54	~ 45	~ 63.9	~ 87	~ 51.6	~ 100	~ 64	~ 99.9
Q-Value(MeV/ c^2)	154.16	—	262.68	—	87.55	37.84	127.55	111.53	76.96	70.92	70.66

Table 5: Difference of mass (ΔM), baryon number (ΔB), strangeness (ΔS) and charge (ΔQ) of the ratios.

Particle	Δ^{++}/p	K^*/K^+	Λ^*/Λ	Σ^{*+}/Λ	Σ^0/Λ	Σ^{*+}/Σ^+	Ξ^{*0}/Ξ^-
ΔM (MeV/ c^2)	293.8	402.25	403.82	267.12	76.96	193.43	210.49
ΔB	0	0	0	0	0	0	0
ΔS	0	0	0	0	0	0	0
ΔQ	+1	-1	0	+1	0	0	-1
Slope (%) per MeV	0.19	0.76	0.98	0.25	-0.08	0.37	0.42

453 **2.1.2 Results and comparison with data**

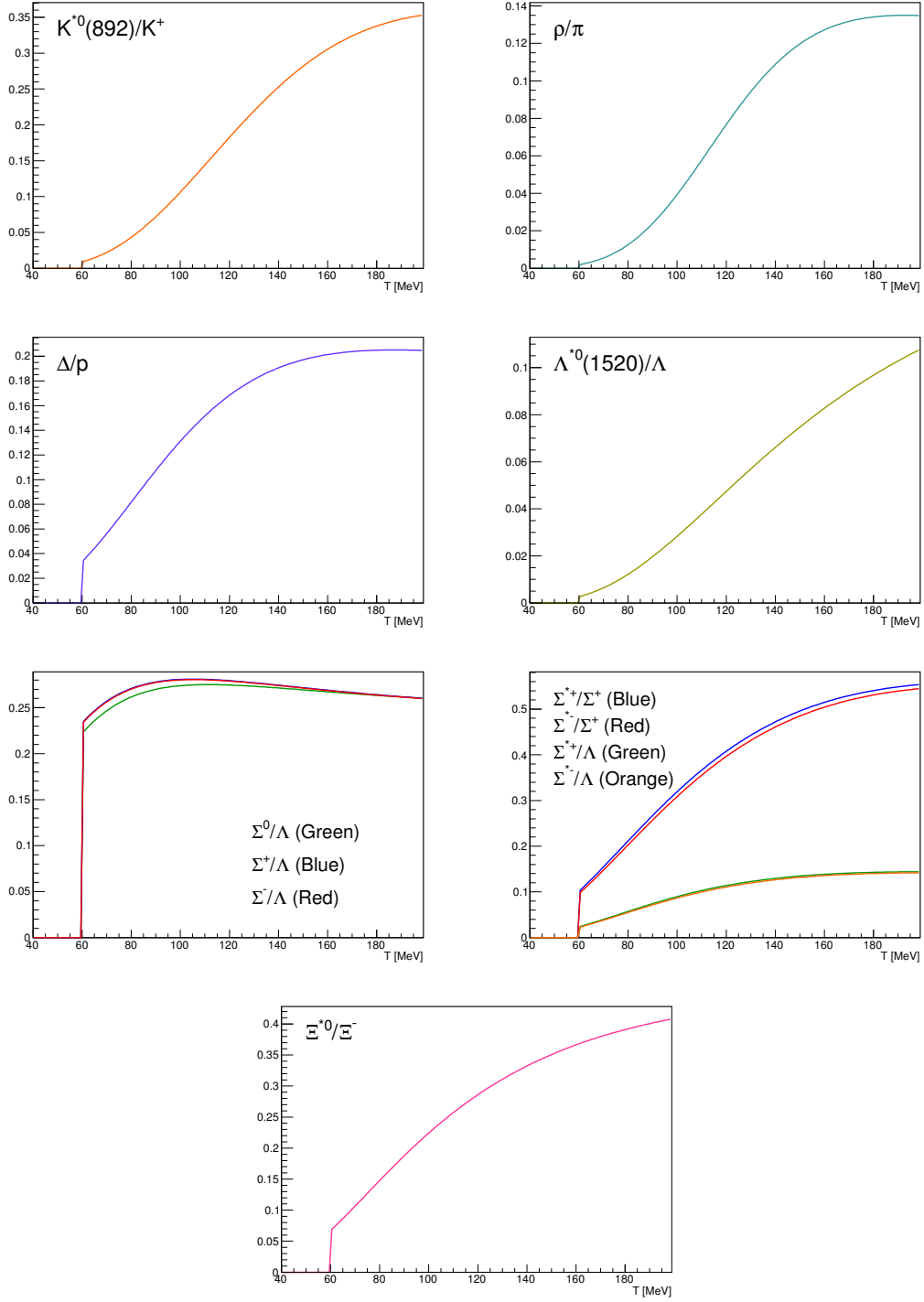


Figure 6: Ratio of baryonic and mesonic resonances over their stable partner as a function of temperature.

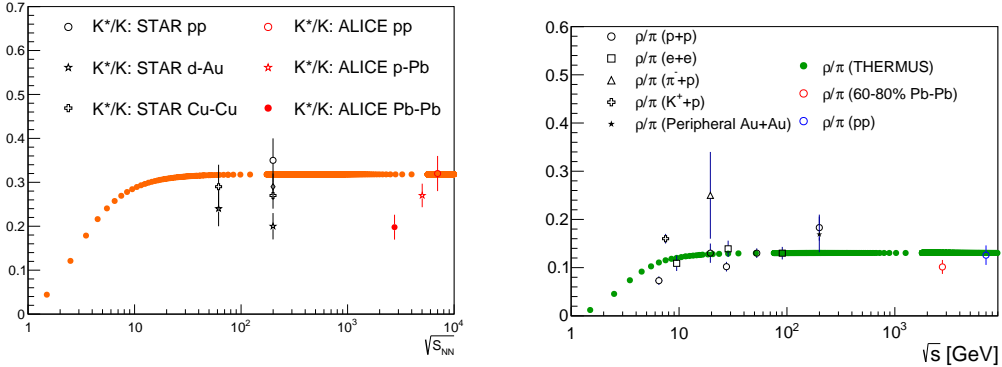


Figure 7: Ratio of resonances over their stable partner as a function of $\sqrt{(s)}$.

454 2.2 EPOS, UrQMD

455 The EPOS3 model [16, 17, 18] describes the full evolution of a heavy-ion collision. The
 456 initial stage is treated via a multiple-scattering approach based on Pomerons and strings.
 457 The reaction volume is divided into a core and a corona part [19]. The core is taken as
 458 the initial condition for the QGP evolution, for which one employ viscous hydrodynamics.
 459 The corona part is simply composed of hadrons from string decays. After hadronisation of
 460 the fluid (core part), these hadrons and as well the corona hadrons are fed into UrQMD
 461 [20, 21], which describes hadronic interactions in a microscopic approach. The chemical
 462 and kinetic freeze-outs occur within this phase. The chemical freeze-out is expected to
 463 occur shortly after the phase transition from partonic to hadronic matter and is followed
 464 by the kinetic freeze-out.

465 As explained in [16, 17, 18, 19], EPOS3 is an event generator based on 3+1D vis-
 466 cous hydrodynamical evolution starting from flux tube as an initial conditions, which are
 467 produced in the Gribov-Regge multiple scattering framework. An individual scattering is
 468 treated as a Pomeron, identified with a parton ladder, eventually showing up as flux tubes
 469 (or strings). Each parton ladder is composed of a pQCD hard process, plus initial and final
 470 state linear parton emission.

471 The final state partonic system (corresponding to a Pomeron) amounts to (usually two)
 472 color flux tubes, being mainly longitudinal, with transversely moving pieces carrying the
 473 p_T of the partons from hard scatterings. One has two flux tubes based on the cylindrical
 474 topology of the Pomerons. Each quark- antiquark pair in the parton ladder will cut a string
 475 into two; in this sense one may have more than two flux tubes. In any case, these flux
 476 tubes eventually constitute both bulk matter, also referred to as "core" (which thermalizes,
 477 flows, and finally hadronizes) and jets (also referred to as "corona"), according to some

478 criteria based on the energy of the string segments and the local string density. For the
479 core, we use a 3+1D viscous hydrodynamic approach, employing a realistic equation of
480 state, compatible with lQCD results. We employ for all calculations in this paper a value
481 of $\eta/s = 0.08$. Whenever a hadronization temperature of T_H is reached, we apply the
482 usual Cooper-Frye freeze-out procedure, to convert the fluid into particles. We use $T_H =$
483 166MeV. From this point on, we apply the hadronic cascade UrQMD [20, 21], about which
484 more details are given later. All hadrons participate in the cascade, including those from
485 the core (after freeze- out) and the corona. The corona particles, from string decay, are only
486 "visible" after a certain formation time (some constant of order one fm/c), multiplied by
487 the corresponding gamma factor), so very high p_T particles have a good chance to escape.

488 The UrQMD model is a non-equilibrium transport approach. The interactions of
489 hadrons in the current version include binary elastic and $2 \rightarrow n$ inelastic scatterings, res-
490 onance creations and decays, string excitations, particle + antiparticle annihilations as
491 well as strangeness exchange reactions. The cross sections and branching ratios for the
492 corresponding interactions are taken from experimental measurements (where available),
493 detailed balance relations and the additive quark model. The model describes the full
494 phase-space evolution of all hadrons, including resonances, in a heavy- ion collision based
495 on their hadronic interactions and their decay products. Due to the short lifetime of res-
496 onances, their decay products may interact in the hadronic phase. This is not the case
497 for weak decays, where the system has already decoupled at the time of the decay. As
498 discussed previously, the experimental reconstruction of resonances will be influenced by
499 the final state interactions of the decay products. Resonance signals have been previously
500 studied using the UrQMD model.

501 **3 Production of hyperon resonance**

502 The Quark Model, proposed independently by Murray Gell-Mann and Yuval Ne'eman in
 503 1964 [22], enables the classification of hadrons in terms of their constituent quarks. In
 504 this model, the lighter mesons and baryons are representations of an $SU_f(3)$ group, whose
 505 fundamental representation is the three dimensional vector (u, d, s). These are the three
 506 lighter quarks whose characteristics are reported in Table reftable:quark.

Light flavor	d	u	s
Baryon number (B)	+1/3	+1/3	+1/3
Electric charge (Q)	-1/3	+2/3	-1/3
Isospin (I)	-1/2	+1/2	0
Strangeness (S)	0	0	-1
mass (MeV/c^2)	$2.3^{+0.7}_{-0.5}$	$4.8^{+0.5}_{-0.3}$	95 ± 5

Table 6: Quantum numbers and masses associated to the three lighter quarks: u, d and s

507 The hadronic state are obtained from the decomposition of the following scalar prod-
 508 ucts of the fundamental representations of the group:

509 $Meson (q\bar{q}) : 3 \otimes \bar{3} = 1 \oplus 8$

511 $Baryon (qqq) : 3 \otimes 3 \otimes 3 = 10_S \oplus 8_M \oplus 8_M \oplus 1_A$

514 For the baryons without *c* or *b* quark, flavor and spin may be combined in an approxi-
 515 mate flavor-spin $SU(6)$, in which the six basic states are $d \uparrow, d \downarrow, \dots, s \downarrow$ (\uparrow, \downarrow = spin up,
 516 down). Then the baryons belong to the multiplets on the right side of

518 $6 \otimes 6 \otimes 6 = 56_S \oplus 70_M \oplus 70_M \oplus 20_A$

520 Here, the 56 representation can be decompose in an octet ($J^P = 1/2^+$) and a decuplet
 521 ($J^P = 3/2^+$), as can be seen in Figure 8 and Figure 9.

522 Among these hadrons, the special family of particles that contain at least one strange
 523 quark but not heavier quarks (like charm or bottom), are called hyperons. These are:
 524 the $\Lambda(uds)$, the triplet $\Sigma^+(uus)$, $\Sigma^0(uds)$, $\Sigma^-(dds)$, the doublet $\Xi^-(dss)$, $\Xi^0(uss)$ and the
 525 $\Omega(sss)$ and the corresponding antiparticles. Ξ and Ω are the only hyperons containing more
 526 than one strange quark, hence they are called multi-strange baryons. Resonances shown
 527 in Figure reffig:decuplet having * with its name (e.g. $X^{*\pm}$) are particles which have higher
 528 mass than the corresponding ground state particle with the same quark content.

529 Different resonances having various lifetimes (Table 7) can be used as tool to explore
 530 different stages of the fireball expansion as discussed in section 1.3. In order to have

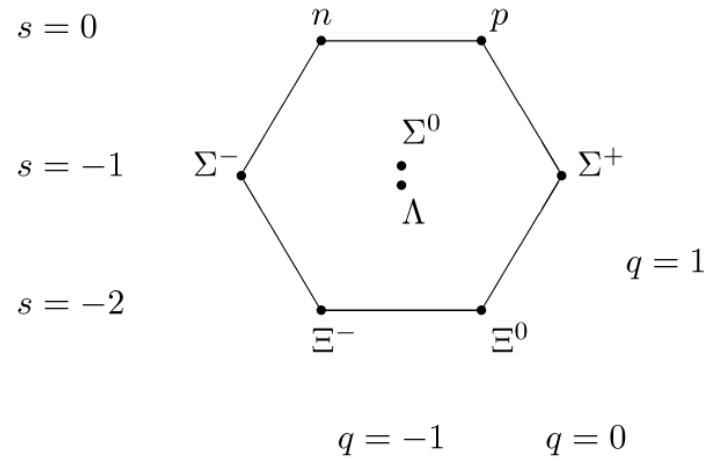


Figure 8: The $J^P = 1/2^+$ ground state baryon octet

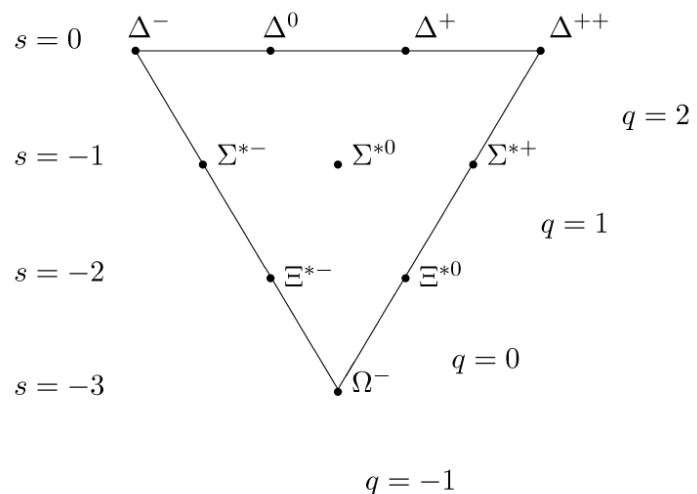


Figure 9: The $J^P = 3/2^+$ baryon decuplet

531 insight on the role of the re-scattering effect between the freeze-out phases, it is important
 532 to measure the ratio between resonances and stable hadrons and compare it with different
 533 lifetimes.

Particle	$\rho(770)$	$\Delta(1232)$	$K^*(892)$	$\Sigma(1385)$	$\Lambda(1520)$	$\Xi(1530)$	$\Phi(1020)$
Lifetime[c τ]	1.3 fm	1.7 fm	4.0 fm	5.5 fm	10.3 fm	22 fm	46 fm

Table 7: Lifetime of hadronic resonances

534 In the following, a general overview of the role of the strange quark within the QGP
 535 studies with heavy-ion collisions is given. And importance of the measurement of resonance
 536 is explained as probe of properties in the duration of hadronic phase from the chemical(T_{ch})
 537 to the kinetic freeze-out(T_{kin}).

538 **3.1 Strange quark and hyperons**

539 The original interest in the strangeness in the context of the QGP comes from an idea by
 540 Johann Rafelski and Berndt Müller. In 1982, they suggested a possible signature for the
 541 formation of a QGP in a heavy-ion collision [23]. The key argument, at a fixed collision
 542 energy, rests on the different production mechanism of the s quark within two different
 543 systems:

544 **1. Hadron Gas (HG)** , where the degrees of freedom are the hadronic ones, as quark and
 545 gluons are confined. The great abundance of pions in the HG suggests to consider the
 546 production of strange particles from the reaction between them. Direct production
 547 can be observed with $\pi + \pi \rightarrow \pi + \pi + \text{strange hadron} + \text{antiparticle}$, considering
 548 the baryon and strange number conservation. This means that, in order to create the
 549 strange particle and anti-particle at once, the reaction threshold (energy needed to
 550 produce mesons or baryons) corresponds to tow times the rest mass of the hadrons.
 551 (2230 MeV for $\Lambda + \bar{\Lambda}$, 2642 MeV for $\Xi + \bar{\Xi}$. 3344 MeV for $\Omega + \bar{\Omega}$)

552 **2. QGP** , where the degrees of freedom are partonic ones, with quarks and gluons free
 553 with respect to each other. The high gluon density gives the possibility to have
 554 new production mechanisms abreast the usual quark-pair annihilation which are the
 555 gluon fusion processes. It becomes the dominant process of $s\bar{s}$ pairs creation. In
 556 these reactions the energy threshold is equal to the naked mass of the two strange
 557 quarks $\approx 2 \cdot 100$ MeV.

558 The quarks can not be seen directly due to the strong interaction which keeps them
 559 confined. Once they are free, as in a QGP, the quarks recover their bare masses. (Note
 560 that, only the part of mass of hadron comes from the mass of the constituent quarks.) It
 561 was predicted that, if the QGP is formed, an enhancement of the strange quarks should

562 occur, because the production of $s\bar{s}$ pairs becomes easier due to the lower energy needed as
 563 explained above. When the QGP cools down, these strange quarks eventually recombine
 564 into hadrons favoring also an enhancement of the number of strange hadrons. This effect is
 565 larger for hadrons with higher strangeness, with the following scaling for the number type:
 566 Ordering in QGP: $N_\Omega > N_\Xi > N_\Lambda$

567 where N_Ω , N_Ξ , N_Λ are the number of produced Ω , Ξ and Λ . A certain enhancement of
 568 strange hadrons can occur also in a hadron gas system, but the processes of hadronisation
 569 in this case are relatively easy for K and Λ . and progressively harder for hadrons with
 570 higher strangeness, hence the relation would be:

571 Ordering in HG: $N_\Omega < N_\Xi < N_\Lambda$.

572 The measurement of multi-strange hadrons in heavy-ion collisions with respect to small
 573 collisions is considered to be a signature of the formation of the QGP and it was observed
 574 at SPS, RHIC and LHC. [24]

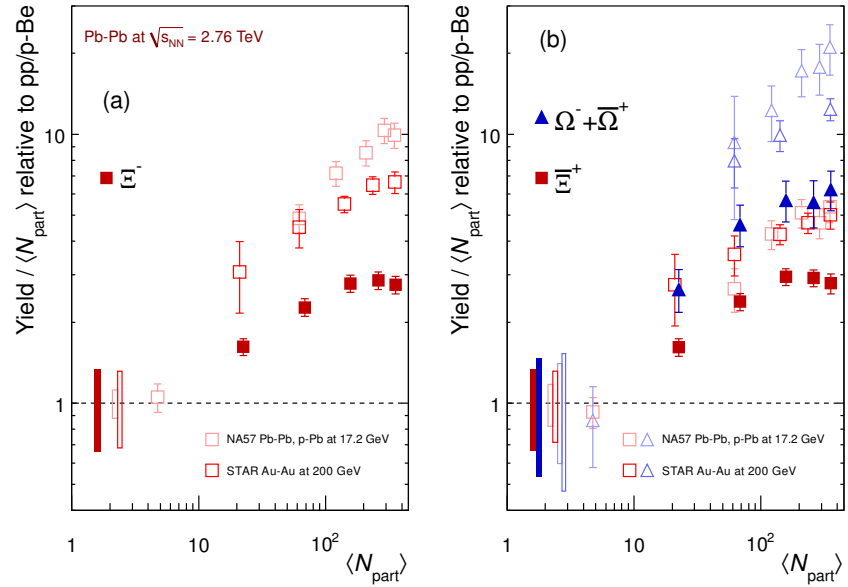


Figure 10: Integrated yield relative to small system (pp or p-Be) as a function of the mean number of participants $\langle N_{part} \rangle$ in the rapidity range $|y| < 0.5$. The results from ALICE are presented as full symbols, RHIC and SPS data are shown as open symbols. Boxes on the dashed line at unity represent statistical and systematic uncertainties on the pp or p-Be reference.

575 The measured enhancement factors of baryons with increasing strangeness content are
 576 reported in Figure 10 as a function of the mean number of participants, $\langle N_{part} \rangle$, compared
 577 with measurements at SPS and RHIC. As shown in the Figure 10, the enhancement in-

578 creases with $\langle N_{part} \rangle$ which is variable to be comparable to the centrality in Pb–Pb collisions
 579 and the effect is more pronounced for particle with larger strangeness content. If one con-
 580 sider the collision energy dependency, the comparison with measurement from the previous
 581 experiment shows that the relative enhancements decrease with increasing energy. This
 582 phenomena has been explained in terms of a statistical model via strangeness-canonical
 583 ensemble discussed in Section 2.1.

584 In a large system with a large number of produced particles, the conservation law of
 585 a quantum number, e.g., strangeness, can be implemented on the average by using the
 586 corresponding chemical potential. This is the Grand Canonical formulation that was dis-
 587 cussed in previous Section. In a small system, however, with small particles multiplicities,
 588 conservation laws must be implemented locally on an event-by-event basis. The Canonical
 589 formulation which conservation of quantum numbers reduce the possibility for strangeness
 590 particle production.[25]. This canonical suppression factor increase with higher energy in
 591 the center of mass of the collision and could explain the less enhancement in the results
 592 from higher energy system.

593 **3.2 Resonance production**

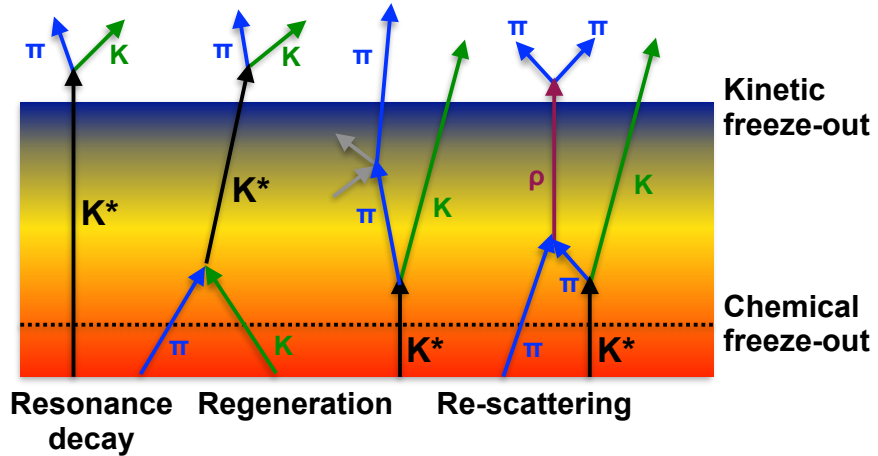


Figure 11: Hadronic phase

594 Resonances are particles with larger mass than the corresponding its ground state
 595 particle which has the same quark content. Because of the hadronic resonances decay
 596 strongly in the medium, it has short lifetime(τ) in the order of few fm/c which is comparable
 597 to the lifetime of the fireball. The natural width of resonances is $\Gamma = \bar{h}/\tau$, which is inverse
 598 proportion to the lifetime. In heavy ion collisions, the hadronic resonances are created in

599 medium which is still expanding so that the particles could interact with the medium and
600 decay while traveling it. The particles can be measured only via reconstruction of their
601 decay products in a detector, since it decays very shortly after being produced.

602 The effects which can be happened in the hadronic phase is shown in Figure 11. In the
603 left on the figure, as example, there is sketch of the original resonance decay of $K^*(892)^0$
604 ($K^*(892)^0 \rightarrow \pi + K$). It is possible that resonances may be regenerated via pseudo-elastic
605 scattering of decay products ($\pi + K \rightarrow K^*(892)^0 \rightarrow \pi + K$) in the time duration between the
606 chemical (T_{ch}) and the kinetic freeze-out (T_{kin}). Conversely, in case that the decay product
607 undergo elastic scattering or pseudo-elastic scattering through a different resonance in the
608 medium, e.g. ρ in the Figure 11, the invariant mass of the decay products can not mach
609 that of the parent particle. As a results, yield after kinetic freeze out could be smaller than
610 the yields originally produced.

611 These effects of re-scattering and regeneration could depend on the lifetime of the
612 resonances and influence the their integrated yield and momentum spectrum. The yield is
613 increase if the regeneration dominates, vice versa, it is decrease with re-scattering effect.
614 In order to understand the properties in hadronic medium, the ratios between resonances
615 and ground state hadrons have to be studies and the results are compared with model
616 predictions discussed in Section 2.

617 4 A Large Ion Collider Experiment at the LHC

618 ALICE (A Large Ion Collider Experiment) is one of major experiment at LHC (Large
619 Hadron Collider) in Geneva and it is dedicated experiment for the study of QCD matter
620 created in high-energy collisions [26]. It has been accumulating data during the whole first
621 phase of the LHC operation, from end of 2009 to the beginning of the technical shutdown
622 2013. During that time, the beam energy was tuned to have data in pp collisions at 0.9,
623 2.76, 7 and 8 TeV, p–Pb collisions at 5.02 TeV and Pb–Pb collisions at 2.76 TeV.

624 The section 4.1 aims to explain the LHC operation of the first phase and includes
625 each experiments builed in LHC. Next section (4.2.1) focuses on general description of
626 the ALICE detector and detailed explanation of sub-detectors used in this analysis will
627 given. And then the particle identification performance is discussed. The Data Acquisition
628 (DAQ) system and trigger system follow in Section 4.2.2. The last section account for
629 offline software frame work.

630 4.1 The Large Hadron Collider

631 The Large Hadron Collider (LHC) [27] at CERN is the world’s largest particle accelerator.
632 It provides maximum possible energies of 7 TeV for proton beam and 2.76 per nucleon
633 for beam of lead ions, hence, providing collisions at $\sqrt{s} = 14$ TeV and $\sqrt{s_{NN}} = 5.5$ TeV,
634 respectively. These energies are largest one ever achieved in particle collision experiment.

635 The LHC is a two ring superconducting hadron accelerator and collider built in the
636 26.7 kM tunnel. In separate parallel beam pipe, there are two counter-rotating beams
637 and the bunches of particles in each of them rotate many time up to collision energy is
638 approached to the desired value. The accelerator keeps to bend the beam around the ring
639 to maintain focused bunches and enlarge them to their collision energy. In the end, the size
640 of each bunches turns into minimized to obtain high luminosity guarantee a high number
641 of collisions per time interval at the collisions points. In order to achieve it, combination
642 of magnetic and electric field have been performed. In spite of the high luminosity, very
643 small portion of the particles from two bunches collides in a single bunch crossing. The
644 others are defocused and continue to rotate the ring.

645 The CERN accelerator complex is shown in the Figure 12. The sequence of injection of
646 bunches into the LHC is started from acceleration in the LINAC (LINEar ACcelerator)2,
647 PS (Proton Synchrotron) booster, PS, and SPS (Super Proton Synchrotron) accelerators.
648 The way to inject of heavy-ion bunches are different. The bunches pass the LINAC3 instead
649 of LINAC2, LEIR (Low Energy Ion Ring), PS and SPS accelerators [28].

650 The first pp collisions at 900 GeV center of mass energy were delivered by the LHC on
651 September 10th 2008. Nine days later, the operations were interrupted due to a failure in
652 an electrical connection between two magnets. The machine operators spent over a year
653 repairing and consolidating the accelerator. On November, 2009 low energy proton beams
654 circulated again, and a few days later, by achieving the energy of 1.18 TeV per proton

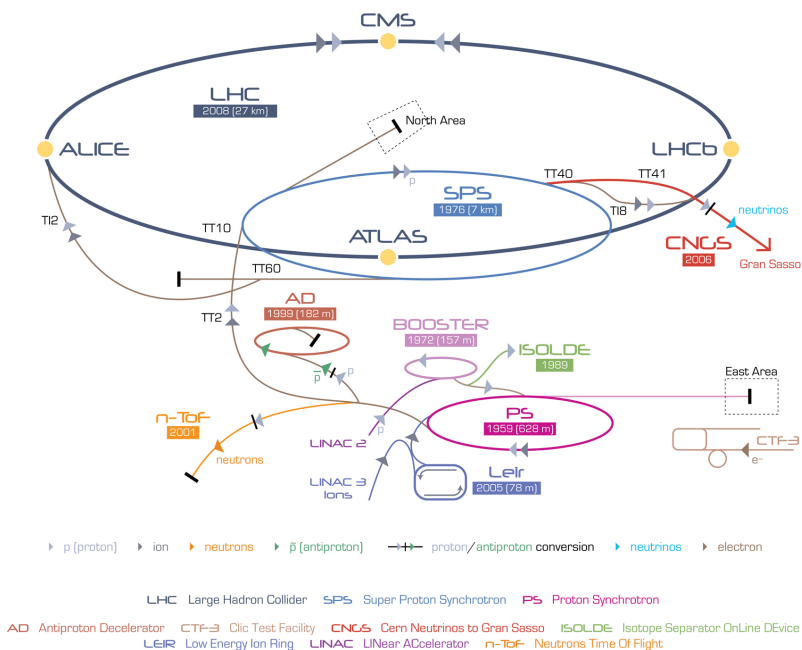


Figure 12: The CERN accelerator complex [3]

beam, LHC became the most powerful accelerator in the world. The first pp collisions at center of mass energy of 7 TeV were delivered in March 2010, and the first Pb–Pb collisions at center of mass energy of 2.76 TeV per nucleon pair in November 2010.

In 2010 the integrated luminosity delivered by the LHC was $\sim 48 \text{ pb}^{-1}$ for pp collisions at $\sqrt{s} = 7 \text{ TeV}$ ($\sim 0.5 \text{ pb}^{-1}$ in ALICE) and $\sim 10 \text{ } \mu\text{b}^{-1}$ for Pb–Pb at $\sqrt{s_{\text{NN}}} = 2.76 \text{ TeV}$ ($\sim 9 \text{ } \mu\text{b}^{-1}$ in ALICE) [26]. In 2011 the beam energy was the same as in 2010 both for pp and Pb–Pb. The performance of the LHC improved in terms of luminosity with $\sim 5.61 \text{ fb}^{-1}$ for pp ($\sim 4.9 \text{ pb}^{-1}$ in ALICE) and $\sim 166 \text{ } \mu\text{b}^{-1}$ for Pb–Pb collisions ($\sim 146 \text{ } \mu\text{b}^{-1}$ in ALICE). In 2012, the centre-of-mass energy for pp collisions was brought to 8 TeV and the integrated luminosity (up to December 2012, end of the pp program) was $\sim 23.3 \text{ fb}^{-1}$ ($\sim 10 \text{ pb}^{-1}$ in ALICE). A pilot p–Pb run operated at $\sqrt{s_{\text{NN}}} = 5.02 \text{ TeV}$ on September 2012, followed by a long p–Pb run on February 2013 with a delivered luminosity of 14 nb^{-1} . A very short pp run at $\sqrt{s} = 2.76 \text{ TeV}$ ended the Run1 of the LHC program, marking the start of the first long shutdown (LS1) until the end of 2014.

The LHC produces collisions in four so called Interaction Points (IPs) in correspondence of which are located six detectors of different dimensions and with different goals, all able to study the products of the interactions. These are:

ALICE (A Large Ion Collider Experiment-IP₂) [29] is devoted heavy-ion experiment intended to investigate strongly interacting matter at very high energy density. It explores the phase transition to the QGP phase diagram and its properties. Furthermore, the ALICE study the results of pp and p–Pb collisions, as a reference for heavy-ion measurements. ALICE is able to measure identified particles by using excellent particle identification capability and its acceptance reached to very low transverse momenta.

ATLAS (A Toroidal LHC ApparatuS-IP₁) and CMS (Compact Muon Solenoid - IP₅) [30][31] are built to cover the widest possible range of physics at the LHC and they are dedicated to collect results from pp collisions. Specific topics are the beyond the Standard Model and serch for the Higgs boson.

LHCb (The Large Hadron Collider beauty experiment-IP₈) [32] is a dedicated experiment for the study of heavy flavor physics at the LHC. In particular, the experiment focuses on the study of CP violation and rare decays of beauty and charm particles, to test the Standard Model and to search for evidence of New Physics. The LHCb physics program is complementary to the flavor physics studies and to the direct exploration for new particles performed at ATLAS and CMS.

TOTEM (TOTal Elastic and diffractive cross-section Measurement-IP₅) [33] is dedicated to the measurement of the total pp cross-section, study of elastic and diffractive scattering. The detector is built at the same interaction point of the CMS experiment.

696 **4.2 The ALICE project**

697 The main goal of the ALICE experiment at the LHC [34] is study of matter produced
698 extreme conditions of temperature and energy density from ultra-relativistic heavy-ion
699 collisions. The purpose is to inspect the existence of a phase transition from the hadronic
700 matter to the QGP which was proposed by QCD prediction. Because only ALICE is the
701 LHC experiment specifically designed for Pb–Pb collisions, it has to be able to cope with
702 the large multiplicities associated with these collision systems and at the same time has to
703 cover as many QGP-related observables as possible. ALICE is also interested in the results
704 of pp interactions, since these are the baseline for the results obtained Pb–Pb collisions. It
705 is not only crucial for comparison with Pb–Pb but also can be used to tune Monte Carlo
706 models.

707 In comparison with the other experiments, ALICE is able to provide an excellent Particle
708 IDentification (PID) performance obtained by combination of different PID techniques
709 from various detectors that are optimized in different momentum (p) regions.

710 **4.2.1 ALICE detector**

711 ALICE is a complex of 14 detector subsystems (Figure 13) that can be categorized in three
712 groups:

713

714 **Central detectors** are installed in a solenoid magnet which gives 0.5 T magnetic field
715 and covered pseudo-rapidity interval is $-0.9 < \eta < 0.9$ (corresponding to a polar acceptance
716 $\pi/4 < \theta < 3\pi/4$). The acceptance in azimuthal angle is 2π . The central detectors
717 are mainly used to vertex reconstruction, tracking, particle identification and momentum
718 measurement. From interaction region to outward region of detector, there are several
719 detectors explained below:

- 720
 - 721 • Inner Tracking System (ITS)
 - 722 • Time Projection Chamber (TPC)
 - 723 • Transition Radiation Detector (TRD)
 - 724 • Time Of Flight (TOF)

725 Following three detectors have limited azimuthal acceptance in the mid-rapidity region:

- 726
 - 727 • High Momentum Particle Identification Detector (HMPID)
 - 728 • PHOton Spectrometer (POHS)
 - 729 • ElectroMagnetic CALorimeter (EMCAL)

728 **Muon spectrometer** is located in the forward pseudo-rapidity region ($-4.0 < \eta < -2.5$) and is made up of a dipole magnet and tracking and trigger chambers. It has been
729 optimized and configured to extract single muons and to reconstruct heavy quark reso-
730 nances (such as J/Ψ through their $\mu^+ \mu^-$ decay channel).

732 **Forward detectors** are placed in the high pseudo-rapidity area (small angles with
733 respect to the beam pipe). They are used to measure global event characteristics and for
734 triggering.

- 736 • Time Zero (T0) measures the time of events with precision of the order of tens of
737 picoseconds, as needed by TOF.
- 738 • VZERO (V0) rejects the backgrounds coming from beam-Gas interaction and trigger
739 minimum bias events.
- 740 • Forward Multiplicity Detector (FMD) gives multiplicity information and it covers
741 large fraction of the solid angle ($-3.4 < \eta < -1.7$ and $1.7 < \eta < 5$).
- 742 • Photon Multiplicity Detector (PMD) measures the spatial distribution of photons on
743 an event-by-event basis in $2.3 < \eta < 3.7$ region.
- 744 • Zero Degree Calorimeter (ZDC) is used to measure and trigger on the impact param-
745 eter. The ZDC consists of two calorimeters, one for neutrons (ZDC:ZN) and another
746 one for protons (ZDC:ZP), and includes also an electromagnetic calorimeter (ZEM)

747 The ALICE global coordinate system [35] is a right-handed orthogonal Cartesian system
748 with the origin X, Y, Z = 0 at the centre of the detector. The three Cartesian axes are
749 defined as follows: the X axis pointing towards the center of the LHC, the Y axis pointing
750 upward and the Z axis parallel to the local mean beam line pointing in the direction opposite
751 to the muon spectrometer. The azimuthal angle increases counter-clockwise from the
752 positive X axis ($\Phi = 0$) to the positive Y axis ($\Phi = \pi/2$) with the observer standing at
753 positive Z and looking at negative Z; the polar angle increases from the positive Z axis (θ
754 = 0) to the X-Y plane ($\theta = \pi/2$) and to the negative Z axis ($\theta = \pi$).

755 In the following Sections more specific descriptions of the detectors used in the identi-
756 fication of the $\Xi(1530)^0$ baryons and in the determination of the characteristics of typical
757 collisions will be given.

758 **ITS**

759 The ITS [34] (Figure 14) is the barrel detector which is closest to the beam pipe. Its main
760 purposes are:

- 762 • to contribute to the global tracking with the TPC by improving the angle and mo-
763 mentum resolution

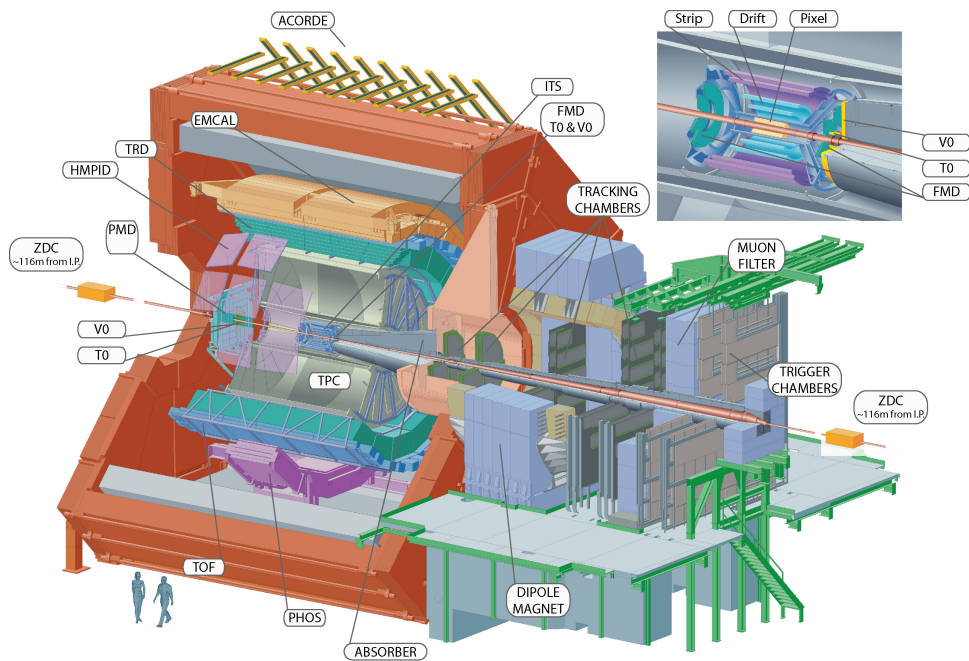


Figure 13: The ALICE detector

- 764 • to reconstruct the position of the primary interaction vertex
- 765 • to reconstruct strange particle decays and secondary vertices from decays of heavy-
766 flavor
- 767 • to track and identify particles with momentum below $100 \text{ MeV}/c^2$
- 768 • to improve the momentum, impact parameter and angle resolution for the measure-
769 ment of high p_T particles performed with the TPC
- 770 • to reconstruct particles traversing dead regions of the TPC

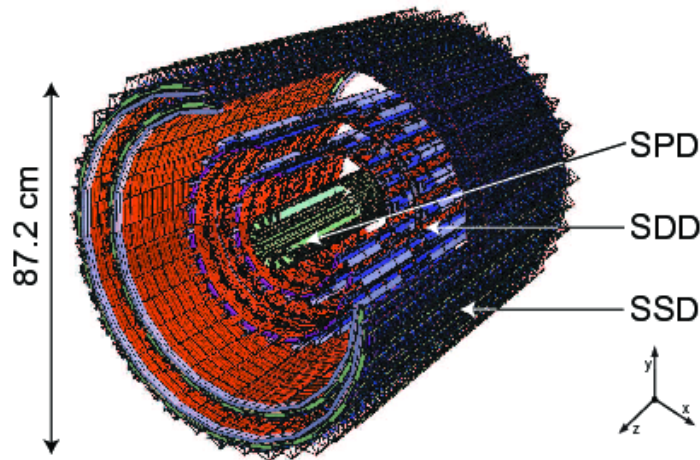


Figure 14: Schematic view of the ITS [4]

771 The ITS encircles the beam pipe which is a $800 \mu\text{m}$ thickness cylinder shape with an
772 outer diameter of 2.9 cm . It consists of six layers of silicon detectors placed at radii from ~ 4
773 cm to $\sim 43 \text{ cm}$. The two innermost layers are Silicon Pixel Detectors (SPD), Silicon Drift
774 Detectors (SDD) is placed in middle and the two outmost layers are Silicon micro-Strip
775 Detectors (SSD).

776 The amount of material in the detector has to be minimized because the momentum
777 and impact parameter resolutions for low momentum particles are dominated by multiple
778 scattering effects. The track impact parameter resolution as function of p_T is shown in
779 Figure 15. The ITS detector has a spatial resolution better than $70 \mu\text{m}$ in the $(r\phi)$ for $p_T >$
780 $1 \text{ GeV}/c$.

781

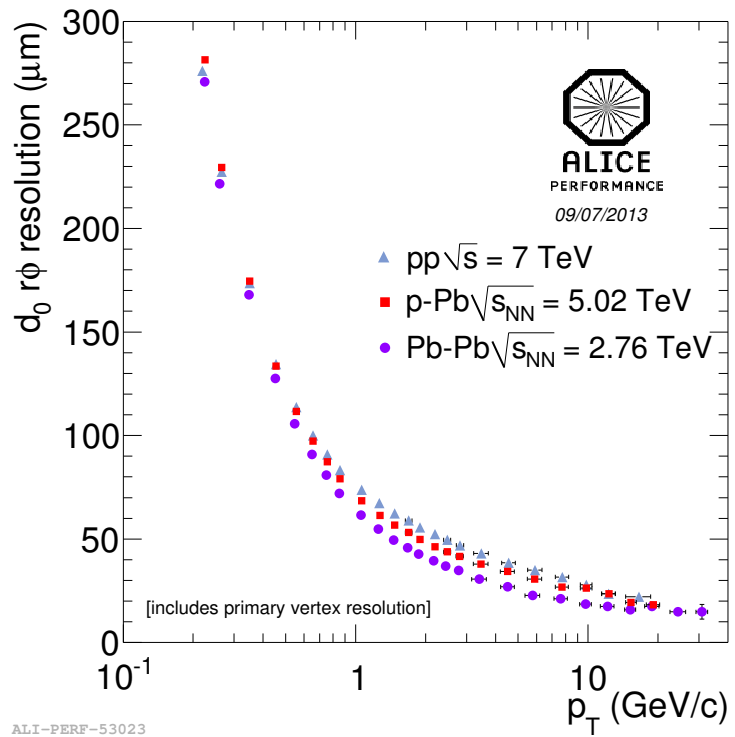


Figure 15: Track impact parameter resolution ($r\phi$) in the transverse plane as function of p_T for charged particle

782 **TPC**

783

784 The TPC [36] (Figure 16) is the main tracking detector of the central barrel optimized
785 to measure charged particle momentum with good track separation, particle identification
786 and vertex determination. In order to get the track in high multiplicity environment of
787 Pb–Pb collisions, the TPC was designed to have an excellent tracking performance. For
788 such reason, it was constructed as a drift chamber in 5 m cylindrical shape. The inner
789 radius is $r_{in} \sim 85$ cm decided by the maximum acceptable track density and the most outer
790 radius is $r_{out} \sim 250$ cm to minimize track length for which dE/dx is $< 10\%$. The volume
791 of TPC is 90 m^3 and it is filled by $\text{Ne}/\text{CO}_2/\text{N}_2$. The readout chambers are installed at
792 the two endplates of the cylinder. Their design is based on the Multi-Wire Proportional
793 Chamber (MWPC) technique with pad readout. The TPC has good dE/dx resolution as
794 results it is able to identify particles with $p_T < 1 \text{ GeV}/c$ on a track-by-track basis.

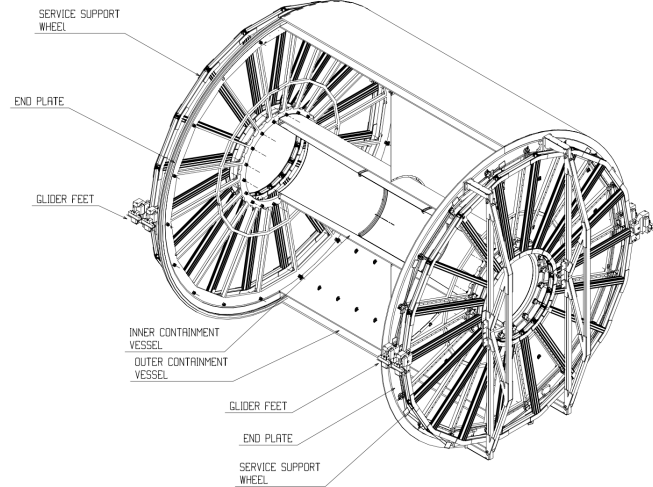


Figure 16: Schematic view of the TPC

795 The gas in the detector is ionized by charged particle traveling through the TPC. The
796 measurement of this loss of energy is what we need to identify a particle. The physics
797 observable in this case is the energy loss per unit length, within the matter crossed by
798 the charged particle, which we call specific energy loss, also denoted by dE/dx . This
799 is described by the Beth–Bloch equation, 5, that highlights the key of the identification
800 technique: this observable depends only on the charge and on velocity (β) of the particle,
801 which, in turn, depends only on the momentum and the mass of the ionizing particle.
802 Since momentum is already known due to track curvature and charge is unitary for most
803 measured tracks, measuring the dE/dx allows us to indirectly determine mass and thus

804 determine the particle species. The Bethe-Bloch equation gives the mean specific energy
 805 loss:

$$-\langle \frac{dE}{dx} \rangle = k_1 \cdot z^2 \frac{Z}{A} \cdot \frac{1}{\beta^2} \left[\frac{1}{2} \ln(k_2 \cdot m_e c^2 \cdot \beta^2 \gamma^2) - \beta^2 + k_3 \right] \quad (5)$$

806 where $\beta\gamma = p/Mc$ and: Z: atomic number of the ionized gas (in this case Ne/CO₂/N₂)
 807 A: mass number of the ionized gas (g/mol)
 808 m_e : electron mass
 809 z: electric charge of the ionizing particle in unit of electron charge e
 810 M: ionizing particle mass
 811 p: ionizing particle momentum
 812 β : ionizing particle velocity normalized to the light velocity c
 813 $\gamma = 1/\sqrt{1 - \beta^2}$, Lorentz factor
 814 k_1, k_2, k_3 : constants depending on the ionized medium
 815

816 For a given ionizing particle mass hypothesis, a given momentum and a given length
 817 of the trajectory in the ionizing medium, the total charge deposited along the trajectory
 818 is subject to statistical fluctuations. This random variable follows a Landau distribution,
 819 that give us the opportunity to measure the mean value $h dE/dx$. The long tail of the
 820 Landau distribution is usually truncated at 50%-70% of the collected signal.

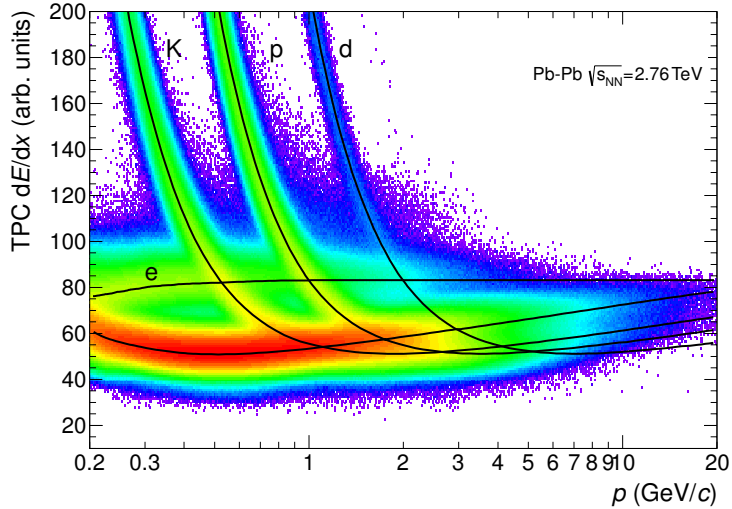


Figure 17: Specific energy loss (dE/dx) in the TPC as a function of momentum in Pb–Pb collisions at $\sqrt{s_{NN}} = 2.76$ TeV. The lines show the parameterizations of the expected mean energy loss.

821 The specific energy loss in the TPC as a function of momentum is shown in Figure

822 17. The different bands characteristic for e^\pm , π^\pm , K^\pm , p^\pm are clearly visible. These
 823 are the evidence of the statistical distribution of the measured energy loss around the
 824 expected mean value. The expected value correspond to the prediction by a Bethe–Bloch
 825 experimental parametrization (superimposed as black lines in the Figure). For a track
 826 within the TPC the relevant quantity to be considered for PID is the difference between
 827 the specific energy loss measured by detector and the corresponding predicted value, by
 828 the Bethe-Bloch parametrization for a given measured momentum. If normalized to the
 829 resolution of the dE/dx measurement in the TPC, this difference could be expressed in
 830 number of σ (see Equation 6). In this way it is possible to estimate more quantitatively the
 831 goodness of a mass hypothesis. This also gives us the possibility to choose the strictness
 832 we want to adopt in the identification of a particle (n_σ , $n = 2, 3, 4$):

$$n_\sigma = \frac{(dE/dx)_{measured} - (dE/dx)_{Bethe-Bloch}}{\sigma_{TPC}} \quad (6)$$

833 *V0*

834 The VZERO detector [37] consists of two segmented arrays of plastic scintillator counters,
 835 called VZERO-A and VZERO-C, placed near the beam-pipe on each side of the interaction
 836 point: one at $Z = 340$ cm, covering the pseudo-rapidity range $(2.8 < \eta < 5.1)$, and the
 837 other at $Z = -90$ cm in front of the absorber, covering the pseudo-rapidity range $(-3.7 < \eta <$
 838 $-1.7)$.

839 By measuring the relative time of flight, the VZERO reject background from beam-gas
 840 collisions. (see, Figure 19) The time of flight of particles coming from the interaction point
 841 to the VZERO-A is ~ 11 ns while VZERP-C is 3 ns. If the beam-gas collision takes place
 842 outside the region between the two arrays, particles arrive 6 ns before or after the time of a
 843 beam-beam collisions. When the beam-gas collision takes place outside the region between
 844 the two arrays, particles arrive 6 ns before or after the time of a beam-beam collision as
 845 shown in Figure ??

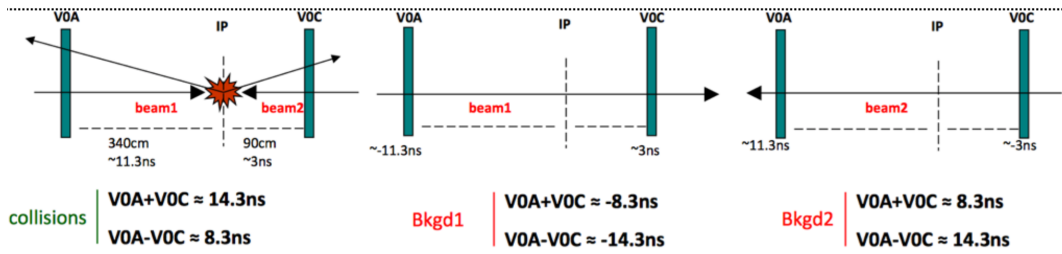


Figure 18: Sketch of events collisions at $(8.3$ ns, 14.3 ns) is shown in left, background from Beam 1 at $(-14.3$ ns, -8.3 ns) in in middel and background from Beam 2 at $(14.3$ ns, 8.3 ns) is in right.

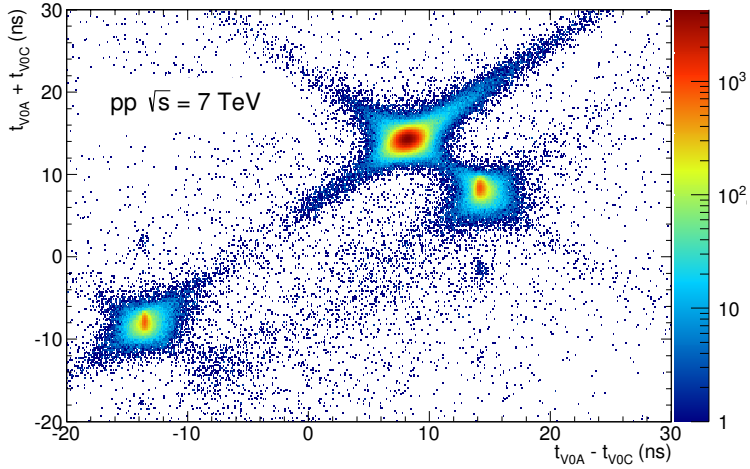


Figure 19: Correlation between the sum (y-axis) and difference (x-axis) of signal times in V0A and V0C. The signals in center come from beam-beam interactions, the signal in left is background from Beam1 and background from Beam2 is shown in right hand.

846 As the VZERO is a trigger detector, it will provide a minimum-bias trigger for all
 847 colliding systems to the central barrel detectors and different centrality triggers in p–Pb
 848 and Pb–Pb collisions (e.g. multiplicity, central and semi-central).

849 The first parameter to be determined in A–A(p–A) collisions is the centrality(multipliciy).
 850 This is defined according to the value of the impact parameter, b , and provides a geomet-
 851 rical scale of the overlapping region between the colliding nuclei: a collision will be defined
 852 from central to peripheral, as the impact parameter increases. The centrality of a col-
 853 lision is not directly available and must be deduced from a combination of experimentally
 854 measured quantities and Monte Carlo simulations.

855 The charged-particle multiplicity N_{ch} is observable that can be measured and used as
 856 centrality estimator and it is related to N_{part} . The variables increase significantly increasing
 857 the centrality of the collisions. Another measurable quantity to estimate the centrality is
 858 the zero-degree energy EZDC, namely the energy carried by spectator nucleons $N_{spec} =$
 859 $2A - N_{part} = EZDC/E_A$, where E_A is the beam energy per nucleon. Typically a measured
 860 distribution of one of the previous observables is mapped to the corresponding distribution
 861 obtained from phenomenological Glauber calculations. The Glauber model [38, 39] uses
 862 a semi-classical approach: the A–A collision is assumed to be an incoherent superposition
 863 of N elementary nucleon- nucleon collisions. The main parameters of the model are the
 864 inelastic nucleon-nucleon collision cross-section σ_n and the nuclear density distribution
 865 $\rho(r)$. In practice, the simulated distribution well reproduce the measured distribution or

866 the latter is fitted with an analytical function. The experimental distribution can then
867 be divided in classes with sharp cuts on the measured observable (E_{ZDC} , E_T or N_{ch}).
868 These "centrality" classes will correspond to well defined percentage of the integral of the
869 distribution. A given centrality class in the measured distribution, corresponds to the
870 same class in the simulated distribution, where the main geometrical variables (N_{part} , N_{coll}
871 and T_{AA}) can be determined. The number of classes that can be defined depends on the
872 resolution achievable on the selection variable. In the analysis described in this thesis
873 the centrality(multiplicity) estimation is based on the measurement of the multiplicities
874 from the VZERO scintillators [40][41]. This is the method that achieve the best centrality
875 resolution: it ranges from 0.5% in central to 2% in peripheral collisions. Other methods,
876 as the ones based on the E_{ZDC} measurement or based on the estimate of the number of
877 tracks in the SPD or TPC, are used to asses a systematic uncertainty on the centrality
878 determination. The distribution of the VZERO amplitudes is shown in Figure 20 where
879 the centrality(multiplicity) percentiles are also indicated.

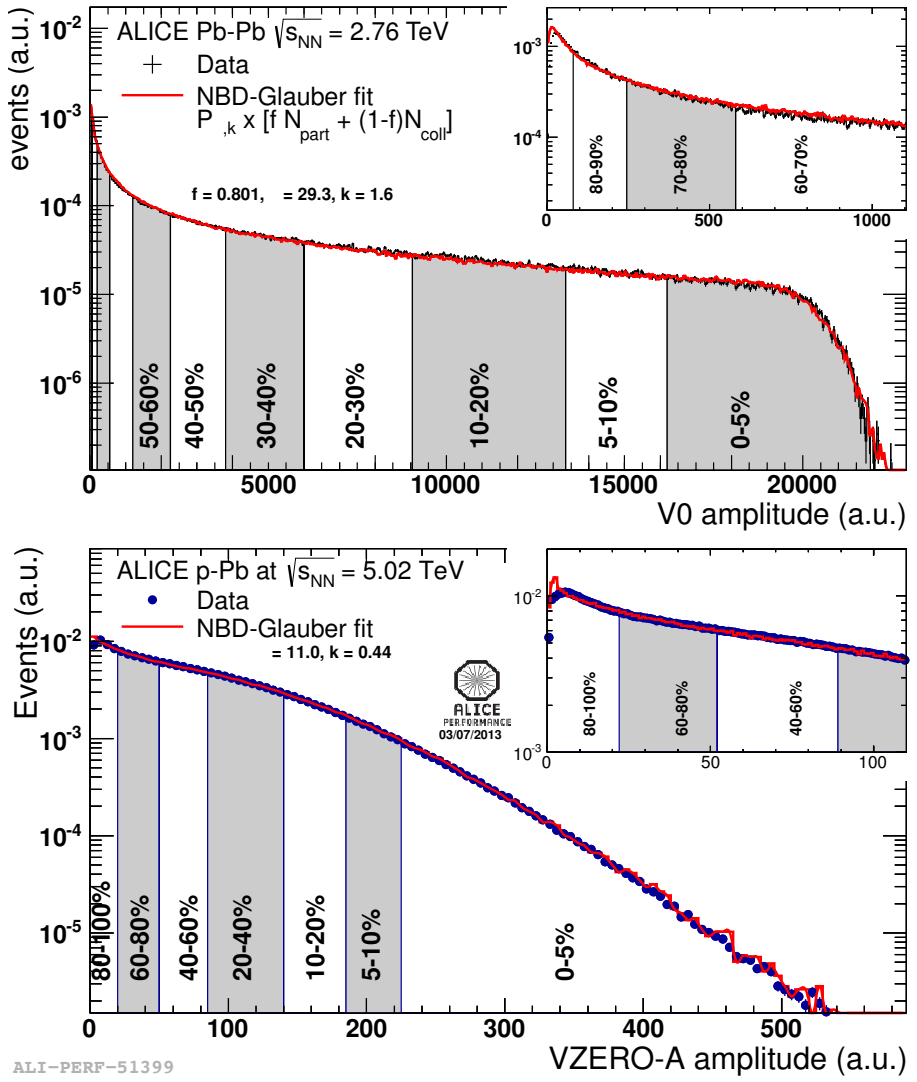


Figure 20: Sum of V0A and V0C amplitude distribution in top and V0A amplitude distribution in bottom.

880 **4.2.2 Data Acquisition (DAQ) and trigger system**

881 The architecture of data acquisition is shown in Figure 21. The tasks of the ALICE DAQ
 882 system are the assembly of event informations from individual detectors into complete
 883 events (event building) as well as buffering and export of assembled events to permanent
 884 storage.

885 The DAQ is designed to process a data rate up to 1.25 GB/s in heavy-ion runs. Event
 886 building is done in two steps. Data from the detectors is received by Detector Data Links
 887 (DDLs) on Local Data Concentrators (LDCs). The LDCs assemble the data into sub-
 888 events that are then shipped to Global Data Collectors (GDCs). A GDC re- ceives all
 889 sub-events from a given event and assembles them into a complete event. These events are
 890 subsequently stored on a system called Transient Data Storage (TDS).

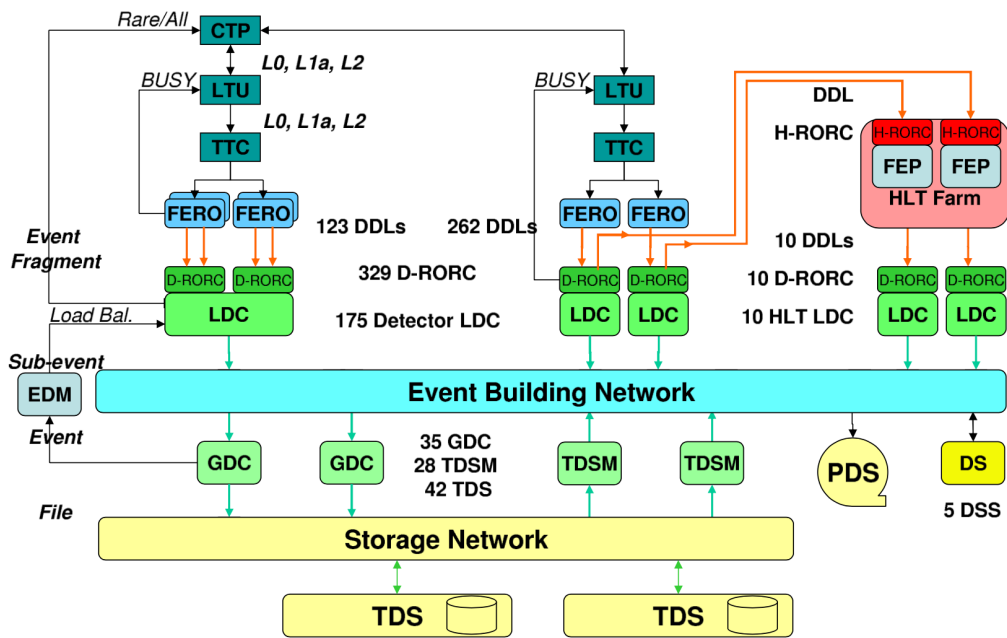


Figure 21: The overall architecture of the ALICE DAQ and the interface to the HLT system.

891 ALICE can simultaneously take data in several partitions, where a set of detec-
 892 tors can store their outputs. Since a partition is a group of commonly controlled detectors, a
 893 given detector can only be active in one partition at a time. The ac- tive detectors in a

894 given partition may be assigned to data taking groups called clusters, for which triggers
895 can be defined. Therefore, upon a trigger only a sub- set of the whole partition may
896 be read out. Furthermore, a triggering detector does not have to be necessarily part of
897 the partition. ALICE has a two-layer trigger architecture [42]. The low-level trigger is a
898 hardware trigger called Central Trigger Processor (CTP). The High-Level Trigger (HLT)
899 is implemented as a pure software trigger. The CTP combines inputs from different trigger
900 sources, namely the various detectors. These inputs are single signals, like a hit in the
901 detector, or, can be the result of fast calculation performed directly in the detectors. The
902 HLT allows the implementation of sophisticated logic for the triggering. In contrast to the
903 CTP which governs the readout of the detectors, the HLT receives a copy of the data read
904 out from the detectors and processes them. The hardware trigger combines the trigger
905 signals of the various detectors to decide if an event is accepted, that means it is read out
906 and written to disk. Several trigger levels reduce the event rate depending on the input
907 signals. The first level, called L0, is delivered after 1.2 ?s, while the second, called L1,
908 after 6.5 ?s. The final trigger, L2, is delivered after 100 ?s, upon completion of the drift
909 time in the TPC. Only after an L2 trigger the event is finally stored. The rates of different
910 trigger classes are very different. By definition minimum-bias triggers have the highest
911 rate; other triggers that look for rare signals are characterized by much lower rates. In
912 order to cope with different scenarios, downscaling factors can be applied to the trigger
913 classes individually, i.e. only every nth event fulfilling the trigger condition is read out. The
914 total recording rate is limited by the maximum bandwidth of data that can be recorded
915 to disk and tape. The ALICE software trigger, called HLT, is a farm of multiprocessor
916 computers. The aim is to have about 1000 PCs processing the data in parallel allowing
917 an online analysis of the events. A trigger decision comes from the analysis of a more
918 comprehensive set of information than what happens for the hardware trigger, giving the
919 possibility to apply more sophisticated triggers. Examples include triggers on high energy
920 jets or on muon pairs. Furthermore, the HLT can significantly reduce the event size by
921 selecting regions of interest (partial readout of detectors) and by further compression of the
922 data. The HLT receives a copy of the raw data and performs per detector reconstruction,
923 partly aided by hardware coprocessors. Subsequently, the trigger decision is based on the
924 global reconstructed event. In the same step a region of interest can be selected. In the
925 last optional step, if the trigger decision is positive, the data are compressed. The trigger
926 decision, partial readout information, compressed data, and the re- construction output
927 is sent to LDCs and subsequently processed by the DAQ. In terms of the overall DAQ
928 architecture, data sent by HLT is treated like stemming from a detector.

929 **4.2.3 ALICE offline software frame work**

930 In order to reconstruct, analyze the raw data as well as the product simulated events, the
931 computing power and resources are required. The ALICE uses decentralized computing
932 system called Grid [43].

933 The Grid paradigm is the unification of resources of distributed computing center,
934 especially, computing power and storage, to provide them to users all over the World. It
935 allows to provide their resources to wider community and the makes local resources to be
936 shared with entire collaboration. Software which is implements the Grid is called Grid
937 middleware. ALICE has developed a Grid middleware called AliEn [44] that is set of tools
938 and services. An ALICE user employs AliEn to connect to the ALICE Grid which is
939 composed of a combination of general services that are provided by many Grid middleware
940 solutions and ALICE-specific services provided by AliEn. Parts of the ALICE Grid are:
941 i) a global file catalog that is a directory of files in storage elements distributed over the
942 Globe, ii) the automatic matching of jobs for execution to a suitable location in one of
943 the connected sites, iii) a shell-like user interface and iv) API9 services for the ROOT
944 framework [45].

945 AliRoot [34] is the offline framework for simulation, alignment, calibration, reconstruction,
946 visualization, quality assurance, and analysis of experimental and simulated data. It
947 is based on the ROOT framework. Most of the code is written in C++ with some parts
948 in Fortran that are wrapped inside C++ code. Re-usability and modularity are the basic
949 features of the AliRoot framework. Modularity allows parts of the code to be replaced,
950 with minimum or no impact on the rest (for example changing the event generator, the
951 transport Monte Carlo or the reconstruction algorithms). This is achieved implementing
952 abstract interfaces. In addition codes for each detector subsystem are independent modules
953 with their specific code for simulation and reconstruction and the code can be developed
954 concurrently with minimum interference. Re-usability is meant to maintain a maximum
955 amount of backward compatibility as the system evolves.

956 The central module of the AliRoot framework is STEER (Figure 22) which provides
957 several common functions such as: steering of program execution for simulation, reconstruction
958 and analysis; general run management, creation and destruction of data structures,
959 initialization and termination of program phases; base classes for simulation, event generation,
960 reconstruction, detectors elements. For event simulation the framework provides the
961 following functionality:

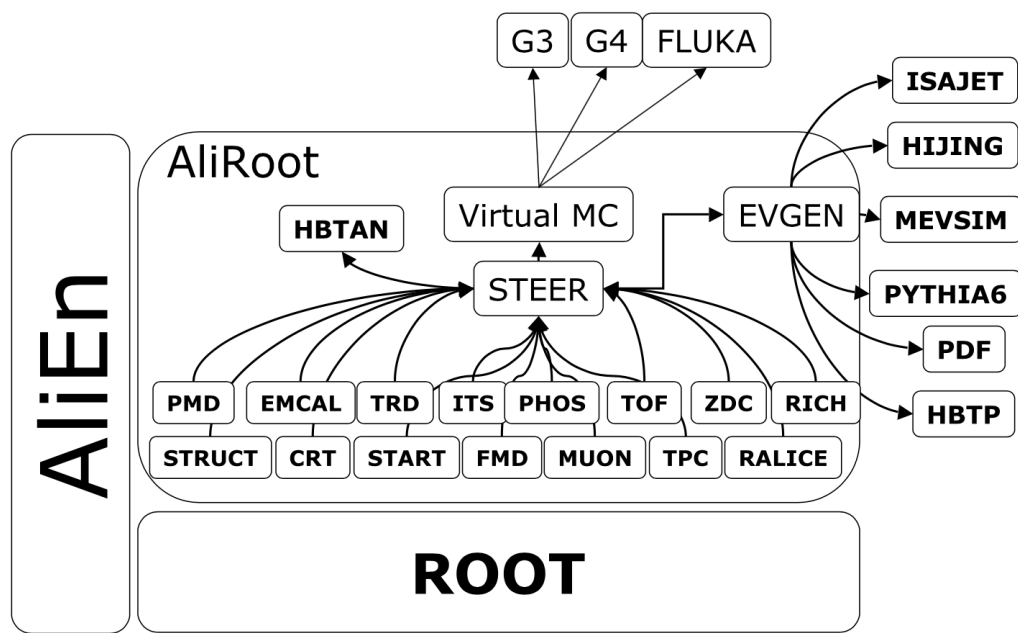


Figure 22: Schematic view of the AliRoot framework

962 **5 Measurement of $\Xi(1530)^0$ production in p–Pb and Pb–Pb**

963 The measurement of hyperon resonance production in p–Pb collisions helps to disentangle
964 cold nuclear matter effects from genuine hot medium effects and contribute to the study of
965 the system size dependence of re-scattering and regeneration in the hadronic phase. And
966 the measurement in ultra-relativistic heavy-ion collisions such as Pb–Pb collisions, allows
967 to study the properties of hadronic medium and different stage of its evolution. In order to
968 study the particle production mechanism in the hadronic phase between the chemical and
969 kinetic freeze-out, the $\Xi(1530)^0$ resonance at mid-rapidity ($-0.5 < y_{\text{CMS}} < 0$) is measured
970 in p–Pb collisions $\sqrt{s_{\text{NN}}} = 5.02$ TeV and in Pb–Pb collisions with $|y| < 0.5$ at $\sqrt{s_{\text{NN}}} = 2.76$
971 TeV with the ALICE by the reconstruction of hadronic decay into $\Xi\pi$.

972 **5.1 $\Xi(1530)^0$ -reconstruction**

973 The Ξ^{*0} production in p–Pb and Pb–Pb collisions at mid-rapidity has been studied in
974 different multiplicity and centrality classes, from peripheral to central collisions including
975 minimum bias events. The analysis is based on the invariant mass of the reconstructed
976 pairs which might be the decay of a Ξ^{*0} baryon into charged particles. The daughter
977 particles which are decay products are identified as oppositely charged Ξ and π among the
978 tracks reconstructed in the central barrel. In section 5.1.1, the event selection and track
979 selection applied in this analysis, and the particle identification is explained. Then, the raw
980 yield from signal is extracted by integrating the fit on the background-subtracted invariant
981 mass distribution of $\Xi\pi$ in several transverse momentum. To obtain the corrected p_{T} -
982 spectra, the raw yields are corrected for acceptance and efficiency ($\text{Acc} \times \epsilon_{\text{rec}})(\text{pt})$ which
983 is computed using Monte Carlo simulation. By dividing for the number of the events in
984 each multiplicity and centrality classes, the normalization on the spectra is performed.

985 **5.1.1 Data sample and event selection**

986 A description of the ALICE detector and of its performance during the LHC Run 1 (2010–
987 2013) can be found in [34, 26]. The data sample in the analysis from Pb–Pb collisions with
988 energy of $\sqrt{s_{\text{NN}}} = 2.76$ obtained during 2011 and the sample of p–Pb run at $\sqrt{s_{\text{NN}}} = 5.02$
989 TeV was recorded in 2013.

990 Due to the asymmetric energies of the proton (4 TeV) and lead ion (1.57 A TeV) beams,
991 the centre-of-mass system in the nucleon-nucleon frame is shifted in rapidity by $\Delta y_{\text{NN}} =$
992 0.465 towards the direction of the proton beam with respect to the laboratory frame of
993 the ALICE detector [6]. For the analysed p–Pb data set, the direction of the proton beam
994 was towards the ALICE muon spectrometer, the so-called “C” side, standing for negative
995 rapidities; conversely, the Pb beam circulated towards positive rapidities, labelled as “A”
996 side in the following. The analysis in this paper was carried out at midrapidity, in the
997 rapidity window $-0.5 < y_{\text{CMS}} < 0$.

998 The minimum bias trigger during the p–Pb run was configured to collect events by
999 requiring a logical OR of signals in V0A and V0C [26], two arrays of 32 scintillator detectors
1000 covering the full azimuthal angle in the pseudo-rapidity regions $2.8 < \eta_{\text{lab}} < 5.1$ and
1001 $-3.7 < \eta_{\text{lab}} < -1.7$, respectively [46]. In the data analysis it was required to have a
1002 coincidence of signals in both V0A and V0C to remove the events from single-diffractive
1003 and electromagnetic interactions.

1004 Out of this sample in p–Pb collision events about 109.3 million events, 93.9 million
1005 events pass the following selection criteria and have been used for the analysis.

1006 The Pb–Pb collisions data sample was selected by online centrality trigger requiring a
1007 signal in the forward V0 detectors[41] to record enhanced data in central collision. The
1008 data consists of 24.8 million events in most central collisions (0-10%), 21.8 million events in
1009 semi-central collisions (10-50%) and 3.5 million events with minimum-bias trigger (0-90%).
1010 Among 49.6 million events in total, 43.0 million events have been analyzed as passed the
1011 criteria below.

- 1012 • Events with z-position of primary vertex (V_z) within ± 10 cm of the center of
1013 TPC/ITS
- 1014 • Rejection of pile-up event
- 1015 • Requiring primary tracks to have at least one hit in SPD
- 1016 • p–Pb: multiplicity ranges in percentile (V0A): 0-20%, 20-40%, 40-60%, 60-100% and
1017 MB(0-100%)
- 1018 • Pb–Pb: centrality classes (V0A and V0C): 0-10%, 10-40%, 40-80% and MB (0-80%)

1019 The distribution of the V_z of the accepted events in p–Pb collision is reported on left
1020 panel in Figure 23 and corresponding figure but obtained from Pb–Pb collisions is shown
1021 on right panel in Figure. 23. Events with $|V_z| < 10$ cm have been used to make sure
1022 that the tracks have been obtained from uniform acceptance in the central pseudo-rapidity
1023 region, $|\eta| < 0.8$, where the analysis is performed. This cut reduces the total number of
1024 events to 97.5 million events, that is the $\sim 89.2\%$ of the initial sample in p–Pb collisions and
1025 43.04 million events which is $\sim 86.8\%$ of the initial sample in Pb–Pb collisions are survived.

1026 Fig. 24 shows the multiplicity distribution of the accepted events in p–Pb collision
1027 divided in bins of percentile. The each color on the histogram indicate the multiplicity
1028 ranges used in this analysis. Corresponding events for each multiplicity range are in Table
1029 8.

1030 The distribution of centrality in each trigger used to select the events in Pb–Pb collision
1031 is shown in Fig. 25 and the reason why the centrality has step structure is that there are
1032 three different trigger classes classified by the amplitude threshold on VZERO detector.
1033 Because the distribution of events as function of centrality is not a flat, this may lead to
1034 additional bias, in particular when one needs to combine the results from different triggers.

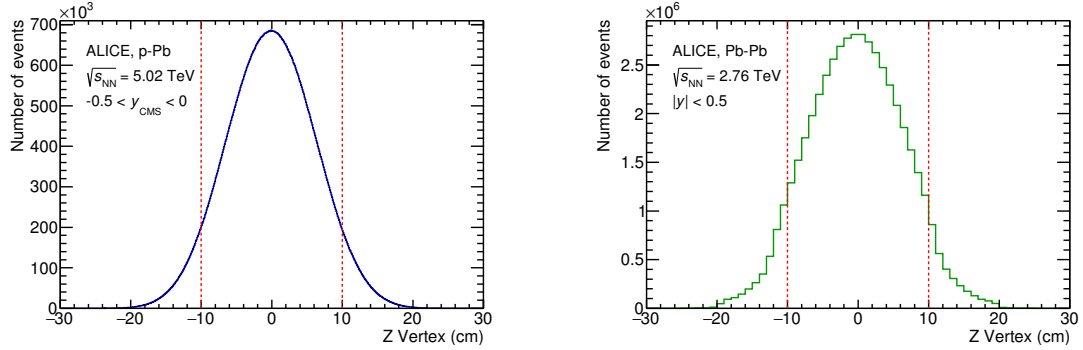


Figure 23: Distribution of vertex-z position from the accepted events in p–Pb collision(Left) and in Pb–Pb collisions(Right). The red dashed line indicates vertex cut

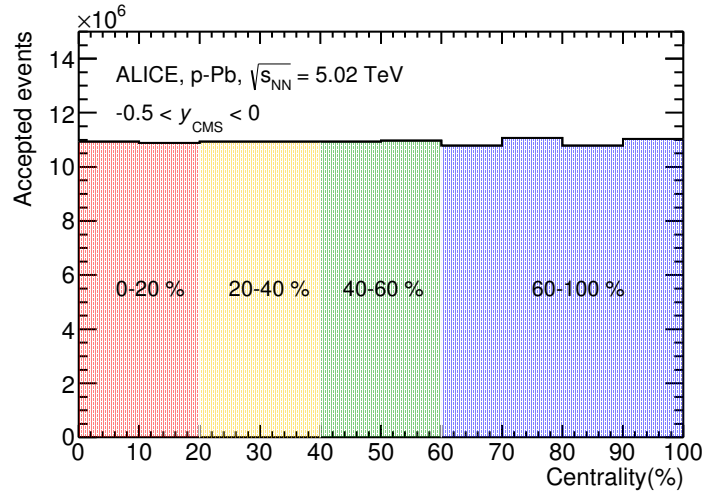


Figure 24: Multiplicity distribution of accepted events in p–Pb collision in percentile. The each color presents the four intervals for the analysis.

1035 For example, events from 40-80% centrality bin have bias with high statistics in 40-60%. In
1036 order to avoid this effect, we have applied a flattening procedure to have flat distribution
1037 of events as function of centrality. A brief explanation of the method is below :

- 1038 1. Histograms are obtained for the effective mass distribution in 1% centrality bins and
1039 for the centrality distribution
- 1040 2. The effective mass distributions are scaled in each 1% centrality bin by a factor:
1041 Factor = $N_{\text{event}} \text{ in 20-40\%} / 20 / N_{\text{event}} \text{ in current 1\% bin}$
- 1042 3. Each bin in the centrality distribution is scaled using the factor described above
- 1043 4. Histograms are added for centrality bins of interest: 0-10%, 10-40%, 40-80%, 0-80%

1044 The resulting number of events in each centrality classes is summarized in Table 8.

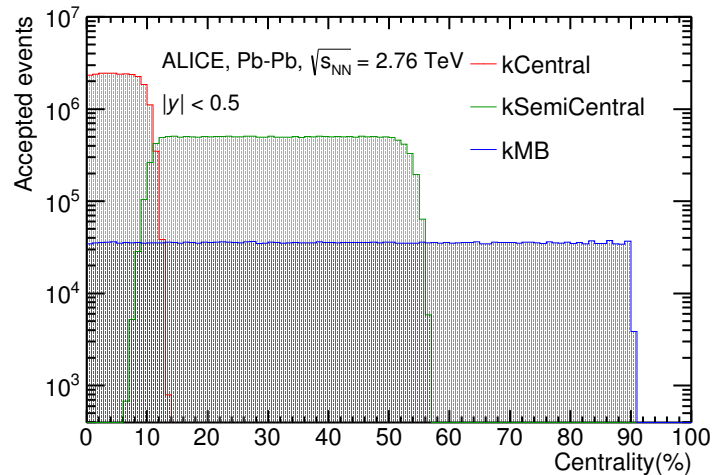


Figure 25: Centrality distribution of three different trigger classes.

Collision	Centrality	Number of events
p-Pb	0-20%	21.82×10^6
	20-40%	21.86×10^6
	40-60%	21.91×10^6
	60-100%	43.68×10^6
Pb-Pb	0-10%	5.58×10^6
	10-40%	16.73×10^6
	40-80%	22.31×10^6

Table 8: Number of analyzed events per multiplicity/centrality interval

1045 **5.1.2 Track and topological selection**

1046 In comparison with the Ξ^{*0} analysis carried out in pp collisions at $\sqrt{s} = 7$ TeV [8], track
 1047 and topological selections were revised and adapted to the p-Pb dataset. Pions from strong
 1048 decays of Ξ^{*0} were selected according to the criteria for primary tracks. As summarized in
 1049 Table 9, all charged tracks were selected with $p_T > 0.15$ GeV/c and $|\eta_{\text{lab}}| < 0.8$, as described
 1050 in Ref. [26]. The primary tracks were chosen with the Distance of Closest Approach (DCA)
 1051 to PV of less than 2 cm along the longitudinal direction (DCA_z) and lower than $7\sigma_r$ in
 1052 the transverse plane (DCA_r), where σ_r is the resolution of DCA_r . The σ_r is strongly
 1053 p_T -dependent and lower than $100 \mu\text{m}$ for $p_T > 0.5$ GeV/c [26]. To ensure a good track
 1054 reconstruction quality, candidate tracks were required to have at least one hit in one of the
 1055 two innermost layers (SPD) of the ITS and to have at least 70 reconstructed points in the
 1056 Time Projection Chamber (TPC), out of a maximum of 159. The Particle IDentification
 1057 (PID) criteria for all decay daughters are based on the requirement that the specific energy
 1058 loss (dE/dx) is measured in the TPC within three standard deviations (σ_{TPC}) from the
 expected value (dE/dx_{exp}), computed using a Bethe-Bloch parametrization [26].

Common track selections	$ \eta_{\text{lab}} $	< 0.8
	p_T	> 0.15 GeV/c
	PID $ (dE/dx) - (dE/dx)_{\text{exp}} $	$< 3 \sigma_{\text{TPC}}$
Primary track selections	DCA_z to PV	< 2 cm
	DCA_r to PV	$< 7\sigma_r$ - $10\sigma_r$ (p_T)
	number of SPD points	≥ 1
	number of TPC points	> 70
	χ^2 per cluster	< 4

Table 9: Track selections common to all decay daughters and primary track selections
 applied to the charged pions from decays of Ξ^{*0} .

1059

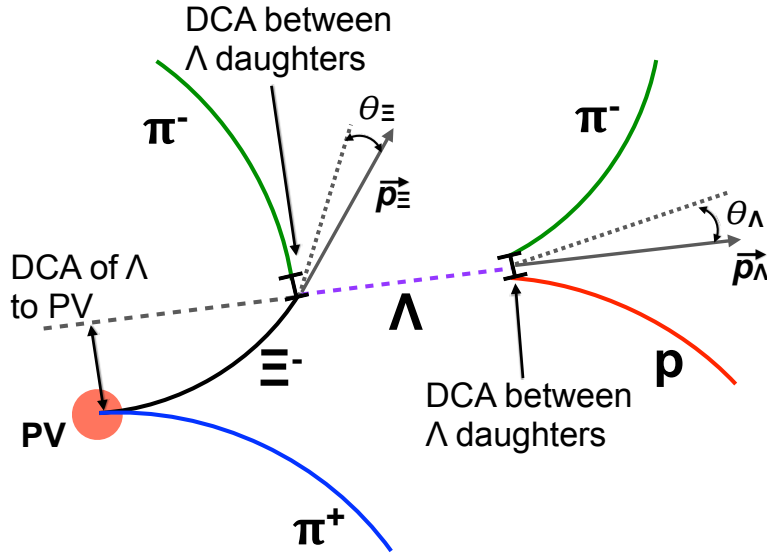


Figure 26: Sketch of the decay modes for Ξ^{*0} and depiction of the track and topological selection criteria.

1060 Since pions and protons from weak decay of Λ ($c\tau = 7.89$ cm [1]) and pions from weak
 1061 decay of Ξ^- ($c\tau = 4.91$ cm [1]) are produced away from the PV, specific topological and
 1062 track selection criteria, as summarized in Table 10, were applied [7, 8, 47].

Topological cuts	p-Pb	Pb-Pb
DCA _r of Λ decay products to PV	> 0.06 cm	> 0.11 cm
DCA between Λ decay products	< 1.4 cm	< 0.95 cm
DCA of Λ to PV	> 0.015 cm	> 0.06
$\cos\theta_\Lambda$	> 0.875	> 0.998
$r(\Lambda)$	$0.2 < r(\Lambda) < 100$ cm	$0.2 < r(\Lambda) < 100$ cm
$ M_{p\pi} - m_\Lambda $	< 7 MeV/ c^2	< 7 MeV/ c^2
DCA _r of pion (from Ξ^-) to PV	> 0.015 cm	> 0.035 cm
DCA between Ξ^- decay products	< 1.9 cm	< 0.275
$\cos\theta_\Xi$	> 0.981	> 0.9992
$r(\Xi^-)$	$0.2 < r(\Xi^-) < 100$ cm	$0.2 < r(\Xi^-) < 100$ cm
$ M_{\Lambda\pi} - m_\Xi $	< 7 MeV/ c^2	< 7 MeV/ c^2

Table 10: Topological and track selection criteria.

1063 In the analysis of Ξ^{*0} , Λ and π from Ξ^- were selected with a DCA of less than 1.9 cm
1064 and with a DCA_r to the PV greater than 0.015 cm. The Λ daughter particles (π and p)
1065 needs to have a DCA_r to the PV greater than 0.06 cm, while the DCA between the two
1066 particles was required to be less than 1.4 cm. The cosine of the pointing angle (θ_Λ , θ_Ξ)
1067 and the radius of the fiducial volume ($r(\Lambda)$, $r(\Xi)$) in Table 10 were applied to optimize the
1068 balance of purity and efficiency of each particle sample.

1069 **5.1.3 Particle identification**

1070 PID selection criteria are applied for

- 1071 1. π^\pm (last emitted π) and proton from Λ
 1072 2. π^\pm (second emitted π) from Ξ^\pm
 1073 3. π^\pm (first emitted π) from $\Xi(1530)^0$

1074 by using TPC. On TPC dE/dx versus momentum distribution, 3σ cuts are applied to TPC
 1075 for selecting each of the particles. The TPC dE/dx selection allows to have better signal
 1076 with $\sim 20\%$ increase of significance.

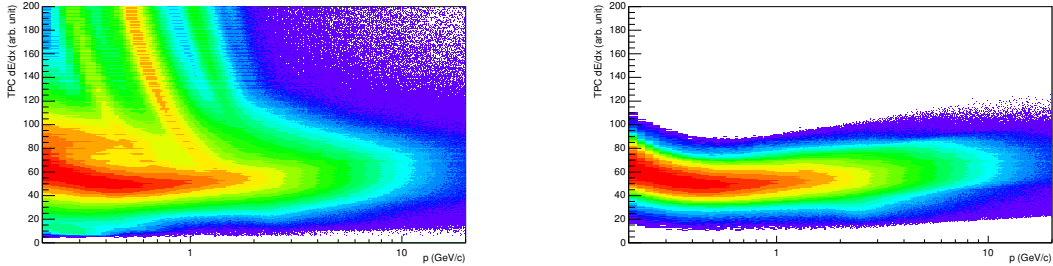


Figure 27: TPC dE/dx as function of transverse momentum in p–Pb collisions for total (Left) and selected first emitted π in 3σ (Right)

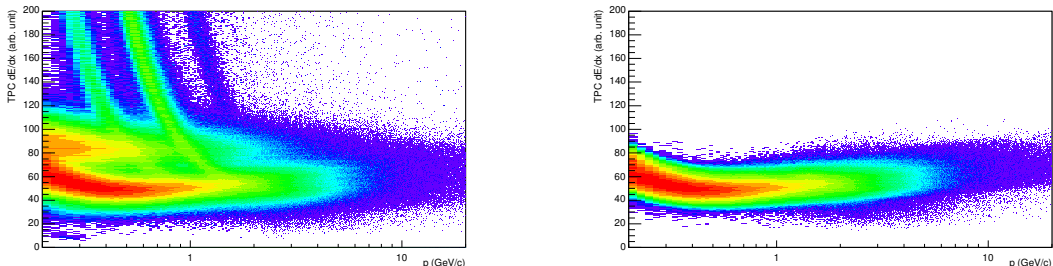


Figure 28: TPC dE/dx as function of transverse momentum in p–Pb collisions for total (Left) and selected second emitted π in 3σ (bottom)

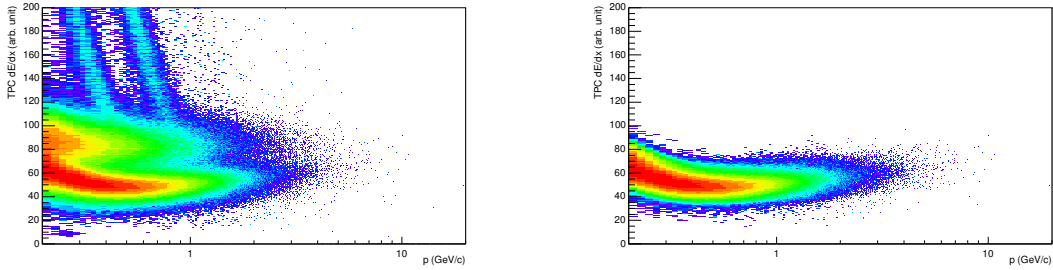


Figure 29: TPC dE/dx as function of transverse momentum in p –Pb collisions for total (Left) and selected last emitted π in 3σ (bottom)

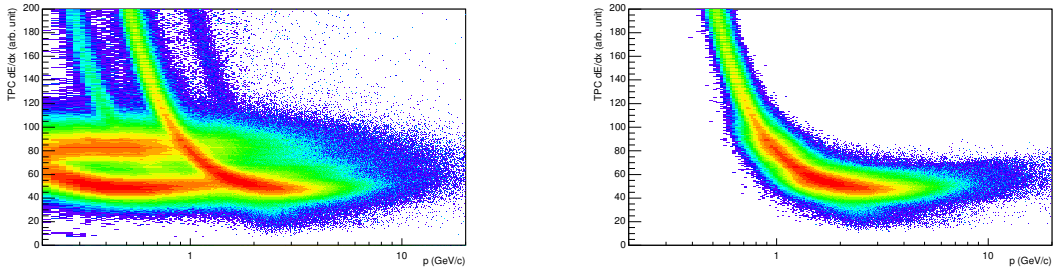


Figure 30: TPC dE/dx as function of transverse momentum in p –Pb collisions for total (Left) and selected proton in 3σ (bottom)

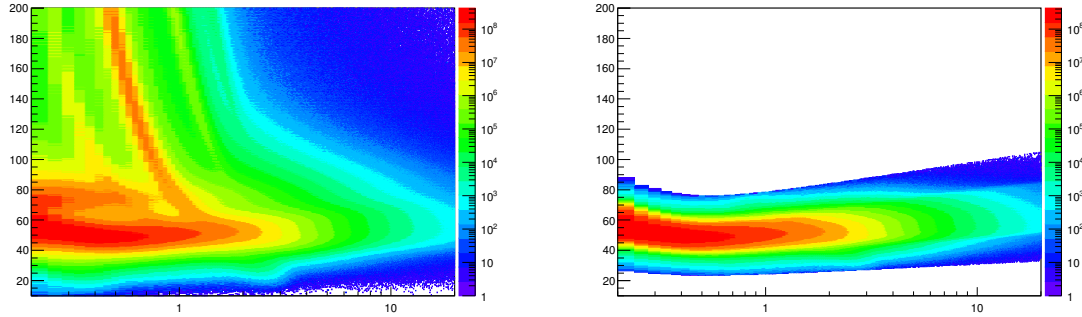


Figure 31: TPC dE/dx as function of transverse momentum in Pb–Pb collisions for total (Left) and selected first emitted π in 3σ (Right)

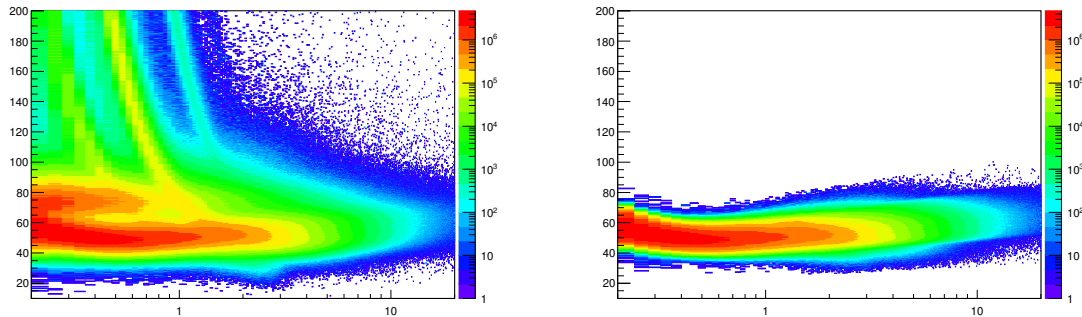


Figure 32: TPC dE/dx as function of transverse momentum in Pb–Pb collisions for total (Left) and selected second emitted π in 3σ (Right)

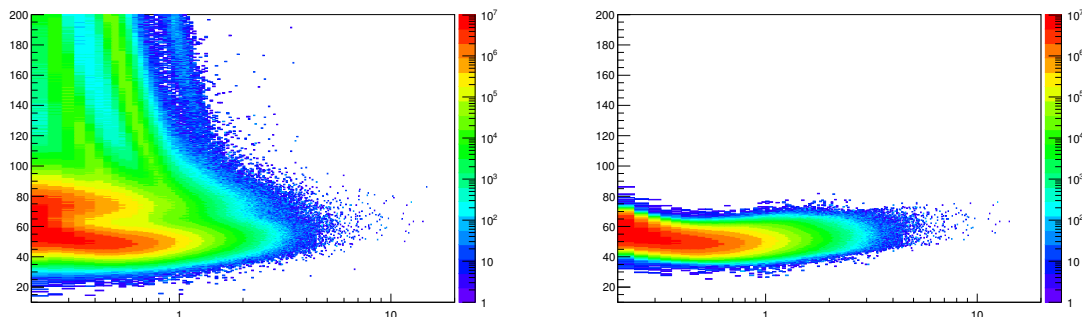


Figure 33: TPC dE/dx as function of transverse momentum in Pb–Pb collisions for total (Left) and selected last emitted π in 3σ (Right)

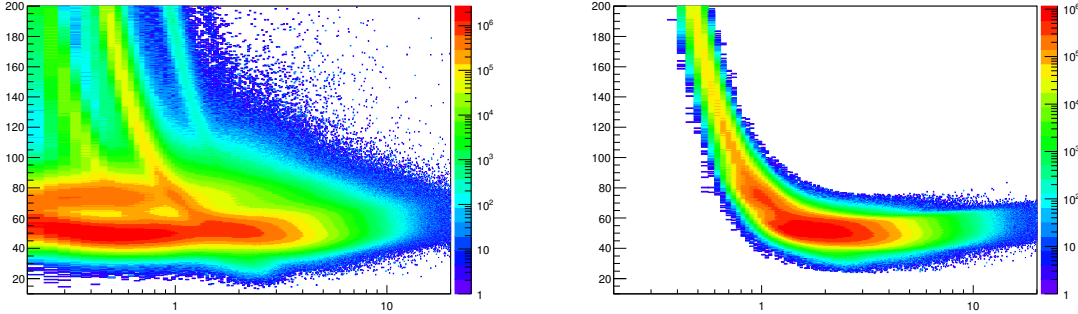


Figure 34: TPC dE/dx as function of transverse momentum in Pb–Pb collisions for total (Left) and selected proton in 3σ (Right)

1077 **5.1.4 Signal extraction**

1078 The Ξ^{*0} signals were reconstructed by invariant-mass analysis of candidates for the decay
 1079 products in each transverse momentum interval of the resonance particle, and for each
 1080 multiplicity class. The $\Xi^-\pi^+(\Xi^+\pi^-)$ invariant mass distribution is reported in Figure 5.1.4
 1081 for semi-central events (20–40%) in p–Pb collisions and Figure 5.1.4 for central events(0–
 1082 10%) in Pb–Pb collisions.

1083 Since the resonance decay products come from location which is indistinguishable from
 1084 the PV, a significant combinatorial background is present. In order to extract $\Xi(1530)^0$
 1085 signal, it is necessary to reduce the combinatorial background as much as possible. For the
 1086 $\Xi(1530)^0$ analysis, event mixing (EM) technique has been applied, by combining uncor-
 1087 related decay products 20 different events in p–Pb (5 different events in Pb–Pb).

1088 The events for the mixing have been chosen by applying the similar selection to minimize
 1089 distortions due to different acceptances and to ensure a similar event structure, only tracks
 1090 from events with similar vertex positions z ($|\Delta z| < 1$ cm) and track multiplicities n ($|\Delta n| <$
 1091 10) were taken.

1092 The mixed-event background distributions were normalised to two fixed regions,
 1093 $1.49 < M_{\Xi\pi} < 1.51$ GeV/c^2 and $1.56 < M_{\Xi\pi} < 1.58$ GeV/c^2 , around the Ξ^{*0} mass
 1094 peak (Figure 5.1.4 and 5.1.4). These regions were used for all p_T intervals and multiplicity
 1095 classes, because the background shape is reasonably well reproduced in these regions and
 1096 the invariant-mass resolution of the reconstructed peaks appears stable, independently of
 1097 p_T . The uncertainty on the normalization was estimated by varying the normalization
 1098 regions and is included into the systematic uncertainty due to the signal extraction (Sec-
 1099 tion 5.4).

1100 After the background subtraction, the resulting distribution is shown in Figure 5.1.4
 1101 and 5.1.4. In order to obtain raw yields, a combined fit of a first-order polynomial for

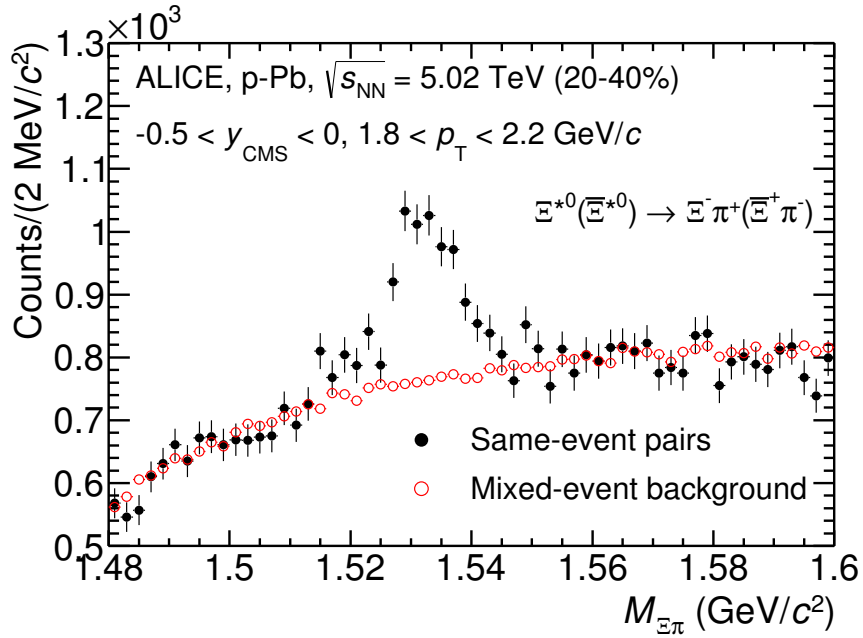


Figure 35: The $\Xi^\pm\pi^\pm$ invariant mass distribution (Same-event pairs) in $1.8 < p_T < 2.2$ GeV/c and for the multiplicity class 20-40%. The background shape, using pairs from different events (Mixed-event background), is normalised to the counts in $1.49 < M_{\Xi\pi} < 1.51$ GeV/c 2 and $1.56 < M_{\Xi\pi} < 1.58$ GeV/c 2 .

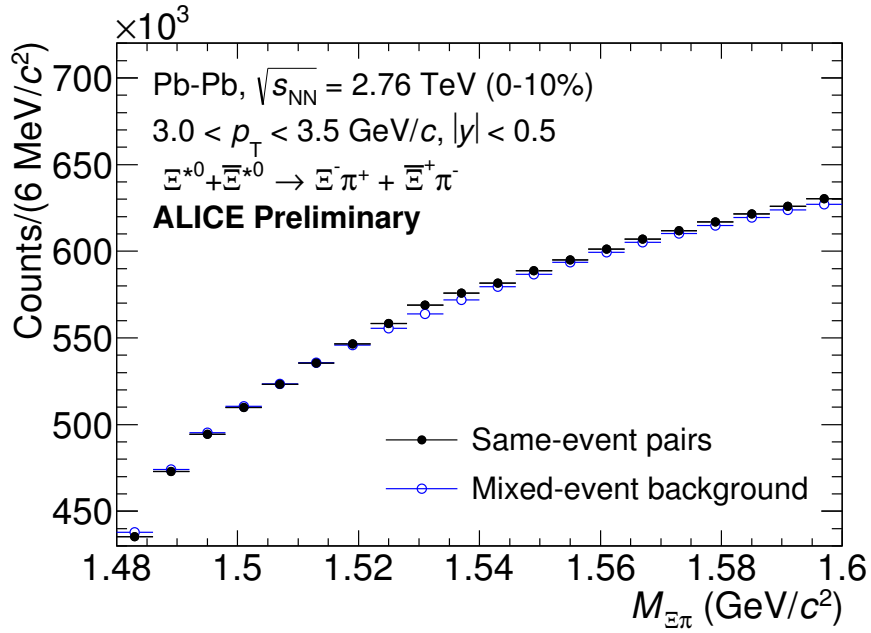


Figure 36: The $\Xi^\pm\pi^\pm$ invariant mass distribution (Same-event pairs) in $3.0 < p_T < 3.5$ GeV/c and for the centrality class 0-10%. The background shape, using pairs from different events (Mixed-event background), is normalised to the counts in $1.49 < M_{\Xi\pi} < 1.51$ GeV/c² and $1.56 < M_{\Xi\pi} < 1.58$ GeV/c².

1102 the residual background and a Voigtian function (a convolution of a Breit-Wigner and a
 1103 Gaussian function accounting for the detector resolution) for the signal was used. The
 1104 mathematical form of fit function used in analysis is:

$$f(M_{\Xi\pi}) = \frac{Y}{2\pi} \frac{\Gamma_0}{(M_{\Xi\pi} - M_0)^2 + \frac{\Gamma_0^2}{4}} \frac{e^{-(M_{\Xi\pi} - M_0)/2\sigma^2}}{\sigma\sqrt{2\pi}} + bg(M_{\Xi\pi}) \quad (7)$$

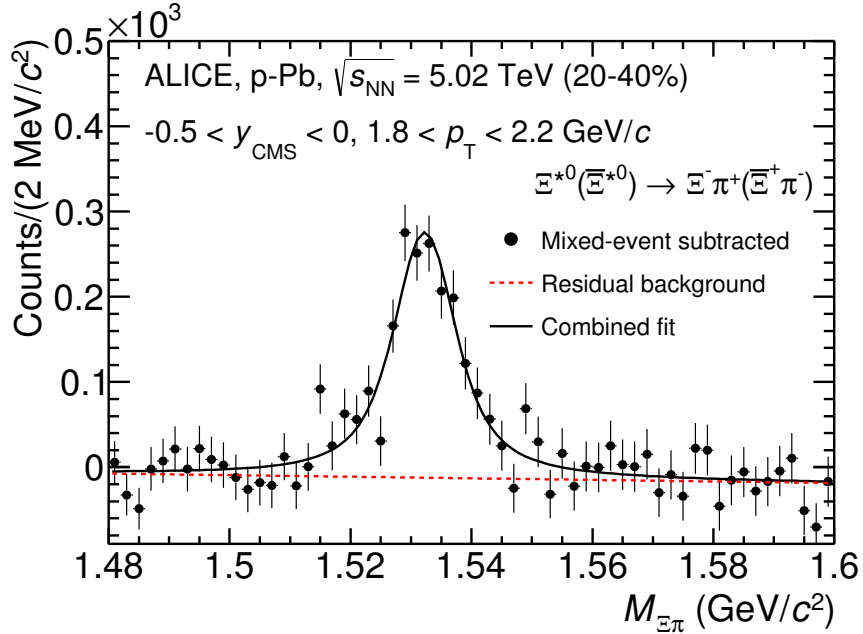


Figure 37: The invariant mass distribution after subtraction of the mixed-event background in p–Pb collisions. The solid curve represents the combined fit, while the dashed line describes the residual background.

1105 The mass parameter of the Voigtian fit (M_0) is left free within the fit range ($1.48 \text{ GeV}/c^2$
 1106 and $1.59 \text{ GeV}/c^2$). The overall invariant mass width of the Voigtian function is governed
 1107 by 2 parameters: σ and Γ_0 . The σ describes the broadening of the peak due to finite
 1108 detector resolution while Γ describes the intrinsic width of the resonance itself. The Γ_0 is
 1109 fixed to the PDG value of $9.1 \text{ MeV}/c$ for the $\Xi(1530)^0$. Because of lack of statistics, the
 1110 σ can be over estimated. Therefore the σ parameter is fixed to value derived from σ in
 1111 MB events which has largest statistics. The σ as function of p_T distribution in MB events
 1112 is shown in Figure. 39 and we also report invariant mass of $\Xi(1530)^0$ as function of p_T in
 1113 Figure. 40. The raw yields of $\Xi(1530)^0$ have been extracted from the Voigtian fit for the 4

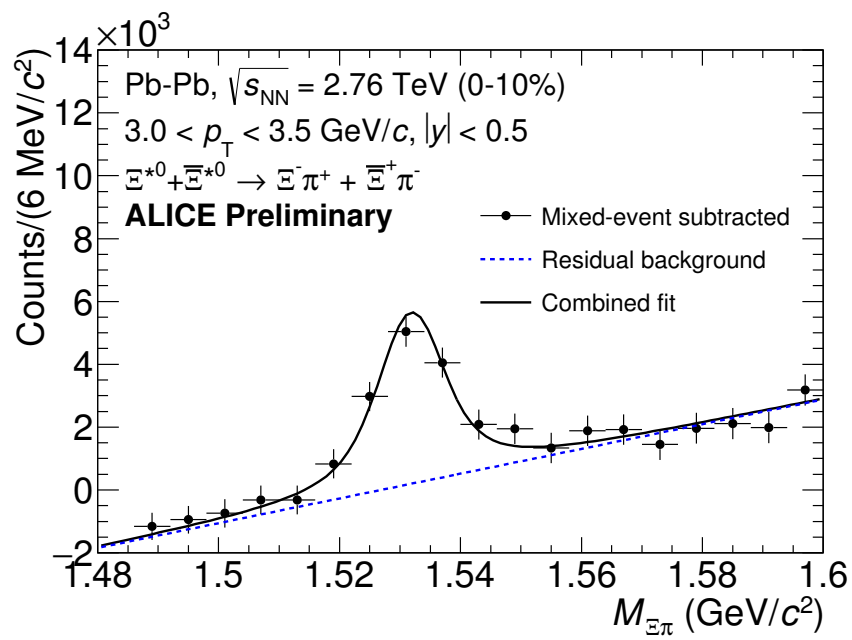


Figure 38: The invariant mass distribution after subtraction of the mixed-event background in Pb–Pb collisions. The solid curve is the combined fit, while the dashed line represents the residual background.

¹¹¹⁴ multiplicity bins (+ NSD events) in p–Pb and 3 centrality bins (+ MB events) in Pb–Pb
¹¹¹⁵ collisions and the yields as function of p_{T} are shown in Figure 41.

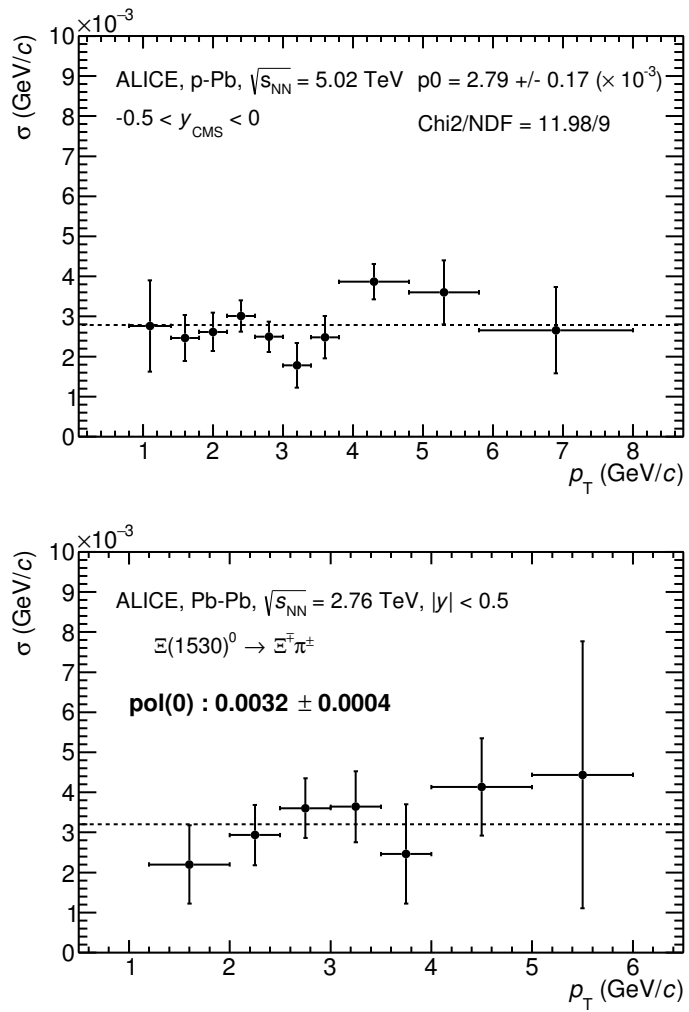


Figure 39: σ fit parameters as a function of p_T in MB in p-Pb collisions (top) and in Pb-Pb collisions (bottom).

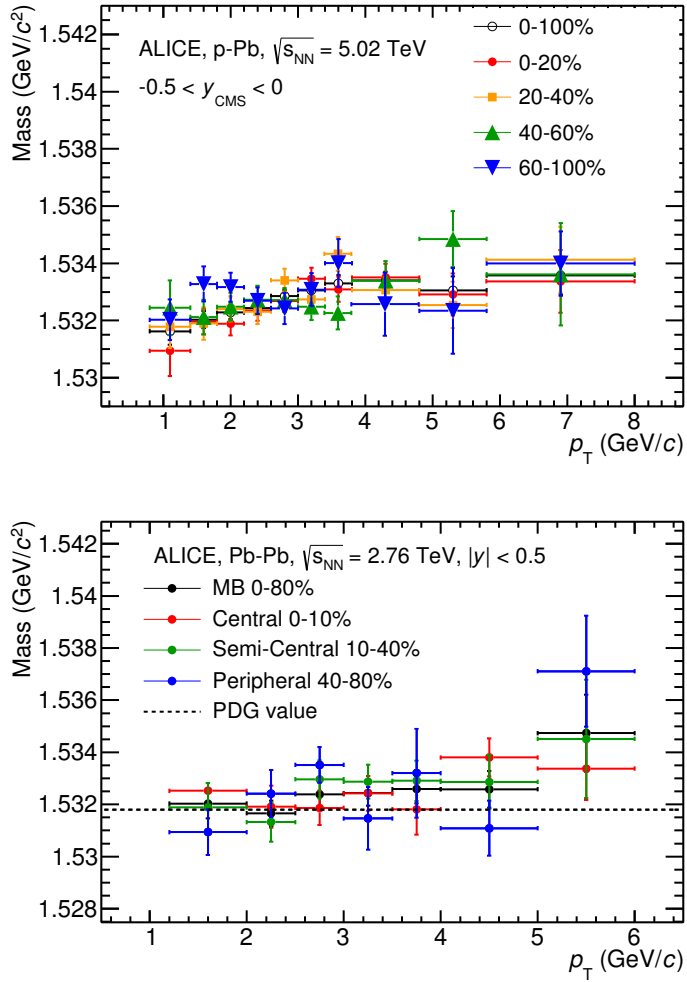


Figure 40: $\Xi(1530)^0$ mass distribution as a function of p_T in each multiplicity classes in p–Pb collisions (top) and the different centrality classes in Pb–Pb (bottom). The mass values are obtained from fit of the Voigtian function.

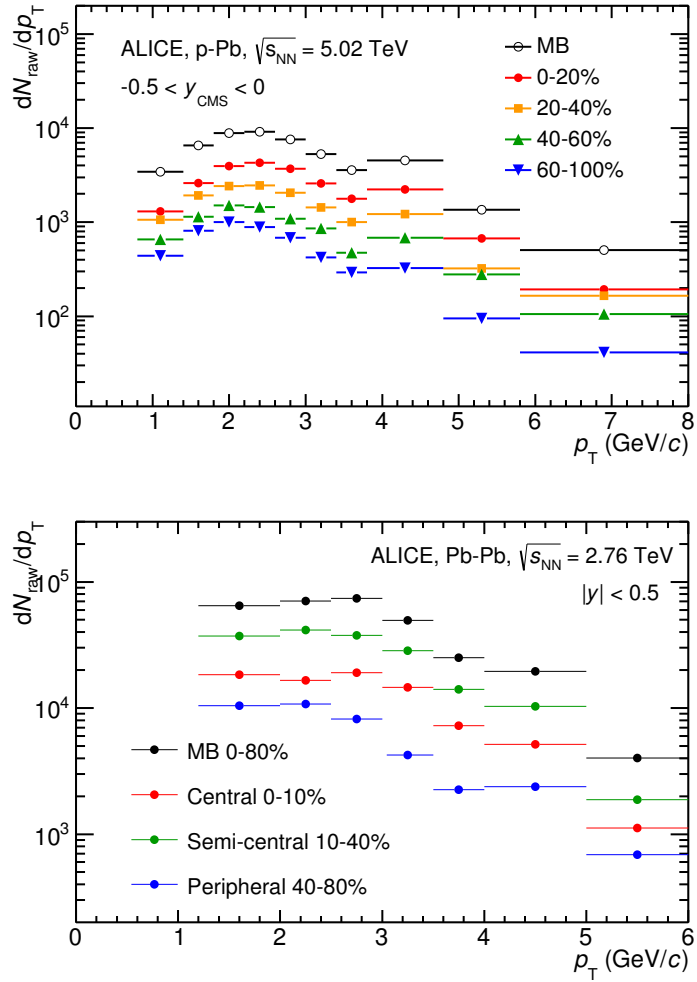


Figure 41: The raw spectra of $\Xi(1530)^0$ obtained by integrating the Voigtian fit function for different multiplicities in p-Pb collisions (top) and Pb-Pb collisions (bottom). Only the statistical error is reported.

1116 **5.2 Efficiency correction**

1117 The raw yields were corrected for the geometrical acceptance and the reconstruction efficiency
 1118 ($A \times \epsilon$) of the detector (Figure. 42). By using the DPMJET 3.05 event generator [48]
 1119 and the GEANT 3.21 package [49], a sample of about 100 million p–Pb events was sim-
 1120 ulated and reconstructed in order to compute the corrections. The distributions of $A \times \epsilon$
 1121 were obtained from the ratio between the number of reconstructed Ξ^{*0} and the number of
 1122 generated particle in the same p_T and rapidity interval. Since the correction factors for
 1123 different multiplicity classes are in agreement with those from MB events within statistical
 1124 uncertainty, the latter were used for all multiplicity classes.

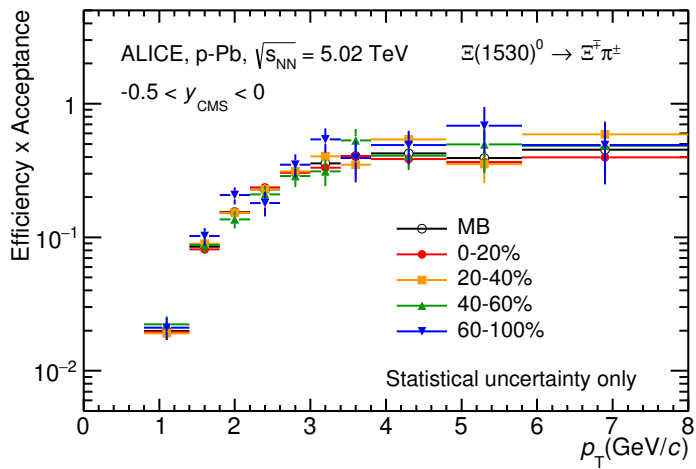


Figure 42: The geometrical acceptance and the reconstruction efficiency ($A \times \epsilon$) for $\Xi(1530)^0$ in $-0.5 < y_{\text{CMS}} < 0$. Only statistical uncertainties are shown.

1125 Because the generated $\Xi(1530)^0$ spectra have different shapes than the measured $\Xi(1530)^0$
 1126 spectra, it is necessary to weight the generated and reconstructed $\Xi(1530)^0$ spectra in these
 1127 simulations. Fig. 43 shows the generated and reconstructed $\Xi(1530)^0$ spectra plotted with
 1128 the (corrected) measured $\Xi(1530)^0$ spectrum for MB events and the Levy fit of that mea-
 1129 sured spectrum. The generated and measured $\Xi(1530)^0$ spectra have different behaviours
 1130 for the range $0.5 < p_T < 1$ GeV/c. The generated $\Xi(1530)^0$ spectrum decreases with
 1131 increasing p_T over this range, while the fit of the measured $\Xi(1530)^0$ spectrum reaches a
 1132 local maximum in this range. The correction ϵ is observed to change rapidly over this
 1133 p_T range. It is therefore necessary to weight the generated spectrum so that it has the
 1134 shape of the measured $\Xi(1530)^0$ spectrum (and to apply corresponding weights to the re-
 1135 constructed $\Xi(1530)^0$ spectrum). An iterative procedure is performed to determine the
 1136 correct weighting (and therefore the correct ϵ).

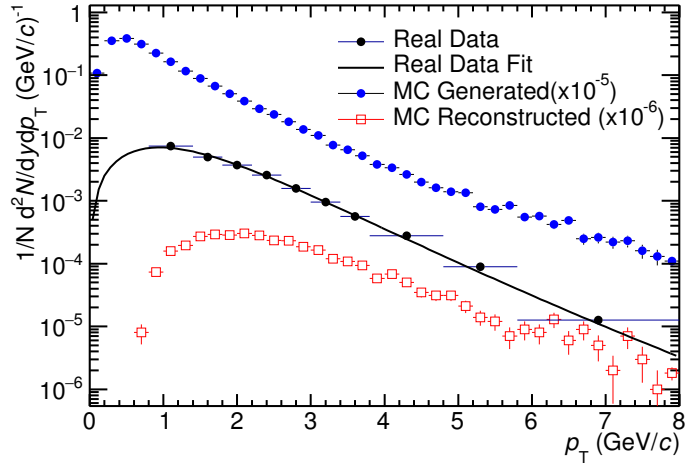


Figure 43: Real corrected $\Xi(1530)^0$ spectrum (black) for the minimum bias with Levy fit (black curve). Also shown are the unweighted generated (blue) and reconstructed (red) $\Xi(1530)^0$ spectra.

- 1137 1. The unweighted ϵ is calculated.
- 1138 2. This ϵ is used to correct the measured xis spectrum.
- 1139 3. The corrected $\Xi(1530)^0$ spectrum is fit.
- 1140 4. This fit is used to weight the simulated xis spectra. A p_T dependent weight is applied
1141 to the generated xis spectrum so that it follows the fit. The same weight is applied
1142 to the reconstructed xis spectrum.
- 1143 5. The (weighted) ϵ is calculated.
- 1144 6. Steps 2-5 are repeated (with the weighted ϵ from step 5 used as the input for step 2)
1145 until the ϵ values are observed to change by $< 0.1\%$ (relative) between iterations. It
1146 is observed that four iterations are sufficient for this procedure to converge.

1147 Finally, the re-weighted efficiency is obtained and the distribution as function of p_T is
1148 shown in Figure 44.

1149 In order to obtain the correction factor dedicated in Pb-Pb collisions, MC events are
1150 generated using Heavy Ion Jet Interaction Generator (HIJING). The generated events are
1151 passed through a GEANT3 model of the ALICE experiment with a realistic description of
1152 the detector response. Because we have observed centrality dependent efficiency, the cen-
1153 trality dependent efficiencies have been applied to get corrected raw yield. The reweighting

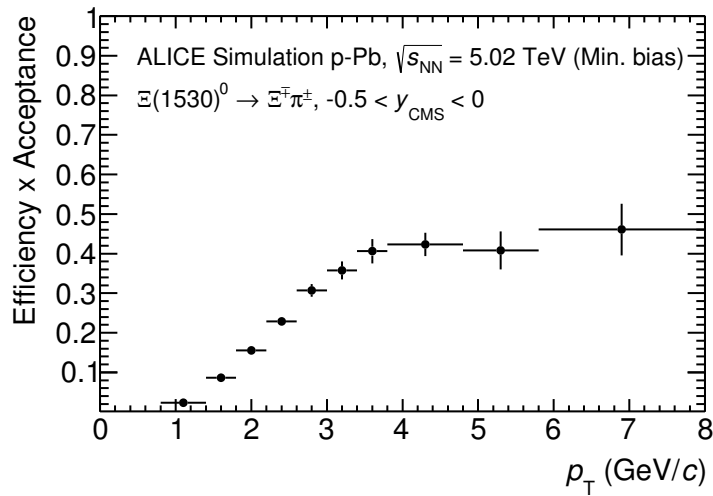


Figure 44: Efficiency as a function of p_T in minimum bias events in p–Pb collisions.

1154 approach which was used to correct the efficiency in p–Pb is also applied to the efficiency
 1155 obtained in Pb–Pb.

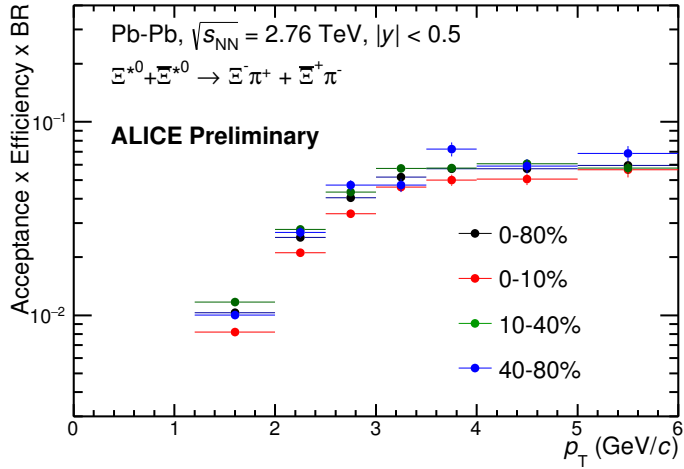


Figure 45: Efficiency as a function of p_T in different centrality classes in Pb–Pb collisions

1156 **5.3 Corrected p_T -spectra**

1157 The p_T spectrum is by the number of produced particles of a given type in the desired
 1158 interval of phase-space divided by the number of inelastic collisions. The spectrum is
 1159 calculated as:

$$\frac{1}{N} \times \frac{d^2N}{dydp_T} = \frac{1}{N_{E,PhysSel}} \times \frac{N_{raw}}{dp_T dy} \frac{1}{\epsilon} \frac{N_{total}^{MC}}{N_{post-PVcut}^{MC}}, \quad (8)$$

1160 where N_E represent the number inelastic collisions, the $\frac{dN}{dydp_T}$ is the yield per range of
 1161 rapidity y , per range in p_T . On the right hand side $N_{E,PhysSel}$ is the number of events
 1162 counted by the physics selection trigger. N_{raw} is the raw extracted number of particle in the
 1163 rapidity and p_T bin of width $\Delta y = 0.5$ in p–Pb ($\Delta y = 1.0$ in Pb–Pb) and Δp_T , respectively.
 1164 ϵ is the reconstruction efficiency estimated from Monte Carlo simulations. $\frac{N_{total}^{MC}}{N_{post-PVcut}^{MC}}$ is the
 1165 ratio of the total number of particle from MC divided by the number of particle from MC
 1166 after the Primary-Vertex cut is imposed. It takes into account the fraction of particle lost
 1167 after imposing the PV cut. We notice that for minimum-bias results in p–Pb, we adopted
 1168 a normalisation such that to provide result from non-single diffractive(NSD) cross-section.
 1169 The normalisation factor is 0.964 [6]. The obtained spectrum at MB and the spectrums
 1170 from different multiplicity classes in p–Pb are shown in Figure 46 and different centrality
 1171 classes in Pb–Pb are shown in Figure 47.

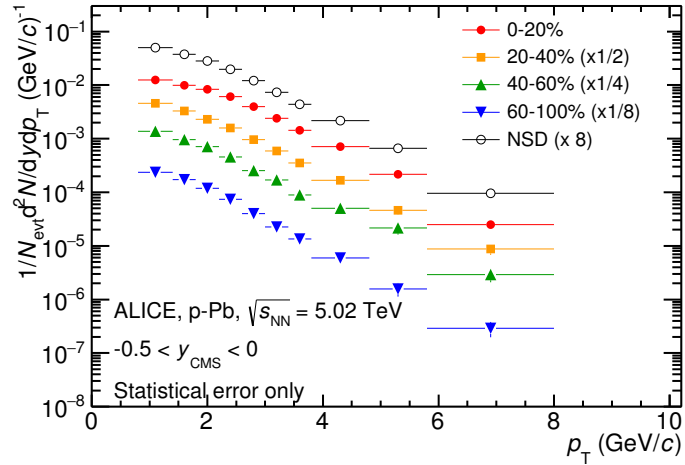


Figure 46: Corrected p_T -spectra of $\Xi(1530)^0$ in NSD and different multiplicity classes in p-Pb collisions.

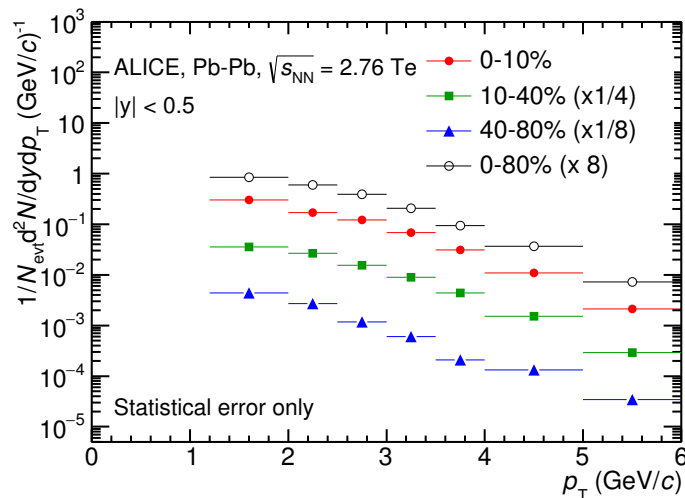


Figure 47: Corrected p_T -spectra of $\Xi(1530)^0$ in different centrality classes in Pb-Pb collisions.

1172 **5.4 Systematic uncertainties**

1173 The systematic uncertainties are calculated in seven principle groups. The procedure to ob-
1174 tain the systematic uncertainties is performed many times by varying the possible permuta-
1175 tion of the analysis parameter. The general strategy for evaluating systematic uncertainties
1176 is described as following:

- 1177 1. Choose one set of parameters for the analysis as default
1178 2. Observe the deviation of yield when one parameter is changed
1179 3. The systematic uncertainty is calculated for a given source as the RMS deviation of
1180 the available sources.
1181 4. The total systematic uncertainty, taking into account all the different sources, is the
1182 sum in quadrature of each source.

1183 To study the systematic effect we repeat the measurement by varying one parameter at
1184 a time. A Barlow [50] check has been performed for each measurement to verify whether it
1185 is due to a systematic effect or a statistical fluctuation. Let each measurement be indicated
1186 by $(y_i \pm \sigma_i)$ and the central value (default measurement) by $(y_c \pm \sigma_c)$, one can define $\Delta\sigma_i$
1187 (Eq. 9).

$$\Delta\sigma_i = \sqrt{(\sigma_i^2 - \sigma_c^2)} \quad (9)$$

1188 Then we calculate $n_i = \Delta y_i / \Delta\sigma_i$, where $\Delta y_i = |y_c - y_i|$. If $n_i \leq 1.0$ then the effects
1189 are due to the statistical fluctuation and if $n_i > 1.0$ we apply consistency check. Since
1190 the alternate and default measurements are not statistically independent, an alternate
1191 measurement which is statistically consistent with the default measurement should not be
1192 used in calculating a systematic uncertainty. The difference between the two measurements
1193 is $\Delta = y_c - y_i$. The difference in quadrature of the uncertainties is calculated by Eq. 9. It
1194 could be possible to check if $\Delta < \sigma$ and exclude such cases from the systematic uncertainties.
1195 However, there can be statistical fluctuations for which $\Delta > \sigma$. If the variations between the
1196 default and alternate measurements are purely statistical, the distribution of Δ/σ should
1197 be a Gaussian with a mean value that is consistent with zero and a deviation σ consistent
1198 with unity. In this analysis, if the mean value is less than 0.1 and σ is less than 1, the
1199 variation passes the consistency check.

1200 Only the measurements which passed the Barlow check ($n_i > 1$) are used to determine
1201 the systematic uncertainty. For measurements $N > 2$, the systematic uncertainty has been
1202 determined as the RMS (eqn. 10) of the available measurements. If $N=2$, the absolute
1203 difference is assigned as systematic uncertainty.

$$\delta y_{syst.} = \sqrt{\frac{1}{N} \sum_i (y_i - \bar{y})^2} \quad (10)$$

1204 Here N is the total number of available measurements including y_c and \bar{y} is the average
1205 of value of the measurements. The measurement did not pass Barlow check, zero systematic
1206 uncertainty has been assigned to the value.

1207 By suing the way as explained above, all the main contributions to the systematic un-
1208 certainty of particle spectra have been studied. In particular those that comes from signal
1209 extraction, topological and kinematical selection cuts, track quality selection and $n\sigma$ TPC
1210 PID variation. the meaning of each source of systematic uncertainty studied is described
1211 in the following:

1212

1213 **Signal extraction**

1214 We have extracted the signal with varying the yield calculating method which contains
1215 the method of signal extraction by integrating the Voigtian fit function and bin counting.
1216 We also have varied the normalisation range which is related to the invariant mass region
1217 where the mixed events distribution is scaled to subtract the combinatorial background
1218 and different background estimator such as Like-Sign distribution and polynomial fit was
1219 taken account into the systematic source of signal extraction. The systematic uncertainty
1220 from signal extraction is sum in quadrature of three sources.

1221

1222 **Topological selection**

1223 To evaluate the stability of the chosen set of values for the topological cuts, loose and tight
1224 cuts have beed defined in order to vary by $\pm 10\%$ respectively. The parameters are changed
1225 once at a time. Total systematic uncertainty from topological selection is calculated by
1226 summation in quadrature of nine sources.

1227

1228 **TPC $N_{cluster}$ selection**

1229 The selection performed for the daughter tracks of the cascade is that $N_{cluster}$ is larger
1230 than 70 and the value has been varied to 60 and 80 in order to estimate the systematic
1231 uncertainty due to this selection.

1232

1233 **TPC dE/dx selection**

1234 In order to evaluate any potential effect due to the TPC dE/dx selection (U_{PID}), the N_σ
1235 selection was varied with $N = 2.5$ and 3.5 .

1236

1237 **p_T shape correction**

1238 As described in Section 5.2, due to the different shape of the measured and generated
1239 $\Xi(1530)^0$ spectra, we have applied reweighing procedure to the generated spectra to have
1240 same shape and this correction is added into contributor of systematic uncertainty as
1241 p_T shape correction.

1242

1243 **Mass window range selection**

1244 In order to select Ξ^\pm which is daughter particle of $\Xi(1530)^0$, we apply the mass window

1245 ± 7 MeV/c² around $\Xi(1530)^0$ mass on $\Lambda\pi$ invariant mass distribution. The boundaries has
1246 been varied to ± 6 MeV/c² and ± 8 MeV/c² to estimate systematic uncertainty.

1247

1248 **Vertex range selection**

1249 The distribution of vertex-z is shown in Fig.23. The cut on |Vz| was varied from the nom-
1250 inal ± 10 cm to ± 9 cm, ± 11 cm.

1251

1252 **Material Budget and hadronic cross section**

1253 A possible source of uncertainty comes from the description of the material, active (de-
1254 tecting area) or dead (structure and cable), that the particles cross during their travel in
1255 the MC with respect to the real material present in the detector. Such description could
1256 affect the reconstruction efficiency in different aspects (e.g. multiple scattering, energy
1257 loss). The value estimated by Ξ analysis [24] has been used in this study which gives 4%
1258 systematic uncertainty. In case of systematic uncertainty from hadronic cross section, we
1259 have inherited the value studied in previous measurement[51] which amount is 1%.

1260

1261 **Tracking efficiency**

1262 Systematic uncertainties from tracking efficiency from ITS + TPC combined track were
1263 assigned as 3% in p–Pb and 4% in Pb–Pb collision system.[51]
1264 (<https://twiki.cern.ch/twiki/bin/view/ALICE/TrackingEfficiencyCharged>)

1265

1266 Finally, total systematic uncertainty is sum in quadrature of sources listed above. Fig-
1267 ure 48 and Figure 49 show the total systematic uncertainty in minimum bias event and
1268 different multiplicity classes in p–Pb collisions, respectively. Again, Figure 50 and Figure
1269 51 present the total systematic uncertainty in minimum bias event and different centrality
1270 classes in Pb–Pb collisions.

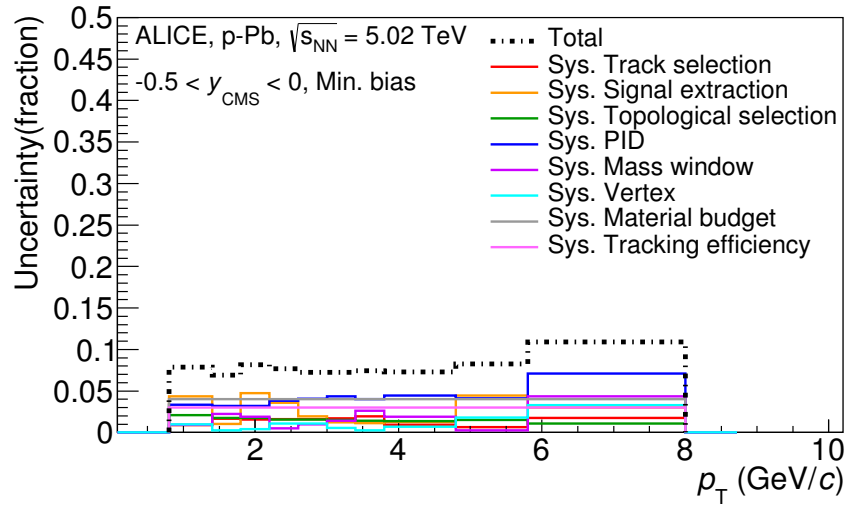


Figure 48: Summary of the contributions to the systematic uncertainty in minimum bias events in p–Pb collisions. The dashed black line is the sum in quadrature of all the contributions.

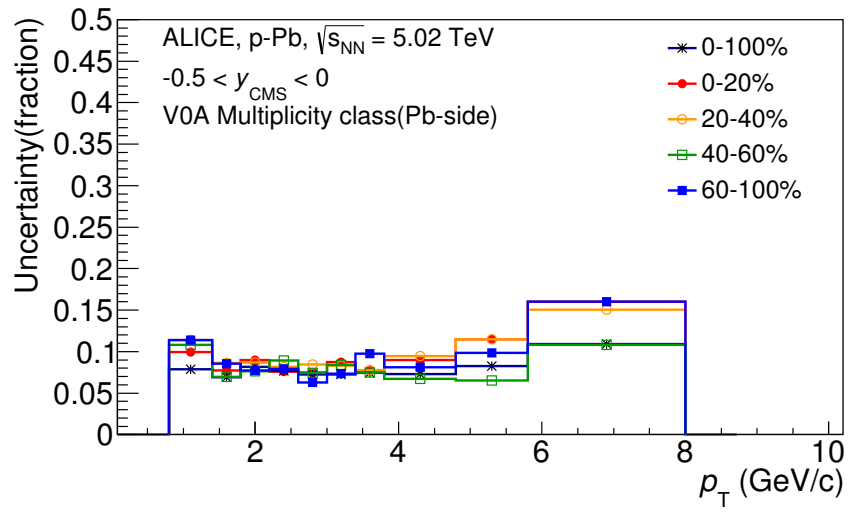


Figure 49: Systematic uncertainties for each multiplicity classes in p–Pb collisions.

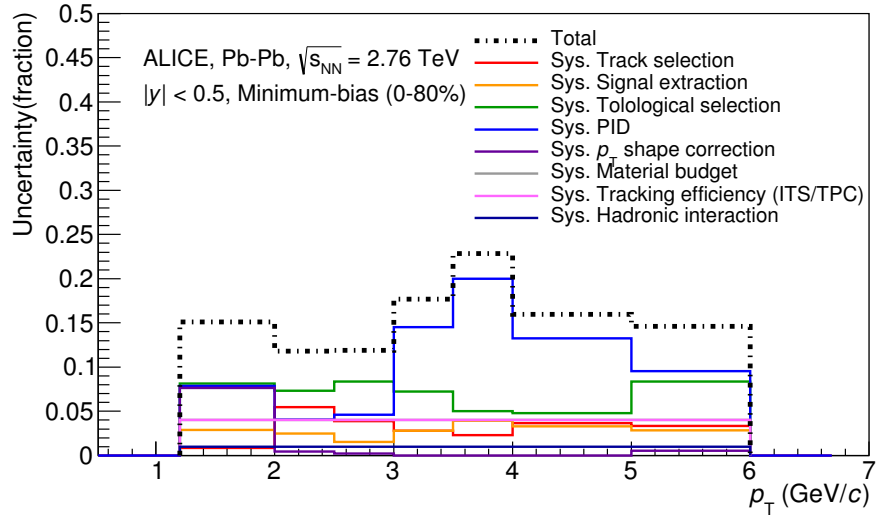


Figure 50: Summary of the contributions to the systematic uncertainty in minimum bias events in Pb–Pb collisions. The dashed black line is the sum in quadrature of all the contributions.

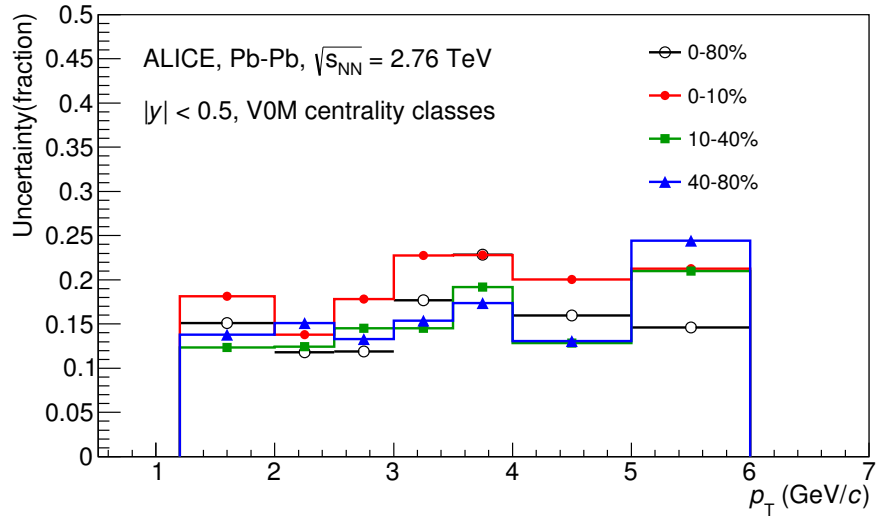


Figure 51: Systematic uncertainties for each multiplicity classes.

Source of uncertainty	p-Pb	Pb-Pb
<i>p</i> _T -dependent		
Tracking efficiency	3%	4%
Tracks selection	1-2%	1-5%
Topological selection	1-2%	5-8%
PID	3-7%	4-20%
Signal extraction	1-5%	1-4%
<i>p</i> _T shape correction	-	0-8%
Mass window (Ξ^\pm)	4%	-
Vertex selection	3%	-
<i>p</i> _T -independent		
Hadronic interaction	-	1%
Material budget	4%	4%
Branching ratio	0.3%	0.3%
Total	8-12%	9-25 %

Table 11: Summary of the systematic uncertainties on the differential yield, $d^2N/(dp_T dy)$. Minimum and maximum values in all p_T intervals and multiplicity classes in p–Pb, centrality classes in Pb–Pb are shown for each source.

1271 **5.5 $\Xi(1530)^0$ transverse momentum spectra**

1272 The raw yield shown in Figure 46 and 47 have been corrected for efficiency as described
 1273 in section 5.2. The measured spectra for $(\Xi(1530)^0 + \bar{\Xi}(1530)^0)/2$ are reported in Figure
 1274 52 for p–Pb collisions and Figure 53 for Pb–Pb collisions. The statistical and systematic
 1275 uncertainties are reported respectively as the error bars and the boxes on the plot. The
 1276 corrected yields for p–Pb collisions are measured with $0.8 < p_T < 8.0$ GeV/c while the
 1277 yields for Pb–Pb collisions are obtained with $1.2 < p_T < 6.0$ GeV/c due to difficulty of
 1278 signal extraction in low and high p_T region.

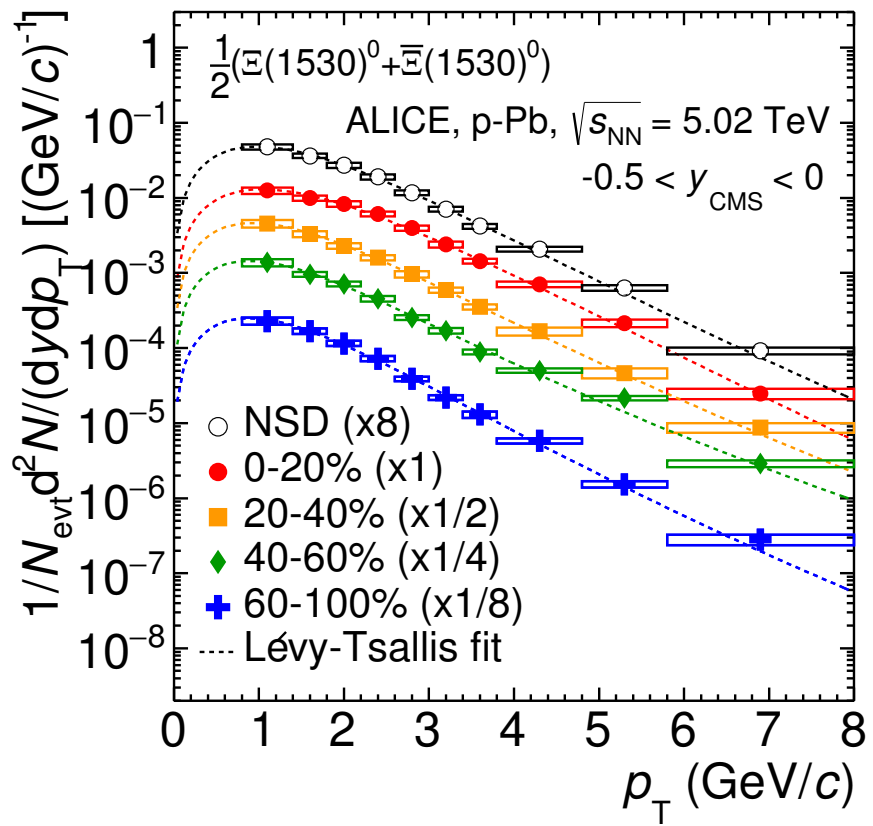


Figure 52: Corrected yields as function of p_T in NSD events and multiplicity dependent event classes in p-Pb collision system. Statistical uncertainties are presented as bar and systematical uncertainties are plotted as boxes.

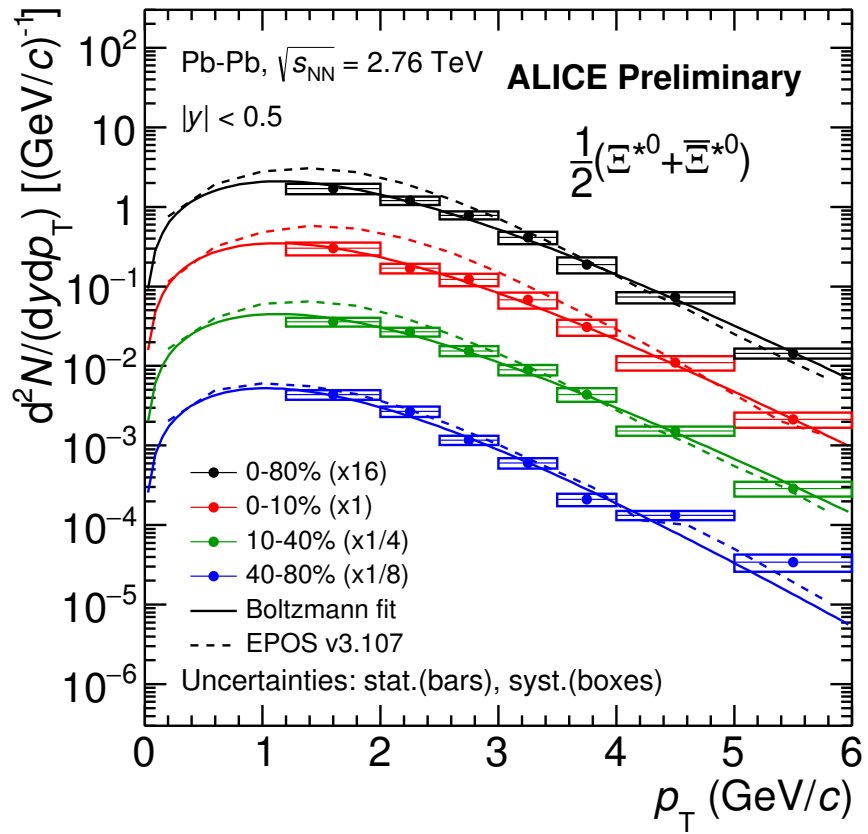


Figure 53: Corrected yields as function of p_T in different centrality classes in Pb–Pb collision system. Statistical uncertainties are presented as bar and systematical uncertainties are plotted as boxes.

1279 **6 Further results and discussion**

1280 The transverse momentum distributions of double-strange hyperon resonances, $\Xi(1530)^0$
1281 , produced in p–Pb collisions at $\sqrt{s_{\text{NN}}}= 5.02$ TeV and Pb–Pb collisions at $\sqrt{s_{\text{NN}}}= 2.76$
1282 TeV were measured in the mid-rapidity range and they have been already presented in
1283 Chapter 5. From the measurement, the $\langle p_{\text{T}} \rangle$ and integrated particle yield ratios with
1284 system size have been obtained. In the present Chapter these results are compared with
1285 model predictions and discussed in connection with the following topics:

- 1286
 - Mean transverse momentum studies
 - Study of particle production mechanism in hadronic phase
 - Study of strangeness enhancement

1289 Most of the theoretical aspects related to these topics and, in particular, the description
1290 of the models already have been addressed in Chapter 2.

1291 **6.1 Mean transverse momentum**

1292 Figure 54 shows the mean transverse momentum $\langle p_{\text{T}} \rangle$ as a function of mean charged-
1293 particle multiplicity density $\langle dN_{\text{ch}}/d\eta_{\text{lab}} \rangle$ at midrapidity. The results for $\Xi(1530)^0$ are
1294 compared with those for other hyperons observed in p–Pb collisions at $\sqrt{s_{\text{NN}}}= 5.02$ TeV [5,
1295 7].

1296 Increasing trends from low to high multiplicities are observed for all hyperons. The
1297 mean transverse momenta increase by 20% as the mean charged-particle multiplicity in-
1298 creases from 7.1 to 35.6. This result is similar to the one obtained for the other hyperons.
1299 Furthermore, a similar increase has been observed also for K^{\pm} , K_S^0 , $K^*(892)^0$ and ϕ [6],
1300 whereas protons are subject to a larger ($\sim 33\%$) increase in the given multiplicity range,
1301 as discussed also in Ref. [5].

1302 In all multiplicity classes, the $\langle p_{\text{T}} \rangle$ follows an approximate mass ordering:

- 1303
 - $\langle p_{\text{T}} \rangle_{\Lambda} < \langle p_{\text{T}} \rangle_{\Xi^-} \simeq \langle p_{\text{T}} \rangle_{\Sigma^{*\pm}} < \langle p_{\text{T}} \rangle_{\Xi^{*0}} < \langle p_{\text{T}} \rangle_{\Omega^-}$

1304 The $\langle p_{\text{T}} \rangle$ of $\Sigma^{*\pm}$ looks systematically lower than the $\langle p_{\text{T}} \rangle$ of Ξ^- , despite the larger mass
1305 of $\Sigma^{*\pm}$. The uncertainties, however, are too large to draw any conclusion on possible hints
1306 of violation of the mass hierarchy. This hierarchy of mass-ordering, also including D^0 and
1307 J/ψ in the comparison, is displayed in Figure 55. Note, however, that the D^0 and J/ψ
1308 were measured in different rapidity ranges: $|y_{\text{CMS}}| < 0.5$ [9] ($|y_{\text{CMS}}| < 0.9$ [10]) for D^0
1309 (J/ψ) in pp and $-0.96 < y_{\text{CMS}} < 0.04$ [9] ($-1.37 < y_{\text{CMS}} < 0.43$ [11]) for D^0 (J/ψ) in
1310 p–Pb, and the results for D^0 and J/ψ in p–Pb collisions are for the 0–100% multiplicity
1311 class. This mass dependence is observed in both p–Pb and pp collisions. It was observed
1312 also by the STAR collaboration [52] in MB pp, MB d–Au and central Au–Au collisions.

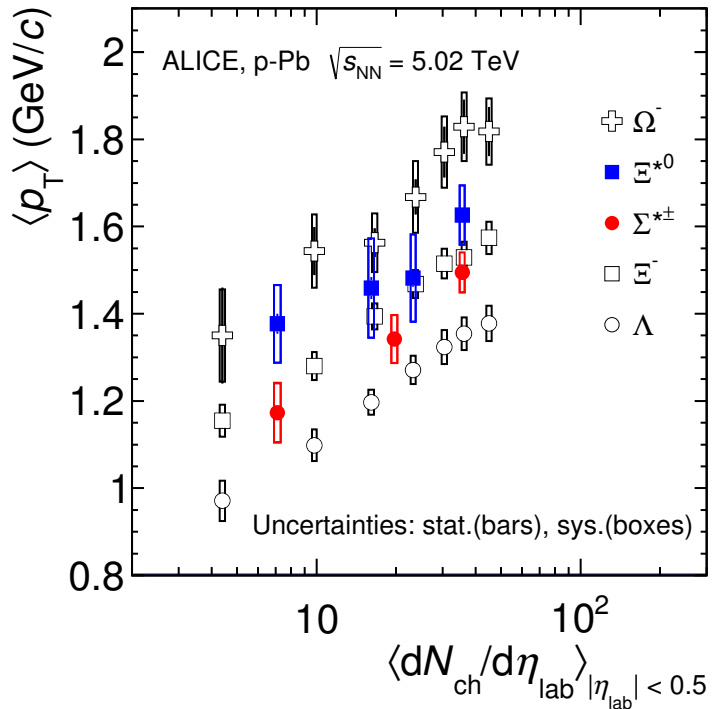


Figure 54: Mean transverse momenta $\langle p_T \rangle$ of Λ , Ξ^- , $\Sigma^{*\pm}$, Ξ^{*0} and Ω^- in p-Pb collisions at $\sqrt{s_{NN}} = 5.02$ TeV as a function of mean charged-particle multiplicity density $\langle dN_{ch}/d\eta_{lab} \rangle$, measured in the pseudorapidity range $|\eta_{lab}| < 0.5$. The results for Λ , Ξ^- and Ω^- are taken from [5, 6, 7]. Statistical and systematic uncertainties are represented as bars and boxes, respectively. The Ω^- and Ξ^- points in the 3rd and 4th lowest multiplicity bins are slightly displaced along the abscissa to avoid superposition with the $\Xi(1530)^0$ points.

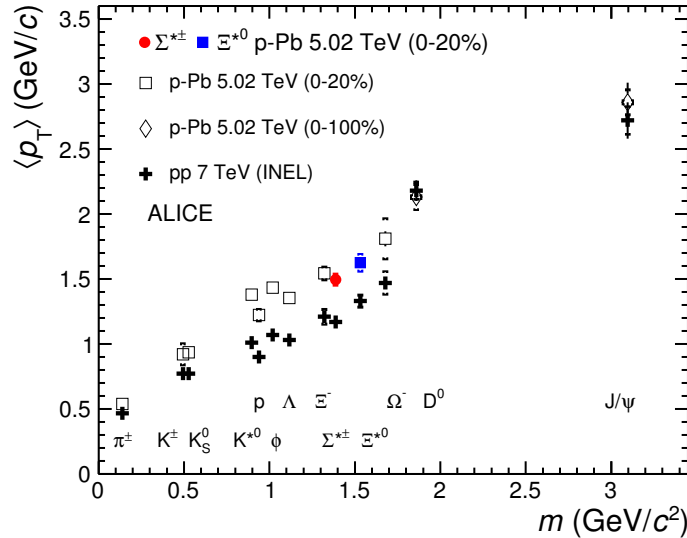


Figure 55: Mass dependence of the mean transverse momenta of identified particles for the 0 – 20% V0A multiplicity class and with $-0.5 < y_{\text{CMS}} < 0$ in p–Pb collisions at $\sqrt{s_{\text{NN}}}=5.02 \text{ TeV}$ [5, 7], and in minimum-bias pp collisions at $\sqrt{s}=7 \text{ TeV}$ [8] with $|y_{\text{CMS}}| < 0.5$. Additionally, D^0 and J/ψ results are plotted. The D^0 and J/ψ were measured in different rapidity ranges: $|y_{\text{CMS}}| < 0.5$ [9] ($|y_{\text{CMS}}| < 0.9$ [10]) for D^0 (J/ψ) in pp and $-0.96 < y_{\text{CMS}} < 0.04$ [9] ($-1.37 < y_{\text{CMS}} < 0.43$ [11]) for D^0 (J/ψ) in p–Pb. Note also that the results for D^0 and J/ψ in p–Pb collisions are for the 0-100% multiplicity class.

1313 Furthermore, for the light-flavour hadrons, the mean transverse momenta in p–Pb col-
1314 lisions are observed to be consistently higher than those in pp collisions at 7 TeV. The
1315 situation for the charm hadrons is different, where $\langle p_T \rangle$ appears compatible between both
1316 colliding systems. The discrepancy is likely due to different production mechanisms for
1317 heavy and light flavours and to a harder fragmentation of charm quarks. Specifically, the
1318 fact that $\langle p_T \rangle$ remains similar in pp and in p–Pb is consistent with an $R_{p\text{Pb}}$ ratio com-
1319 patible with unity at all p_T [9] for D^0 , and/or with the effects of shadowing in p–Pb which
1320 reduces the production at low p_T and thus increasing the overall $\langle p_T \rangle$ for J/ψ [11]; the
1321 small p_T hardening expected in pp when going from 5.02 to 7TeV is apparently not enough
1322 to counter-balance the situation.

1323 Because of small decrease of the $\langle p_T \rangle$ for proton and Λ relative to those for K^{*0} and
1324 ϕ , two different trends for mesons and baryons have been suggested [53]. Even including
1325 D^0 and J/ψ , as shown in Figure 55, a different trend for mesons and baryons cannot be
1326 convincingly established.

1327 **6.2 Particle yield ratios**

1328 **6.2.1 Integrated yield ratios of excited to ground-state hadrons**

1329 The integrated yield ratios of excited to ground-state hyperons [54, 5, 8, 7] with the same
1330 strangeness content, for different collision systems and energies, are shown in Figure 56
1331 as a function of system size. The ratio of $\Xi(1530)^0$ to Ξ is flat across the system and
1332 it complements the information derived from other resonance measurement for different
1333 lifetime which are shown in Figure 57.

1334 The short-lived resonances(ρ , K^* and Λ^*) which exhibit suppression from peripheral to
1335 central lead-lead collisions and with respect to thermal model in central lead-lead collisions.
1336 Currently favored explanation of is dominance of elastic re-scattering of decay daughters
1337 over regeneration in the hadronic phase.

1338 The constant behavior of the yield ratios of excited to ground-state hyperons with same
1339 strangeness content ($\Xi(1530)^0$ and Φ) indicates that neither regeneration nor re-scattering
1340 dominates with increasing collision system size because of its longer-lifetime.

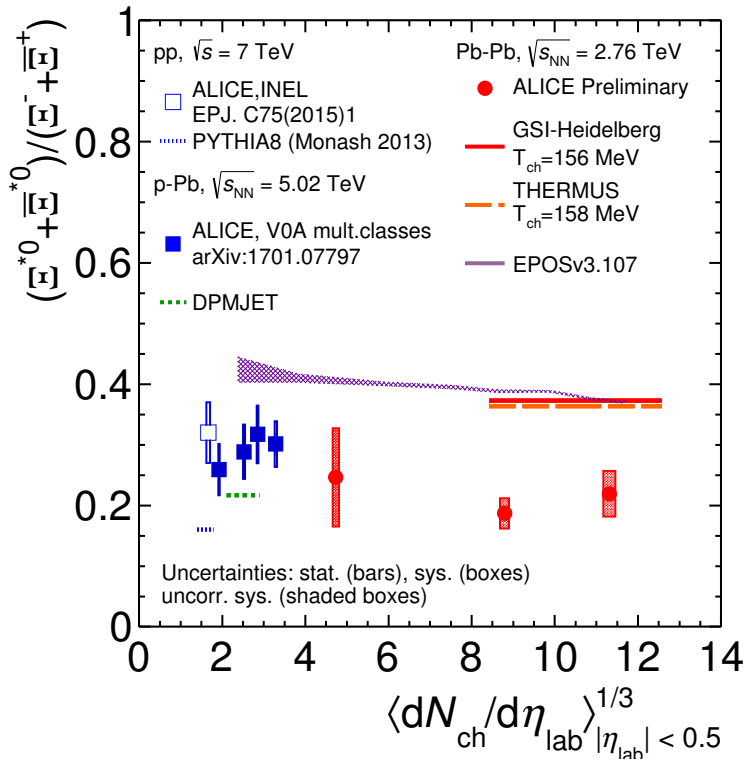


Figure 56: Ratio of $\Xi(1530)^0$ to Ξ^- measured in pp [8], p–Pb [5, 7] and Pb–Pb collisions as a function of $\langle dN_{ch}/d\eta_{lab} \rangle$ measured at midrapidity. Statistical uncertainties (bars) are shown as well as total systematic uncertainties (hollow boxes) and systematic uncertainties uncorrelated across multiplicity (shaded boxes). A few model predictions are also shown as lines at their appropriate abscissa.

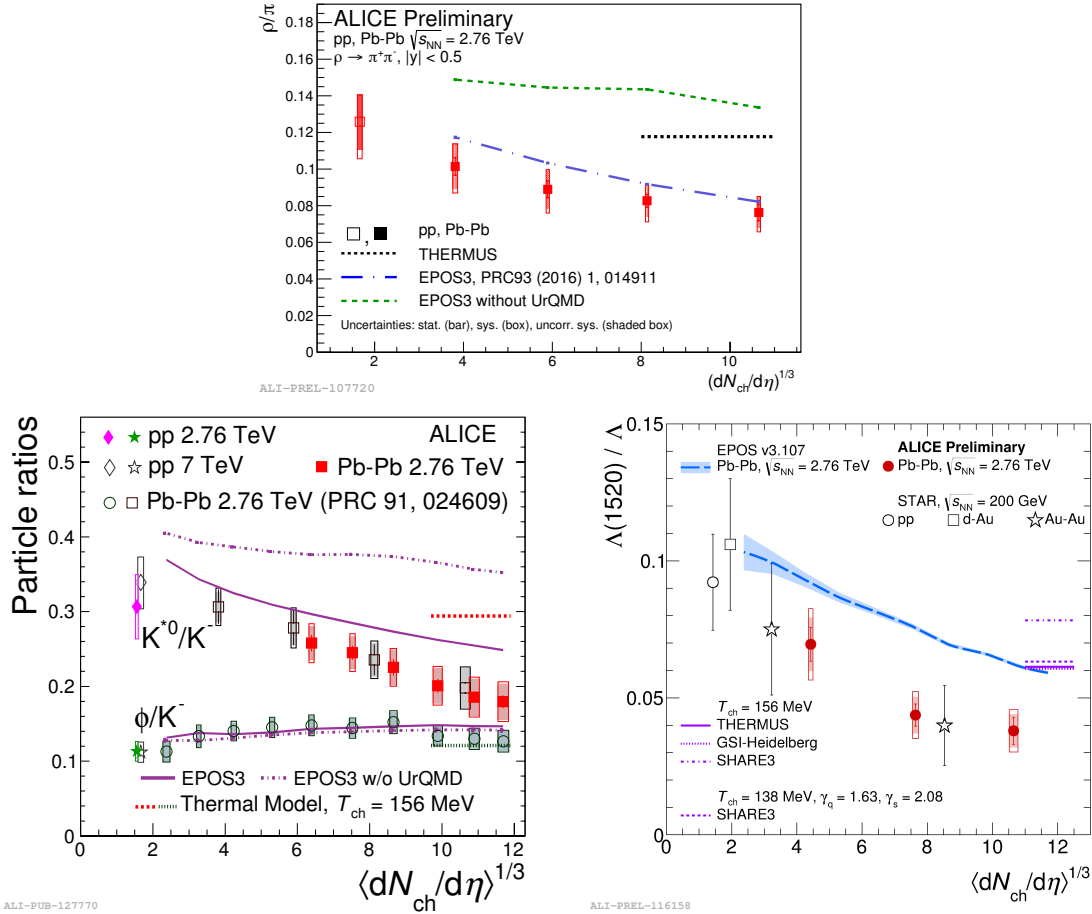


Figure 57: Ratio of ρ/π (Up), K^*/K , ϕ/K (Left bottom) and Λ^*/Λ with system size measured at mid-rapidity. Statistical uncertainties (bars) are shown as well as total systematic uncertainties (hollow boxes) and systematic uncertainties uncorrelated across multiplicity (shaded boxes). A few model predictions are also shown as lines at their appropriate abscissa.

1341 **6.3 Integrated yield ratios to pion**

1342 The integrated yield ratios of excited hyperons to pions are shown in Figure 58 to study
1343 the evolution of relative strangeness production yields with increasing collision system
1344 size. The ratio of $\Xi(1530)^0$ to Ξ is observed to be increase from pp to p–Pb collisions
1345 system and then, decrease from peripheral to central Pb–Pb collision. The QCD-inspired
1346 predictions like PYTHIA for pp [55] and DPMJET for p–Pb [48] clearly underestimate
1347 the observed yield ratios, while the statistical one seems to be comparable with results
1348 from high multiplicity in p–Pb but the ratio in Pb–Pb is below with respect to the model.
1349 The results in pp and p–Pb collisions are consistent with previous observation of ground-
1350 state hyperons to pion ratios. The Figure 59 presents particle yield ratios to pions of
1351 strange and multi-strange hadrons normalized to the values measured in pp collisions. As
1352 shown in the Figure 59, the $\Xi(1530)^0$ to pion ratios follow the trend of Ξ π as function of
1353 $\langle dN_{ch}/d\eta_{lab} \rangle$ and indicate that the strangeness enhancement observed in p–Pb collisions
1354 depends predominantly on the strangeness content, rather than on the hyperon mass.

1355 The Figure 60 also shows the hyperon-to-pion ratios and compared with model predictions. The
1356

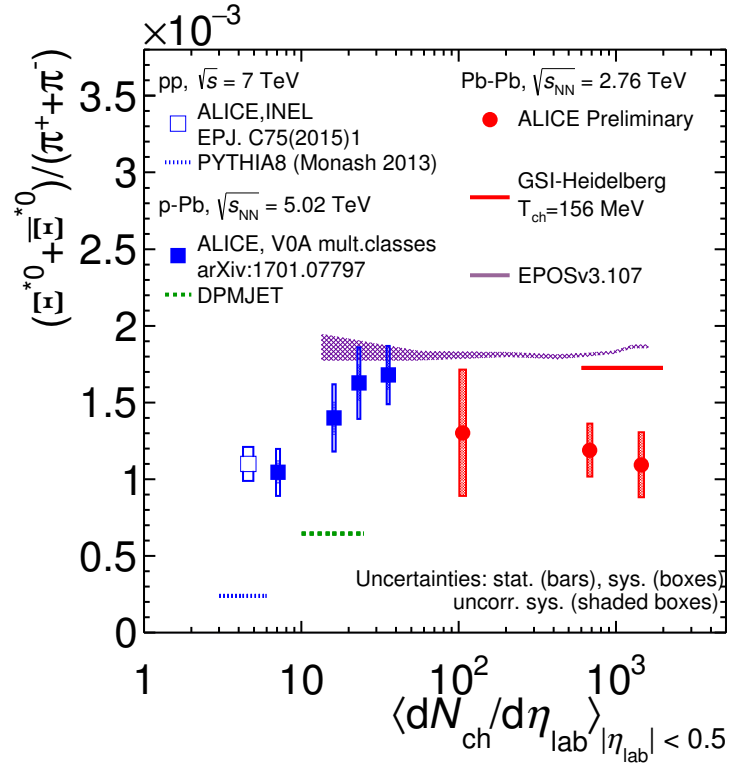


Figure 58: Ratio of $\Xi(1530)^0$ to π^\pm , measured in pp [12] and p–Pb [8] collisions, as a function of the average charged particle density ($\langle dN_{ch}/d\eta_{lab} \rangle$) measured at mid-rapidity. Statistical uncertainties (bars) are shown as well as total systematic uncertainties (hollow boxes) and systematic uncertainties uncorrelated across multiplicity (shaded boxes). A few model predictions are also shown as lines at their appropriate abscissa.

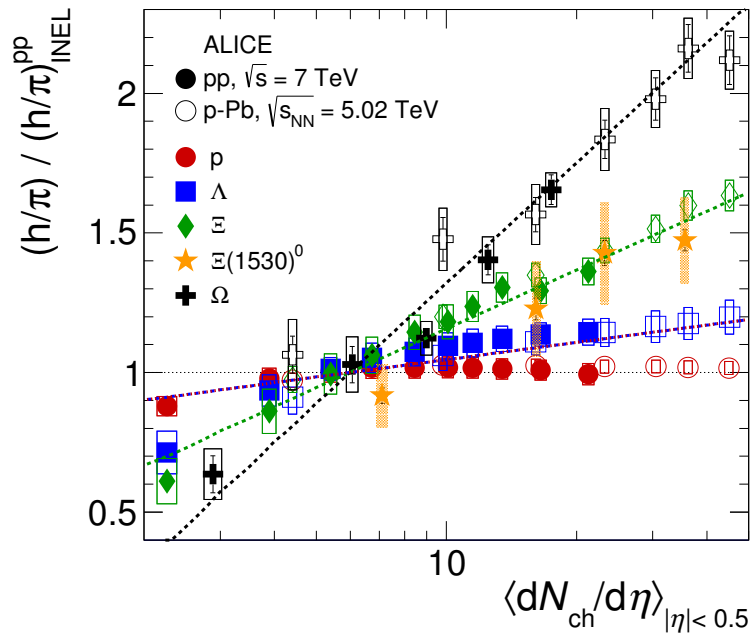


Figure 59: Particle yield ratios to pions of strange and multi-strange hadrons normalized to the values measured in pp collisions, both in pp and in p–Pb collisions. The common systematic uncertainties cancel in the double-ratio. The empty boxes represent the remaining uncorrelated uncertainties.

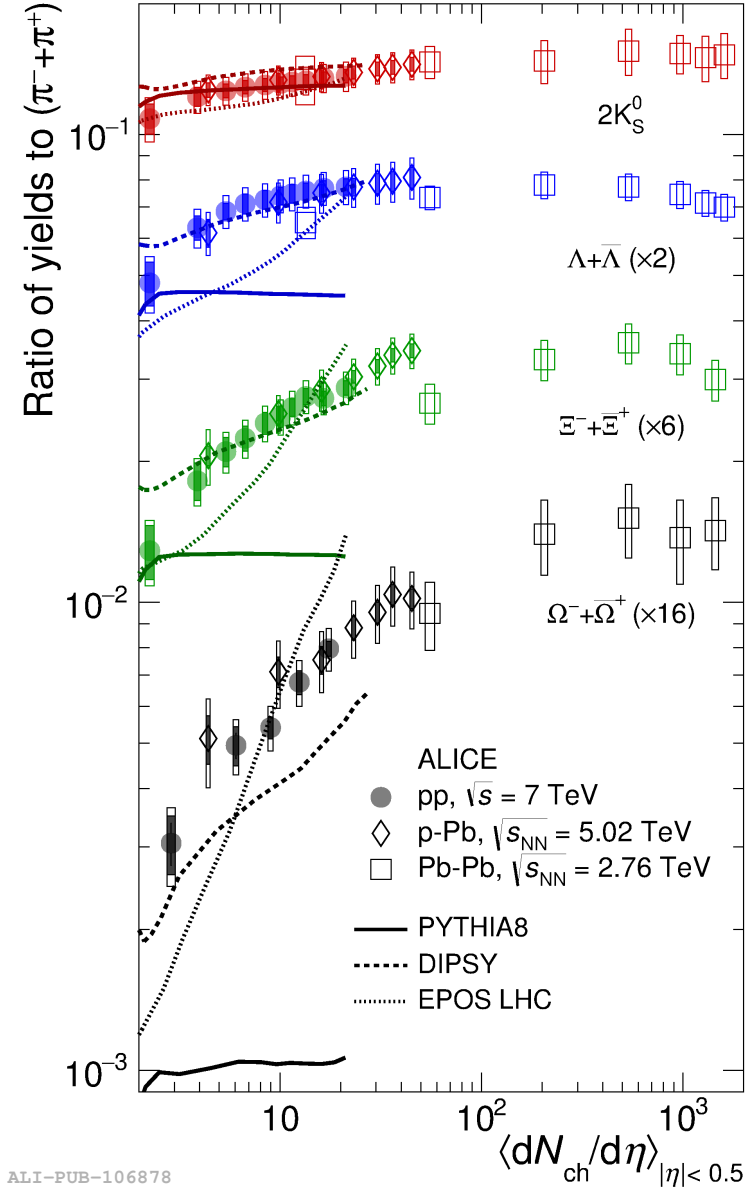


Figure 60: p_T -integrated yield ratios of strange and multi-strange hadrons to $(\pi^+ + \pi^-)$ as a function of $\langle dN_{ch}/d\eta_{lab} \rangle$ measured in the rapidity interval $|\eta| < 0.5$. The empty and dark-shaded boxes show the total systematic uncertainty and the contribution uncorrelated across multiplicity bins, respectively. The values are compared to calculations from MC models and to results obtained in Pb–Pb and p–Pb collisions at the LHC.

1357 **References**

- 1358 [1] **Particle Data Group** Collaboration, K. Olive *et al.*, “Review of Particle Physics,”
1359 *Chin. Phys. C* **38** (2014) 090001.
- 1360 [2] K. R. Ahmed Tounsi, “Strangeness Enhancement and Canonical Suppression,” *High*
1361 *Energy Physis A* **681** (2001) 119–123.
- 1362 [3] “TE-EPC-LPC LHC units,”.
1363 <http://te-epc-lpc.web.cern.ch/te-epc-lpc/machines/lhc/general.stm>.
- 1364 [4] **ALICE** Collaboration, K. e. a. Aamodt, “Alignment of the ALICE Inner Tracking
1365 System with cosmic-ray tracks,” *JINST* **5** (2010) P03003.
- 1366 [5] **ALICE** Collaboration, J. Adam *et al.*, “Multiplicity dependence of pion, kaon,
1367 proton and lambda production in p–Pb collisions at $\sqrt{s_{NN}} = 5.02$ TeV,” *Phys. Lett.*
1368 **B728** (2014) 25–38, [arXiv:1307.6796 \[nucl-ex\]](https://arxiv.org/abs/1307.6796).
- 1369 [6] **ALICE** Collaboration, J. Adam *et al.*, “Production of $K^*(892)^0$ and $\phi(1020)$ in
1370 p–Pb collisions at $\sqrt{s_{NN}} = 5.02$ TeV,” *Eur. Phys. J.* **C76** (2016) 245,
1371 [arXiv:1601.7868 \[nucl-ex\]](https://arxiv.org/abs/1601.7868).
- 1372 [7] **ALICE** Collaboration, J. Adam *et al.*, “Multi-strange baryon production in p–Pb
1373 collisions at $\sqrt{s_{NN}} = 5.02$ TeV,” *Phys. Lett.* **B758** (2016) 389–401,
1374 [arXiv:1512.07227 \[nucl-ex\]](https://arxiv.org/abs/1512.07227).
- 1375 [8] **ALICE** Collaboration, B. Abelev *et al.*, “Production of $\Sigma(1385)^{\pm}$ and $\Xi(1530)^0$ in
1376 proton-proton collisions at $\sqrt{s} = 7$ TeV,” *Eur. Phys. J.* **C75** (2015) 1,
1377 [arXiv:1406.3206 \[nucl-ex\]](https://arxiv.org/abs/1406.3206).
- 1378 [9] **ALICE** Collaboration, J. Adam *et al.*, “ D -meson production in p–Pb collisions at
1379 $\sqrt{s_{NN}} = 5.02$ TeV and in pp collisions at $\sqrt{s} = 7$ TeV,” *Phys. Rev. C* **94** (2016)
1380 054908, [arXiv:1605.07569 \[nucl-ex\]](https://arxiv.org/abs/1605.07569).
- 1381 [10] **ALICE** Collaboration, B. Abelev *et al.*, “Inclusive J/ψ production in pp collisions
1382 at $\sqrt{s} = 2.76$ TeV,” *Phys. Lett.* **B718** (2012) 295–306, [arXiv:1203.3641 \[hep-ex\]](https://arxiv.org/abs/1203.3641).
- 1383 [11] **ALICE** Collaboration, J. Adam *et al.*, “Rapidity and transverse-momentum
1384 dependence of the inclusive J/ψ nuclear modification factor in p–Pb collisions at
1385 $\sqrt{s_{NN}} = 5.02$ TeV,” *JHEP* **06** (2015) 55, [arXiv:1503.07179 \[nucl-ex\]](https://arxiv.org/abs/1503.07179).
- 1386 [12] **ALICE** Collaboration, J. Adam *et al.*, “Measurement of pion, kaon and proton
1387 production in proton-proton collisions at $\sqrt{s} = 7$ TeV,” *Eur. Phys. J.* **C75** (2015)
1388 226, [arXiv:1504.00024 \[nucl-ex\]](https://arxiv.org/abs/1504.00024).

- 1389 [13] F. Halzen and A. Martin, “Quarks and Leptons: an introductory course in modern
 1390 particle physics,” *By John Wiley and Sons* (1984) .
- 1391 [14] T. K. Nayak, “Heavy Ions: Results from the Large Hadron Collider,” *Pramana* **79**
 1392 (2012) 719–735.
- 1393 [15] S. Wheaton, J. Cleymans, and M. Hauer, “THERMUS: A Thermal model package
 1394 for ROOT,” *Comput. Phys. Commun.* **180** (2009) 84–106, [arXiv:hep-ph/0407174](https://arxiv.org/abs/hep-ph/0407174)
 1395 [hep-ph].
- 1396 [16] S. O. T. P. K. W. H.J. Drescher, M. Hladik, “Parton-Based Gribov-Regge Theory,”
 1397 *Phys. Rept.* **350** (2001) 93–289, [hep-ph/0007198](https://arxiv.org/abs/hep-ph/0007198).
- 1398 [17] T. P. M. B. K. M. K. Werner, Iu. Karpenko, “Event-by-event simulation of the
 1399 three-dimensional hydrodynamic evolution from flux tube initial conditions in
 1400 ultrarelativistic heavy ion collisions,” *Phys. Rev.* **C82** (2010) 044904.
- 1401 [18] I. K. T. P. K. Werner, B. Guiot, “Analyzing radial flow features in p-Pb and p-p
 1402 collisions at several TeV by studying identified-particle production with the event
 1403 generator EPOS3,” *Phys. Rev.* **C89** (2014) 064903.
- 1404 [19] K. Werner., “Analyzing radial flow features in p-Pb and p-p collisions at several TeV
 1405 by studying identified-particle production with the event generator EPOS3,” *Phys.*
 1406 *Rev. Lett.* **98** (2007) 152301.
- 1407 [20] S. B. et al., “Microscopic Models for Ultrarelativistic Heavy Ion Collisions,” *Prog.*
 1408 *Part. Nucl. Phys.* **41** (1998) 255.
- 1409 [21] M. B. et al., “Relativistic Hadron-Hadron Collisions in the Ultra-Relativistic
 1410 Quantum Molecular Dynamics Model,” *J. Phys.* **G25** (1999) 1859–1896.
- 1411 [22] M. Gell-Mann and Y. Ne’eman, “The Eightfold Way,” *By W.A. Benjamin* (1964) .
- 1412 [23] J. Rafelski and B. Mller, “Strangeness Production in the Quark-Gluon Plasma,”
 1413 *Phys. Rev. Lett* **48** (1982) 1066–1069.
- 1414 [24] **ALICE** Collaboration, B. Abelev *et al.*, “Multi-strange baryon production at
 1415 mid-rapidity in Pb–Pb collisions at $\sqrt{s_{\text{NN}}} = 2.76$ TeV,” *Phys. Lett.* **B728** (2014)
 1416 216–227, [arXiv:1307.5543](https://arxiv.org/abs/1307.5543) [nucl-ex].
- 1417 [25] P. Braun-Munziger, “Chemical equilibration and the Hadron-QGP phase
 1418 transition,”.
- 1419 [26] **ALICE** Collaboration, B. Abelev *et al.*, “Performance of the ALICE Experiment at
 1420 the CERN LHC,” *Int. J. Mod. Phys.* **A29** (2014) 1430044, [arXiv:1402.4476](https://arxiv.org/abs/1402.4476)
 1421 [nucl-ex].

- 1422 [27] L. Evans and P. Bryant, “LHC Machine,” *JINST* **3** (2008) S08001.
- 1423 [28] C. S. I. Service, “LHC Design Report Volume I+II+III,” *In*
1424 *CERN-2004-003-V1(-V2)(-V3)* (2004) .
- 1425 [29] “ALICE Technical Proposal,” *In CERN-LHCC-95-71* (1995) .
- 1426 [30] “ATLAS Technical Proposal,” *In CERN-LHCC-94-43* (1994) .
- 1427 [31] “CMS Technical Proposal,” *In CERN-LHCC-94-38* (1994) .
- 1428 [32] “LHCb Technical Proposal,” *In CERN-LHCC-98-004* (1998) .
- 1429 [33] “Total Cross Section, Elastic Scattering and Diffraction Dissociation at the LHC,”
1430 *In CERN-LHCC-99-007* (1999) .
- 1431 [34] **ALICE** Collaboration, K. Aamodt *et al.*, “The ALICE experiment at the CERN
1432 LHC,” *JINST* **3** (2008) S08002.
- 1433 [35] **ALICE** Collaboration, L. B. et al, “Definition of the ALICE coordinate system and
1434 basic rules for sub-detector components numbering,” *In Internal Note*
1435 *ALICE-INT-2003-038* (2003) .
- 1436 [36] **ALICE** Collaboration, J. e. a. Alme, “The ALICE TPC, a large 3-dimensional
1437 tracking device with fast readout for ultra-high multiplicity events,” *In Nuclear*
1438 *Instruments and Method in Physics Research* **A622** (2010) 316–367.
- 1439 [37] “Technical Design Report on Forward Detectors: FMD, T0 and VZERO,” *In*
1440 *CERN-LHCC-2004-025* (2004) .
- 1441 [38] R. Glauber, “Lectures in Theoretical Physics,” *By Interscience Publishers.* **1** (1959)
1442 315.
- 1443 [39] A. S. K.C. Chung, C.S. Whang and G. Pech, “Transverse and forward energy
1444 distributions in untra-relativistic heavy-ion collisions by an absorption model,”
1445 *Physics Review* **C57** (1998) 847–856.
- 1446 [40] **ALICE** Collaboration, J. Adam *et al.*, “Centrality dependence of particle
1447 production in p–Pb collisions at $\sqrt{s_{\text{NN}}}= 5.02$ TeV,” *Phys. Rev.* **C91** (2015) 064905,
1448 [arXiv:1412.6828 \[nucl-ex\]](https://arxiv.org/abs/1412.6828).
- 1449 [41] **ALICE** Collaboration, B. Abelev *et al.*, “Centrality determination of Pb–Pb
1450 collisions at $\sqrt{s_{\text{NN}}}= 2.76$ TeV with ALICE,” *Phys. Rev.* **C88** (2013) ,
1451 [arXiv:1303.0737 \[nucl-ex\]](https://arxiv.org/abs/1303.0737).
- 1452 [42] “ALICE Technical Design Report of the Trigger, Data Acquisition, High-Level
1453 Trigger, Control system,” *In CERN-LHCC-2003-062.* (2003) .

- 1454 [43] “The Grid - Blueprint for a New Computing Infrastructure,” *By Morgan Kaufmann*
 1455 *Publishers.* (1999) .
- 1456 [44] e. a. Bagnasco. S, “AliEn: ALICE Environment on the GRID,” *In Jounal of Physics: Conference Series* **119** (2008) n.062012.
- 1458 [45] R. Brun and F. Rademakers, “ROOT - An object oriented data analysis framework,” *In Nuclear Instrument and Methods in Physics Research Section A* **389** (1997) 81–86.
- 1461 [46] **ALICE** Collaboration, B. Abelev *et al.*, “Pseudorapidity Density of Charged Particles in p–Pb Collisions at $\sqrt{s_{\text{NN}}}= 5.02$ TeV,” *Phys. Rev. Lett.* **110** (2013) 032301, [arXiv:1210.3615 \[nucl-ex\]](https://arxiv.org/abs/1210.3615).
- 1464 [47] **ALICE** Collaboration, K. Aamodt *et al.*, “Strange particle production in proton-proton collisions at $\sqrt{s}= 0.9$ TeV with ALICE at the LHC,” *Eur. Phys. J.* **C71** (2011) 1594, [arXiv:1012.3257 \[nucl-ex\]](https://arxiv.org/abs/1012.3257).
- 1467 [48] S. Roesler, R. Engel, , and J. Ranft, “The Monte Carlo Event Generator DPMJET-III, Advanced Monte Carlo for Radiation Physics, Particle Transport Simulation and Applications,” *Conference Proceedings, MC2000, Lisbon, Portugal, October 23–26* (2000) 1033–1038, [hep-ph/0012252](https://arxiv.org/abs/hep-ph/0012252).
- 1471 [49] R. Brun, F. Carminati, and S. Giani, “GEANT detector description and simulation tool,” *CERN-W5013* (1994) .
- 1473 [50] R. Barlow, “Systematic Errors: Facts and Fictions,” *Presented at Advanced Statistical Techniques in HEP, Durham, March 2002* (2002) 333p, [hep-ex/0207026v1](https://arxiv.org/abs/hep-ex/0207026v1).
- 1476 [51] **ALICE** Collaboration, B. Abelev *et al.*, “Centrality dependence of π , K and p production in Pb–Pb collisions at $\sqrt{s_{\text{NN}}}= 2.76$ TeV,” *Phys. Rev.* **C88** (2013) , [arXiv:1301.4361 \[nucl-ex\]](https://arxiv.org/abs/1301.4361).
- 1479 [52] **STAR** Collaboration, B. I. Abelev *et al.*, “Hadronic resonance production in d–Au collisions at $\sqrt{s_{\text{NN}}}= 200$ GeV measured at the BNL Relativistic Heavy-Ion Collider,” *Phys. Rev.* **C78** (2008) 044906, [arXiv:0801.0450 \[nucl-ex\]](https://arxiv.org/abs/0801.0450).
- 1482 [53] A. Velásquez, “Mean p_{T} scaling with m/n_{q} at the LHC: Absence of (hydro) flow in small systems?,” *Nucl. Phys.* **A943** (2015) 9–17, [arXiv:1506.00584 \[hep-ph\]](https://arxiv.org/abs/1506.00584).
- 1484 [54] **ALICE** Collaboration, B. Abelev *et al.*, “Multi-strange baryon production in pp collisions at $\sqrt{s}= 7$ TeV with ALICE,” *Phys. Lett.* **B712** (2012) 309, [arXiv:1204.0282 \[nucl-ex\]](https://arxiv.org/abs/1204.0282).

- 1487 [55] T. Sjöstrand, S. Mrenna, and P. Skands, “A brief introduction to PYTHIA 8.1,”
1488 *Comput. Phys. Comm.* **178** (2008) 852–867, [arXiv:0710.3820](https://arxiv.org/abs/0710.3820) [hep-ph].

1489 **Acknowledgements**